

Rheinisch-Westfaelische Technische
Hochschule Aachen

Fakultät für Mathematik, Informatik und Naturwissenschaften

Masterarbeit Physik

MEASUREMENT OF TOP SPIN ASYMMETRIES IN
T-CHANNEL SINGLE TOP QUARK PRODUCTION
AT 7 TEV WITH THE CMS EXPERIMENT

von Matthias Komm

17.10.2012

Erstgutachter

Professor Dr. Martin Erdmann

III. Physikalischen Institut A
RWTH Aachen

Zweitgutachter

Professor Dr. Thomas Hebbeker

III. Physikalischen Institut A
RWTH Aachen

Matthias Komm:

MEASUREMENT OF TOP SPIN ASYMMETRIES IN T-CHANNEL SINGLE
TOP QUARK PRODUCTION AT 7 TeV WITH THE CMS EXPERIMENT

Masterarbeit Physik

Rheinisch-Westfaelische Technische Hochschule Aachen

Bearbeitungszeitraum: 17. Oktober 2011 - 17. Oktober 2012

Contents

1	Introduction	1
2	Theory	3
2.1	The Standard Model of Particle Physics	3
2.1.1	General Construction	3
2.1.2	The Electroweak interactions and Higgs Mechanism	5
2.1.3	Quantum Chromodynamics	8
2.2	The Top Quark	9
2.2.1	Top quark production and decay	9
2.2.2	Theoretical Results	10
2.3	Effective Theory	11
2.3.1	Anomalous Couplings	11
2.3.2	W Boson Helicity Fractions	11
2.3.3	Top Spin Asymmetries	12
2.4	The WHIZARD Monte Carlo Generator	14
3	Experimental Setup	15
3.1	The Large Hadron Collider	15
3.2	The CMS Experiment	17
3.3	Reconstruction of Physics Objects	21
3.3.1	The Particle-Flow Algorithm	21
3.3.2	Muon Identification	21
3.3.3	Missing Transverse Energy	22
3.3.4	Jet Definition	22
3.3.5	Identification of Jets from b-Quarks	23
3.4	Analysis Software	23
3.4.1	CMS Software Framework	23
3.4.2	THETA	24
3.4.3	ROOT	24
3.4.4	Toolkit for Multivariate Data Analysis with ROOT	24
3.4.5	VISPA and PXL	26

4	Event Selection and Simulation	27
4.1	The Simulated Standard Model Samples	28
4.2	Simulated Signal Samples with WHIZARD	29
4.2.1	Sample Generation	29
4.2.2	Results	30
4.3	Dataset	32
4.4	Event Selection	34
4.5	Top Quark Reconstruction	36
4.6	Validation	38
5	Analysis Strategy	43
5.1	The Observables	43
5.2	Discrimination of Signal and Background	43
5.2.1	Choice of Independent Variables	45
5.2.2	MVA Training	46
5.2.3	Discrimination Power	47
5.3	Unfolding	51
5.3.1	Introduction	51
5.3.2	Regularization	53
5.3.3	Construction of the Response Matrix	56
6	Measurement Technique and Results	61
6.1	Systematic Uncertainties	61
6.1.1	Sources	61
6.1.2	Fit to the top quark mass	66
6.1.3	Impact of Uncertainties	69
6.2	Measurement Procedure	71
6.3	Optimization	73
6.4	Results	79
6.4.1	The Unfolded Distributions	79
6.4.2	The Top Quark Spin Asymmetries	83
6.4.3	Fit to Anomalous Couplings	86
7	Conclusion	89
	Appendix	A
	List of Figures	G
	List of Tables	K

Bibliography

M

Danksagung

S

Erklärung

U

Introduction

The Standard Model of Particle Physics (SM) is the theory of the interactions between point-like (elementary) particles. Among all known elementary particles, the top quark has the highest mass of $m_t = 173.5 \text{ GeV}$ [50]. In 1995, the top quark was discovered at the Tevatron Collider (Fermilab) in Chicago, USA [2]. The SM predicts that in electroweak interactions only left-handed top quarks (t) couple to the W boson (W) and the bottom quark (b). This is called a “vector”-“axialvector” (V-A) structure. However it is possible that yet undiscovered interactions or particles may lead to a deviation from this coupling structure.

In this thesis, the strategy for and results of a first measurement of the top quark spin asymmetries are presented. These asymmetries are measured in single top quark t-channel production. They are sensitive to the coupling structure at the Wtb-vertex and are used to constrain possible anomalous couplings in a further step. The analysis uses data from proton-proton collisions recorded by the CMS (Compact Muon Solenoid) experiment at a center-of-mass energy of $\sqrt{s} = 7 \text{ TeV}$.

The next chapter briefly covers the theory behind the Standard Model of Particle Physics and focuses especially on the top quark. An effective extension of the SM is discussed to introduce a more general coupling scenario. The Monte-Carlo event generator WHIZARD is used to generate anomalous coupling scenarios.

In chapter 3, the experimental setup is discussed. The CMS experiment, the reconstruction of the necessary physics objects and the used software are described. The multivariate classification methods “Boosted Decision Tree” and “Projective Likelihood Estimator” are explained.

The event simulation and selection are described in chapter 4. The analysis strategy is presented in chapter 5. The multivariate classification methods are used to further discriminate remaining background contributions after the event selection. This yields a very pure selection of signal events from data. The resulting distributions are unfolded to correct for detector and reconstruction effects. The unfolding procedure and its regularization are analyzed in detail.

Finally, in chapter 6, the top quark spin asymmetries are measured using the unfolded distributions. The complete analysis procedure is cross checked with the generated anomalous coupling samples.

Unit Convention

Throughout this thesis the “natural” unit convention, which differs from the SI units is used. This means that the following is assumed:

- for the speed of light: $c = 1$
- for the Planck constant: $\hbar = 1$
- for the electric permittivity: $\epsilon_0 = 1$

which changes amongst others the following basic SI units to

- mass $[m] = \text{GeV}$
- time $[t] = \frac{1}{\text{GeV}}$
- length $[s] = \frac{1}{\text{GeV}}$

Theory

2.1 The Standard Model of Particle Physics

The Standard Model of Particle Physics (SM) is a theory that describes the interactions between elementary particles. So far, deep inelastic scattering experiments have detected no sub structure of elementary particles. They are therefore considered as point-like. Table 2.1 and table 2.2 list the elementary particles, with spin $s = \frac{1}{2}$ (fermions). The given masses are taken from Ref. [50]. For the neutrino masses only exclusion limits are given. In the SM these are considered as massless.

Each particle carries different charges. These determine if it can participate in electromagnetic (EM), in weak or in strong interactions. The interactions themselves are mediated by bosonic elementary particles with spin $s = 1$ (gauge bosons) and are listed in Table 2.3.

Table 2.1: The SM leptons.

generation	name	symbol	mass	EM charge	interactions
1	electron	e^-	0.511 MeV	-1	EM, weak
	electron neutrino	ν_e	$< 2.05 \text{ eV}$	0	weak
2	muon	μ^-	105.66 MeV	-1	EM, weak
	muon neutrino	ν_μ	$< 0.19 \text{ MeV}$	0	weak
3	tau	τ^-	1.777 GeV	-1	EM, weak
	tau neutrino	ν_τ	$< 18.2 \text{ MeV}$	0	weak

The next subsections will shortly describe the construction procedure of the SM theory.

2.1.1 General Construction

The SM is based on Quantum Field Theory (QFT). Here, elementary particles are considered as excitation modes of associated quantized fields Ψ . Dynamics are described via Lagrangian density functions. Starting with a “free” Lagrangian density for fermions

$$\mathcal{L} = \bar{\Psi} (i\partial - m) \Psi, \quad \partial = \gamma_\mu \frac{\partial}{\partial x^\mu}, \quad \bar{\Psi} = \Psi^\dagger \gamma_0, \quad (2.1.1)$$

one can obtain the equation of motion (for fermions: the Dirac equation) by using the Euler-Lagrangian equation

2.1 The Standard Model of Particle Physics

Table 2.2: The SM Quarks.

generation	name	symbol	mass	EM charge	interactions
1	up	u	$2.3^{+0.7}_{-0.5} \text{ MeV}$	$\frac{2}{3}$	EM, weak, strong
	down	d	$4.8^{+0.7}_{-0.3} \text{ MeV}$	$-\frac{1}{3}$	EM, weak, strong
2	charm	c	$1.275 \pm 0.025 \text{ GeV}$	$\frac{2}{3}$	EM, weak, strong
	strange	s	$95 \pm 5 \text{ MeV}$	$-\frac{1}{3}$	EM, weak, strong
3	top	t	$173.5 \pm 1.0 \text{ GeV}$	$\frac{2}{3}$	EM, weak, strong
	bottom	b	$4.18 \pm 0.03 \text{ GeV}$	$-\frac{1}{3}$	EM, weak, strong

Table 2.3: The SM interactions and their gauge bosons [50].

interactions	gauge group	gauge bosons	mass
EM	U(1)	photon γ	0
weak	SU(2)	Z^0 boson	$80.385 \pm 0.015 \text{ GeV}$
		W^\pm bosons	$91.188 \pm 0.002 \text{ GeV}$
strong	SU(3)	8 gluons g	0

$$0 = \frac{\partial}{\partial x_\mu} \left(\frac{\partial \mathcal{L}}{\partial (\partial \bar{\Psi} / \partial x_\mu)} \right) - \frac{\partial}{\partial \bar{\Psi}} \mathcal{L} = (i\not{\partial} - m) \Psi. \quad (2.1.2)$$

Interactions can be introduced by requiring that the Lagrangian density is invariant under a local gauge transformation of the field Ψ . For example, the electromagnetic interactions is obtained by postulating

$$\Psi \rightarrow \Psi' = \Psi \cdot e^{-iq\alpha(x)} \quad (2.1.3)$$

with the free chosen local phase $\alpha(x)$ and the EM charge q . This transforms the Lagrangian density to

$$\Rightarrow \mathcal{L} \rightarrow \mathcal{L}' = \bar{\Psi}(i\not{\partial} + q\not{\partial}\alpha(x) - m)\Psi. \quad (2.1.4)$$

The requirement for invariance of the Lagrangian density $\mathcal{L}(\Psi') = \mathcal{L}(\Psi)$ under such transformation can be solved by adding the additional photon field A_μ . It transforms under local gauge transformation to

$$A_\mu \rightarrow A'_\mu = A_\mu - \partial_\mu \alpha(x). \quad (2.1.5)$$

This leads to

$$\Rightarrow \mathcal{L} = \underbrace{-\frac{1}{4}F_{\mu\nu}F^{\mu\nu}}_{\text{photon propagator}} + \underbrace{\bar{\Psi}(i\not{\partial} - m)\Psi}_{\text{fermion propagator}} - \underbrace{q\bar{\Psi}\gamma_\mu\Psi A^\mu}_{\text{interaction vertex}}, \quad F_{\mu\nu} = \partial_\mu A_\nu - \partial_\nu A_\mu \quad (2.1.6)$$

where additionally the already gauge invariant photon propagator has been added. This construction procedure predicts that the photon is massless. Extending the Lagrangian density with a mass term proportional to $\propto m_\gamma^2 A_\mu A^\mu$ violates the invariance. Furthermore, the conservation of angular momentum at the interaction vertex and its degrees of freedom states that the photon is a boson with spin $s = 1$.

In conclusion, the Lagrangian density of the electromagnetic interactions is determined by requiring local gauge invariance. Weak and strong interactions are as well connected to certain gauge group transformations. However, experiments have shown that the gauge bosons of the weak interactions have non-zero masses. The list of the SM gauge bosons and their masses are given in table 2.3 together with the associated gauge groups and interactions.

2.1.2 The Electroweak interactions and Higgs Mechanism

The EM and weak interactions can be united to the electroweak interactions. In addition, the following experimental results had to be included:

- In weak interactions, parity is not conserved. Only left-handed fermions can couple to charged currents [72].
- Three of the four gauge bosons of the unified $U(1) \otimes SU(2)$ group are massive.

The Glashow-Weinberg-Salam model accounts for the coupling of left-handed fermions by splitting the fermion fields into left- and right-handed fields:

$$\Psi_L = \underbrace{\frac{1}{2}(1 - \gamma_5)}_{P_L} \Psi, \quad (\text{SU}(2) \text{ doublet}); \quad \Psi_R = \underbrace{\frac{1}{2}(1 + \gamma_5)}_{P_R} \Psi, \quad (\text{SU}(2) \text{ singlet}) \quad (2.1.7)$$

Therefore, lepton and quark fields are splitted into

2.1 The Standard Model of Particle Physics

$$\vec{E}_L = \left\{ \begin{pmatrix} \nu_e \\ e^- \end{pmatrix}_L, \begin{pmatrix} \nu_\mu \\ \mu^- \end{pmatrix}_L, \begin{pmatrix} \nu_\tau \\ \tau^- \end{pmatrix}_L \right\}; \quad \vec{Q}_L = \left\{ \begin{pmatrix} u \\ d \end{pmatrix}_L, \begin{pmatrix} c \\ s \end{pmatrix}_L, \begin{pmatrix} t \\ b \end{pmatrix}_L \right\} \quad (2.1.8)$$

and

$$\vec{e}_R = \{e_R, \mu_R, \tau_R\}; \quad \vec{u}_R = \{u_R, c_R, t_R\}; \quad \vec{d}_R = \{d_R, s_R, b_R\}. \quad (2.1.9)$$

The right-handed neutrinos do not couple at all in the SM. The resulting Lagrangian density

$$\mathcal{L} = \sum_j^3 \left(\vec{E}_L^j i\gamma_\mu D^\mu E_L^j + \vec{Q}_L^j i\gamma_\mu D^\mu Q_L^j + \vec{e}_R^j i\gamma_\mu D^\mu e_R^j + \vec{u}_R^j i\gamma_\mu D^\mu u_R^j + \vec{d}_R^j i\gamma_\mu D^\mu d_R^j \right) \quad (2.1.10)$$

with the covariant derivatives

$$D_\mu = \partial_\mu - ig\vec{W}_\mu \vec{T} - ig'\gamma \cdot B_\mu, \quad Y = Q_{EM} - T_3 \quad (\text{"hypercharge"}) \quad (2.1.11)$$

does then not involve terms of the form

$$\mathcal{L}_R \propto W_\mu^+ \bar{\Psi}_R \gamma^\mu \Psi'_R + \text{h.c.}, \quad (2.1.12)$$

where the EM charge would be conserved. The structure of the coupling to W^\pm bosons includes only terms proportional to $\propto (\gamma_\mu - \gamma_\mu \gamma_5)$ which transforms like a "vector" – "axial vector" (V-A structure). By using the chiral representation of a general field $\Psi = (\Psi_L, \Psi_R)$ with $\gamma_5 \Psi_L = (-1)\Psi_L$ and $\gamma_5 \Psi_R = (+1)\Psi_R$, the eigenstate Ψ_L is labeled "left-handed" and the eigenstate Ψ_R is labeled "right-handed". In the case of massless particles, the chirality is equal to the helicity H (projection of the spin along the momentum).

Mass terms for the three gauge bosons are generated by the Englert-Brout-Higgs-Guralnik-Hagen-Kibble-mechanism [47, 46, 40, 44]. For this, another $SU(2)$ field ϕ with a $U(1) \otimes SU(2)$ symmetry is needed. This symmetry gets "broken" or "hidden" by shifting the vacuum expectation value of ϕ through a potential $V(\phi^\dagger \phi) = \lambda (\phi^\dagger \phi)^2 - \mu^2 \phi^\dagger \phi$, shown in figure 2.1, to

$$\langle \phi \rangle_{\min} = \sqrt{\frac{\mu^2}{\lambda}} \equiv \frac{v}{\sqrt{2}}. \quad (2.1.13)$$

Then, one can develop ϕ around this minimum to

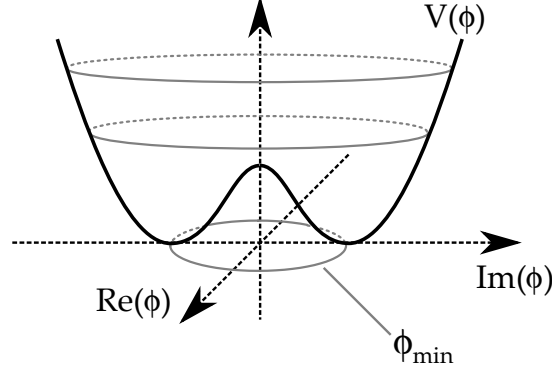


Figure 2.1: The Higgs Potential - “Mexican Hat”.

$$\phi = \frac{1}{\sqrt{2}} \begin{pmatrix} 0 \\ v + h(x) \end{pmatrix} \cdot \exp \left(-\frac{i\theta(x)}{v} \right). \quad (2.1.14)$$

For the masses of the electroweak gauge bosons, the $U(1) \otimes SU(2)$ invariant Lagrangian density

$$\mathcal{L} = \dots + \left(D_\mu \phi^\dagger \right) \left(D^\mu \phi \right) - V(\phi^\dagger \phi), \quad D_\mu = \partial_\mu - \underbrace{ig \frac{\vec{\tau}}{2} \vec{W}_\mu}_{SU(2)} - \underbrace{ig' \frac{1}{2} B_\mu}_{U(1)} \quad (2.1.15)$$

contains amongst interactions terms the following after the symmetry breaking:

$$\text{“Higgs” boson : } \mathcal{L}_h = \frac{1}{2} (\partial_\mu h) (\partial^\mu h) - \lambda^2 v^2 h^2 \quad (2.1.16)$$

$$W^\pm \text{ bosons : } \mathcal{L}_{W^\pm} = -\frac{1}{8} g^2 v^2 W_{1,\mu} W_1^\mu - \frac{1}{8} g^2 v^2 W_{2,\mu} W_2^\mu \quad (2.1.17)$$

$$W_3, B \text{ bosons : } \mathcal{L}_{W_3, B} = -\frac{1}{8} v^2 (g W_{3,\mu} - g' B_\mu) (g W_3^\mu - g' B^\mu) \quad (2.1.18)$$

The Higgs boson is predicted by the SM but was not observed for a long time. Very recently, an evidence for a Higgs-like boson with a mass of around $m_H \approx 126 \text{ GeV}$ has been observed by the ATLAS [1] and CMS [21] experiments. The W^\pm bosons can be obtained by transforming $W_\mu^\pm = \frac{1}{\sqrt{2}} (W_{1,\mu} \mp i W_{2,\mu})$. The W_3, B - fields are mixed. By introducing the following transformation

$$\begin{pmatrix} Z^0 \\ A \end{pmatrix} = \begin{pmatrix} \cos \theta_W & -\sin \theta_W \\ \sin \theta_W & \cos \theta_W \end{pmatrix} \begin{pmatrix} W_3 \\ B \end{pmatrix}, \quad \cos \theta_W = \frac{g}{\sqrt{g^2 + g'^2}} \quad (2.1.19)$$

2.1 The Standard Model of Particle Physics

with the weak-mixing angle or “Weinberg” angle θ_W , one obtains a massless boson, the photon A , and one massive boson, the Z^0 boson. Thus, this mechanism of spontaneous symmetry breaking yields the following mass terms for the four bosons:

$$m_{\text{Higgs}} = \lambda v \qquad m_{W^\pm} = \frac{1}{2} g v \qquad (2.1.20)$$

$$m_{Z^0} = \frac{1}{2} \sqrt{g^2 + g'^2} v \qquad m_\gamma = 0$$

Lepton masses can also be generated by interactions with the field ϕ

$$\mathcal{L} = - \sum_j^3 \left(\lambda_j \bar{E}_L^j \phi \cdot e_R^j + \text{h.c.} \right) \quad (\text{U}(1) \otimes \text{SU}(2) \text{ invariant}) \qquad (2.1.21)$$

$$= - \underbrace{\lambda_e \frac{v}{\sqrt{2}}}_{m_e} \bar{e}_L e_R - \underbrace{\lambda_\mu \frac{v}{\sqrt{2}}}_{m_\mu} \bar{\mu}_L \mu_R - \underbrace{\lambda_\tau \frac{v}{\sqrt{2}}}_{m_\tau} \bar{\tau}_L \tau_R + \mathcal{L}_{h\Psi_L\Psi_R}^{\text{interaction}} + \text{h.c.}, \qquad (2.1.22)$$

where after the symmetry breaking a mass term for the electron, muon and tau appears. For the quark masses the procedure is nearly equivalent. Starting with

$$\mathcal{L} = - \sum_i^3 \sum_j^3 \left(\lambda_d^{ij} \bar{Q}_L^i \phi \cdot d_R^j + \lambda_u^{ij} \epsilon^{ab} \bar{Q}_{L,a}^i \phi_b^\dagger u_R^j \right) + \text{h.c.} \qquad (2.1.23)$$

and applying the rotations $u_L^i \rightarrow U_u^{ij} u_L^j$ and $d_L^i \rightarrow U_d^{ij} d_L^j$, the Lagrangian density can be written in the quark mass eigenstates

$$\mathcal{L} = - \sum_i^3 \left(m_d^i \bar{d}_L^i d_R^i + m_u^i \bar{u}_L^i u_R^i \right) + \text{h.c.} \qquad (2.1.24)$$

For the interaction terms between quarks and W^\pm boson, this rewriting leads to

$$\mathcal{L}_{W^\pm}^{\text{interaction}} = \frac{e}{\sqrt{2} \sin \theta_W} \left(W_\mu^+ \bar{u}_L^i \gamma^\mu \underbrace{(U_u^\dagger U_d)^{ij}}_{=V^{ij}} d_L^j + \text{h.c.} \right), \quad g = \frac{e}{\sin \theta_W}, \qquad (2.1.25)$$

where V_{ij} is called the Cabibbo-Kobayashi-Maskawa (CKM) mixing matrix [62].

2.1.3 Quantum Chromodynamics

Quantum Chromodynamics is the description of the strong interactions in which only partons (quarks and gluons) can participate in. QCD demonstrates new effects through

its non-abelian $SU(3)$ gauge group. The coupling charge is called “color”. It features also a $SU(3)$ group with the triplet states “red”, “green,” and “blue”, but its coupling strength is equal for all charges.

Experiments have shown that no “free” quarks could be observed so far. This effect can be explained through a modified potential between quarks which leads to a “confinement”. Bounded states of quarks appear only in color singulets of mesons ($q\bar{q}$) or baryons (qqq). Moreover, it is possible to produce additional $q\bar{q}$ pairs from the vacuum if the potential exceeds $2 \cdot m_q$. This process of grouping and pair production is called “hadronization” and can not be calculated perturbatively.

However, QCD scattering processes can be calculated in a perturbative way through the behavior of the running coupling constant

$$\alpha_s(q^2) = \frac{\alpha_s(\mu_R^2)}{1 + \left(\alpha_s(\mu_R^2) \cdot \frac{33-2 \cdot n_f}{12\pi} \right) \cdot \ln \left(\frac{|q^2|}{\mu_R^2} \right)} \quad (2.1.26)$$

with μ_R as a measured reference scale and q^2 the scale to which the coupling is extrapolated. The number n_f counts the quark flavors. In strong interactions involving a large momentum scale the coupling goes to $\lim_{q \rightarrow \infty} \alpha_s(q^2) = 0$. Quarks are “asymptotically free” so that perturbative theory can be applied.

2.2 The Top Quark

In 1995, the top quark was first observed at the Tevatron collider in Chicago, USA [2]. It has by far the highest mass of $m_t = 173.5 \text{ GeV}$ [50] amongst all quarks. Therefore, it decays on a much shorter time scale which allows no hadronization. This makes it possible to probe the top quark and its properties directly.

The quark masses can not directly be measured due to non-perturbative effects of QCD at an energy scale $< 1 \text{ GeV}$. Only the top quark mass results from a direct measurement.

For this thesis, it is crucial that the spin orientation of the top quark stays encoded in its decay products and is not lost due to non-perturbative gluon radiation.

2.2.1 Top quark production and decay

Top quarks can be produced through strong or electroweak interactions. Figure 2.2 gives an overview of the different production channels. Top quarks are produced in $t\bar{t}$ pairs via strong interactions. The production in pairs follows from the flavor conservation. Single top quarks are produced by electroweak interactions. Here, the measured relation of the CKM matrix elements $V_{tb} \gg V_{ts}, V_{td}$ favors the production and decay of top quarks by a W boson and a bottom quark [34].

2.2 The Top Quark

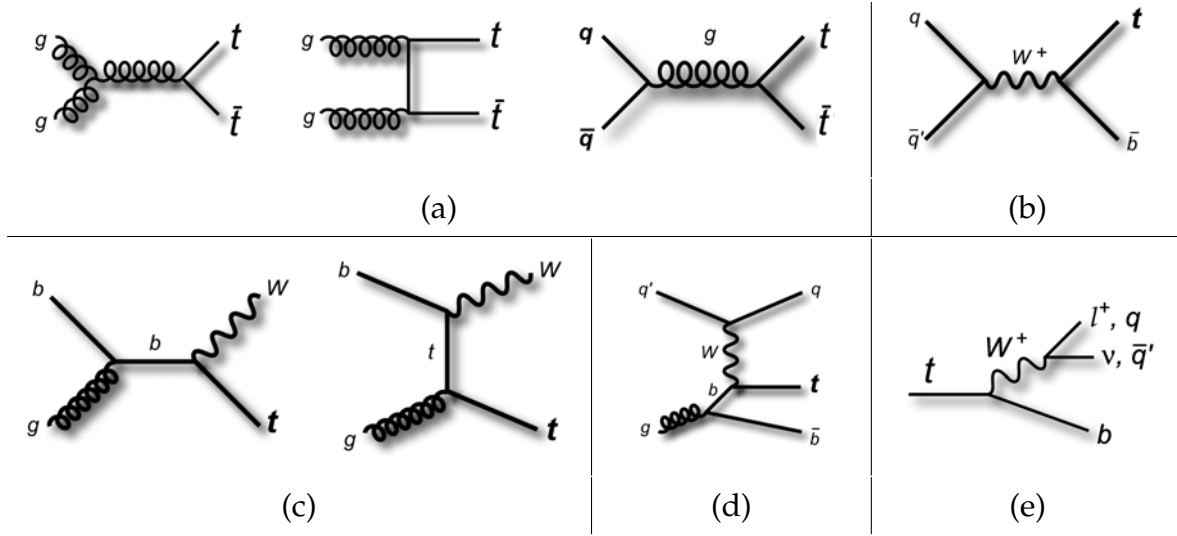


Figure 2.2: The production and decay of the top quark: (a) $t\bar{t}$ production; (b) s-channel production; (c) tW associated production; (d) t-channel production; (e) top decay. Figures were taken from Ref. [45].

2.2.2 Theoretical Results

In table 2.4, the theoretical calculated cross sections for the different top quark production processes are listed.

Table 2.4: Top quark cross sections. The cross sections are calculated for proton-proton collision at $\sqrt{s} = 7$ TeV in NNLO approximation.

$\sigma(t\bar{t})$	$163_{-8}^{+4}(\text{scale})_{-9}^{+9}(\text{pdf}) \text{ pb}$	[53]
$\sigma(\text{t-channel single top})$	$64.57_{-0.71}^{+2.09}(\text{scale})_{-1.74}^{+1.51}(\text{pdf}) \text{ pb}$	[55]
$\sigma(\text{s-channel single top})$	$4.63 \pm 0.07(\text{scale})_{-0.17}^{+0.19}(\text{pdf}) \text{ pb}$	[52]
$\sigma(\text{tW-channel single top})$	$15.74 \pm 0.40(\text{scale})_{-1.14}^{+1.10}(\text{pdf}) \text{ pb}$	[54]

Measuring the top quark production cross sections and its properties is essential for understanding the electroweak symmetry breaking, since the top quark mass is in the vicinity of the Higgs potential vacuum expectation value $v = (\sqrt{2}G_F)^{-1/2} \approx 246.22 \text{ GeV}$ ¹. Furthermore, new heavy particles are predicted by various extensions to the SM like Super SYmmetry (SUSY) or extra dimension models. Those particles can decay into top quarks which changes the expected SM cross sections. Also, loop corrections involving new particles or interactions may alter the V-A coupling structure.

¹ G_F denotes the Fermi constant, which can be measured in muon decays [10].

2.3 Effective Theory

2.3.1 Anomalous Couplings

The effects of new particles or interactions to the top quark electroweak couplings can be parametrized by using the Operator Product Expansion (OPE) [62]. New products of operators may arise from new interactions at a higher energy scale Λ . Those can be developed around their spatial separation

$$\mathcal{O}_1(x)\mathcal{O}_2(0) \rightarrow \sum_j C_{12}^j(x)\mathcal{O}_j(0), \quad (2.3.1)$$

with the complex functions $C_{12}^j(x)$. For the SM Lagrangian, this can be understood as

$$\mathcal{L} \rightarrow \mathcal{L}_{\text{eff}} = \mathcal{L}_{\text{SM}} + \sum_{d>4, j} \frac{C_j^{(d)}}{\Lambda^{d-4}} \cdot \mathcal{O}_j^{(d)} + \text{h.c.} \quad (2.3.2)$$

where d denotes the “mass dimension” [4, 9]. For $d = 6$ this leads to leading order contributions to the SM. In the case of the top quark, the SM Lagrangian density

$$\mathcal{L}_{\text{Wtb}}^{\text{SM}} = -\frac{g}{\sqrt{2}} \bar{b} \gamma^\mu V_{\text{tb}} P_L t W_\mu^- + \text{h.c.} \quad (2.3.3)$$

can be extended in an effective coupling scenario at the Wtb-vertex [6]:

$$\begin{aligned} \mathcal{L}_{\text{Wtb}}^{\text{eff}} = & -\frac{g}{\sqrt{2}} \bar{b} \gamma^\mu (V_L P_L + V_R P_R) t W_\mu^- & (\text{vector couplings}) \\ & -\frac{g}{\sqrt{2}} \bar{b} \frac{i\sigma^{\mu\nu} q_\nu}{m_W} (g_L P_L + g_R P_R) t W_\mu^- + \text{h.c.} & (\text{tensor couplings}) \end{aligned} \quad (2.3.4)$$

The scale dependence Λ is absorbed into the new coupling strength parameters V_R , g_L and g_R . The SM is obtained by setting $V_L = V_{\text{tb}} \approx 1$ and $V_R = g_L = g_R = 0$. V_R introduces a new right-handed vector anomalous coupling and g_L , g_R new tensor left-, right-handed anomalous couplings.

2.3.2 W Boson Helicity Fractions

One way of probing the presence of anomalous couplings at the Wtb-vertex is by analyzing the W boson helicity fractions. The W boson spin is quantized along its momentum in the top quark rest frame. The angle between the lepton in the W boson rest frame and the quantized spin, $\cos \theta^*$, then follows the distribution

2.3 Effective Theory

$$\begin{aligned} \frac{d\Gamma}{\Gamma \cdot d\cos\theta^*} = & \frac{3}{8} (1 + \cos\theta^*)^2 \cdot F_+ + \frac{3}{8} (1 - \cos\theta^*)^2 \cdot F_- \\ & + \frac{3}{4} \sin^2\theta^* \cdot F_0, \end{aligned} \quad (2.3.5)$$

where the angle is calculated through

$$\cos\theta^* = \frac{\vec{p}_W^{(\text{top})} \cdot \vec{p}_{\text{lepton}}^{(W)}}{|\vec{p}_W^{(\text{top})}| |\vec{p}_{\text{lepton}}^{(W)}|}. \quad (2.3.6)$$

$F_j \equiv \frac{\Gamma_j}{\Gamma}$ denotes the W boson helicity fractions [5]. Figure 2.3 shows the described spin quantization and angle.

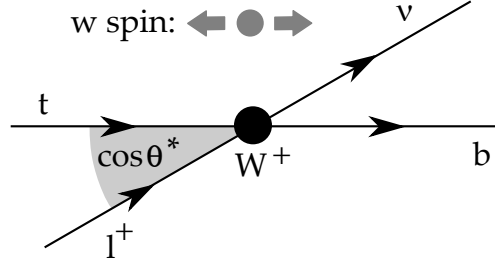


Figure 2.3: Quantization of the W boson spin.

F_{\pm} corresponds to positive/negative W boson helicity $H = \pm 1$ and F_0 to the transversal orientation of the spin ($H = 0$). In the effective extension, the fractions depend on the anomalous couplings $F_j = F_j(V_L, V_R, g_L, g_R)$. By measuring F_j , the couplings can be constrained.

2.3.3 Top Spin Asymmetries

Further observables to constrain anomalous couplings can be obtained by quantizing the top quark spin directly in electroweak production. In single top quark t-channel production it is however challenging to reconstruct the center-of-mass system in the presence of additional jets with high precision. Thus a different quantization axis has to be found.

It has been shown in Ref. [13] that choosing the direction of the spectator quark as the top quark spin axis yields a high polarization ρ . This leads to the following distribution

$$\frac{d\Gamma}{\Gamma \cdot d\cos\theta_{B,X}} = \frac{1}{2} (1 + \rho_B \cdot c_X \cdot \cos\theta_{B,X}), \quad \cos\theta_{B,X} = \frac{\vec{p}_B^{(\text{top})} \cdot \vec{p}_X^{(\text{top})}}{|\vec{p}_B^{(\text{top})}| |\vec{p}_X^{(\text{top})}|}. \quad (2.3.7)$$

The polarization

$$\rho_B = \frac{N_{\uparrow} - N_{\downarrow}}{N_{\uparrow} + N_{\downarrow}} \quad (2.3.8)$$

denotes the degree of how much the top spin actually coincide with the direction of a chosen basis B. The spectator basis yields an expected polarization of $\rho_{\text{spec.}}^t = 99\%$, and $\rho_{\text{spec.}}^{\bar{t}} = -96\%$. Another basis with high polarization can be constructed by projecting the spectator quark along the beamline. The polarizations are $\rho_{\text{bml.}}^t = 96\%$, and $\rho_{\text{bml.}}^{\bar{t}} = -97\%$ [13].

The factor c_X is called “spin analyzing power” and depends on the anomalous couplings [5]. The “spin analyzer” X can be each decay product of the top quark. If the W boson decays leptonically, one can choose the lepton, bottom quark and the neutrino as independent spin analyzers c_l , $c_b = -c_W$, and c_ν . Figure 2.4 visualizes the construction of the different angles in the top rest frame. Like the W boson helicity fractions, those spin analyzing powers can be considered as fundamental quantities. However, the differential cross section in equation 2.3.7 depends on the product of the polarization and the spin analyzing power. Therefore, the spin analyzing powers can not be measured directly.

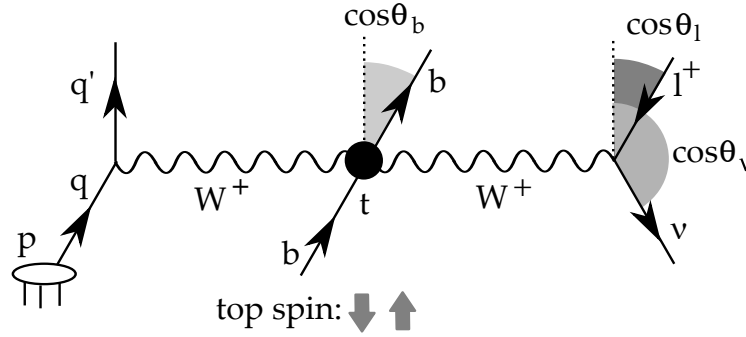


Figure 2.4: Quantization of the top quark spin.

In this thesis, the top spin asymmetries which are related to the product $\rho \cdot c_X$ will be measured. These are defined as follows:

$$A_X^B = \frac{N(\cos \theta_{B,X} > 0) - N(\cos \theta_{B,X} < 0)}{N(\cos \theta_{B,X} > 0) + N(\cos \theta_{B,X} < 0)} = \frac{1}{2} \rho_B \cdot c_X(V_L, V_R, g_L, g_R) \quad (2.3.9)$$

In total, three asymmetries, each in two bases, can be constructed. Table 2.5 gives an overview of the expected asymmetries in the SM case. The values are analytically calculated using equations for the spin analyzers from Ref. [5]. The polarizations for t and \bar{t} have been averaged according to their production cross sections.

2.4 The WHIZARD Monte Carlo Generator

Table 2.5: The expected top quark spin asymmetries if the SM couplings are considered.

	asymmetries A_X^B		
	muon: $c_l = 1.00$	bottom quark: $c_b = -0.39$	neutrino: $c_\nu = -0.34$
spectator basis	0.49	-0.19	-0.17
beamline basis	0.48	-0.19	-0.16

In the context of the effective SM extension, the analysis of the top quark spin asymmetries gives a model independent new insight into the coupling structure at the Wtb -vertex.

2.4 The WHIZARD Monte Carlo Generator

To simulate events with anomalous top quark couplings, the WHIZARD [56] Monte Carlo generator is used. It has been designed for efficient calculation and simulation of multi-particle scattering. Matrix elements for leading order processes are automatically generated as needed by the integrated O'Mega matrix element generator. The steering is performed through a script file written in the domain-specific language SINDARIN.

Besides the SM, other models like the minimal supersymmetric Standard Model (MSSM), little Higgs models, anomalous coupling models and more are available.

Experimental Setup

3.1 The Large Hadron Collider

The Large Hadron Collider (LHC) is a proton-proton storage ring at the European Organization for Nuclear Research (CERN) in Geneva, Switzerland. It is built underground and has a circumference of approximately 27 km. The performance goal is a center-of-mass energy of $\sqrt{s} = 14$ TeV at a luminosity of $L = 10^{34} \frac{1}{\text{cm}^2\text{s}}$ [41]. The proton beams can also be switched to ion beams. Here, the aimed peak luminosity is $L = 10^{27} \frac{1}{\text{cm}^2\text{s}}$ at $\sqrt{s} = 2.76$ TeV [41]. Figure 3.1 shows the accelerator complex with the LHC, its experiments and the pre-accelerator chain.

The acceleration of protons starts at the Linac2. It continues with the Proton Synchrotron Booster (PSB), the Proton Synchrotron (PS), the Super Proton Synchrotron (SPS), and finally the protons are injected into the LHC at an energy per proton of 450 GeV [41].

After filling the LHC ring, the proton beams consist of maximally 2808 bunches with a spacing of 25 ns between them. With $1.15 \cdot 10^{11}$ protons per bunch, the current per beam is $I = 0.58$ A.

A magnet system of NbTi superconductors is used for deflecting and focusing the beams. Superfluid helium cools the superconductors down to 1.9 K. This allows the dipole magnets to be driven with a current of 11850 A. The dipole magnets produce a magnet field of 8.33 T. Magnets for both beams are integrated into one cold mass inside the cryostats (“twin-bore” design). 1232 dipole magnets are needed for deflection. Additionally, around 450 quadrupole magnets are installed for focusing and approximately 4800 magnets are installed for orbit correction.

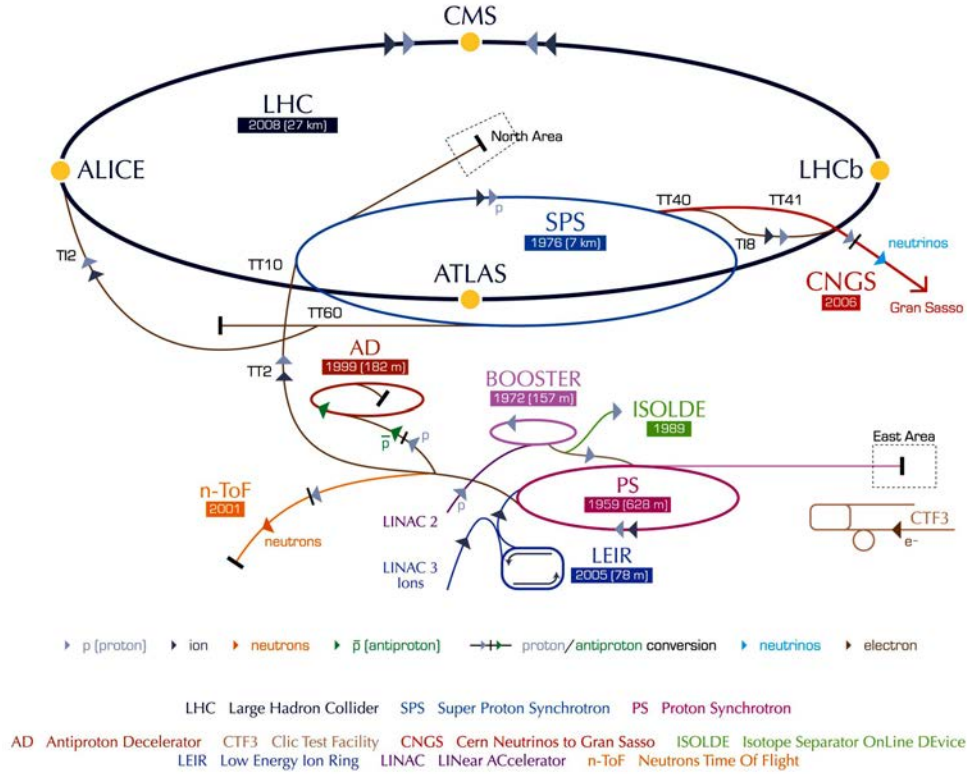
A superconducting cavity system operating at 400 MHz is used for accelerating. The protons within the beams gain an energy of 485 keV per turn which yields an acceleration time from injection energy at 450 GeV to 7 TeV per beam of around 20 min [41].

Four major experiments are using the LHC beam collisions for analysis:

- ALICE (A Large Ion Collider Experiment) is a detector for studying heavy-ion collisions and the properties of quark-gluon plasma.
- ATLAS is a general purpose detector with a special donut-shaped magnet system. Its scientific program covers the physics of the Higgs boson, super-symmetry, extra dimensions and SM precision measurements besides others.
- CMS (Compact Muon Solenoid) is also a general purpose detector with a wide-

3.1 The Large Hadron Collider

CERN's accelerator complex



European Organization for Nuclear Research | Organisation européenne pour la recherche nucléaire

© CERN 2008

Figure 3.1: The CERN accelerator complex [58].

ranging physics program. Its design involves different technical solutions compared to ATLAS.

- LHC-b (Large Hadron Collider beauty Experiment) has a forward sub-detector system. Besides others, it probes the CP violation in B hadrons.

After a breakdown during the first tests in September 2008, the full operation of the LHC started on 20th November 2009 with successfully circulating beams at injection energy. In March 2010, the targeted beam energy of 3.5 TeV for the first run period of 2010 had been established [61]. In 2011, the proton-proton run program at $\sqrt{s} = 7$ TeV finished with a delivered integrated luminosity of 5.57 fb^{-1} for ATLAS and 5.73 fb^{-1} for CMS [43]. In 2012, the center-of-mass energy has been raised to $\sqrt{s} = 8$ TeV.

3.2 The CMS Experiment

The Compact Muon Solenoid (CMS) is a general-purpose detector developed to detect and record the proton-proton collisions at the high luminosity that the LHC provides. The physics program of the CMS collaboration involves the search for the Higgs boson, the discovery or exclusion of supersymmetric particles (SUSY), new heavy vector bosons, and extra dimensions. Besides that, precision measurements of the SM are performed, e.g. like studies of QCD, electroweak and top quark physics. During heavy-ion runs, the properties of strongly-interacting nuclear matter are investigated.

The CMS detector has been designed with a cylindrical symmetry around the beam pipe. It is 21.5 m long and has a diameter of 14.6 m. Figure 3.2 shows the CMS detector and its subsystems which are mainly the inner tracker (pixel and silicon tracker), the electromagnetic calorimeter, the hadron calorimeter, the superconduction solenoid, and the muon detectors.

CMS uses the following coordinate system. The interaction point (IP) is the origin. The z-axis matches the beamline. The x-axis points towards the center of the LHC ring and the y-axis points upwards, orthogonal to x and z. To reflect the cylindrical symmetry of the detector, one instead often uses the pseudorapidity $\eta = -\ln\left(\tan\frac{\theta}{2}\right)$ with the azimuthal angle θ between the z-axis and the xy-plane, and the polar angle ϕ inside the xy-plane.

The next paragraphs will briefly describe the main systems of the detector starting from the IP.

Inner tracking system Around the IP, the tracking system is placed. It is 540 cm long and has an outer radius of $r = 110$ cm.

The system itself is divided into three regions. This is due to the expected particle flux which decreases radially. At $r \approx 10$ cm pixel detectors are placed with a size of $100 \times 150 \mu\text{m}^2$. In the next region around $20 < r < 55$ cm, silicon microstrip detectors can be used due to the lower particle flux. They have a minimal cell size of $10 \text{ cm} \times 80 \mu\text{m}$. In the last region of the tracking system, larger-pitch silicon microstrips are installed. Their cell size is at minimum $25 \text{ cm} \times 180 \mu\text{m}$. With these components, the tracking system is able to reconstruct particle tracks even in the high particle density environment of heavy-ion collisions.

Electromagnetic calorimeter The electromagnetic calorimeter (ECAL) is composed out of lead tungstate (PbWO_4) scintillating crystals. The crystal material was chosen due to its fast response time (within 25 ns) and radiation hardness (up to 10 Mrad). 61200 crystals are installed in the central barrel part and an additional 7324 crystals are

3.2 The CMS Experiment

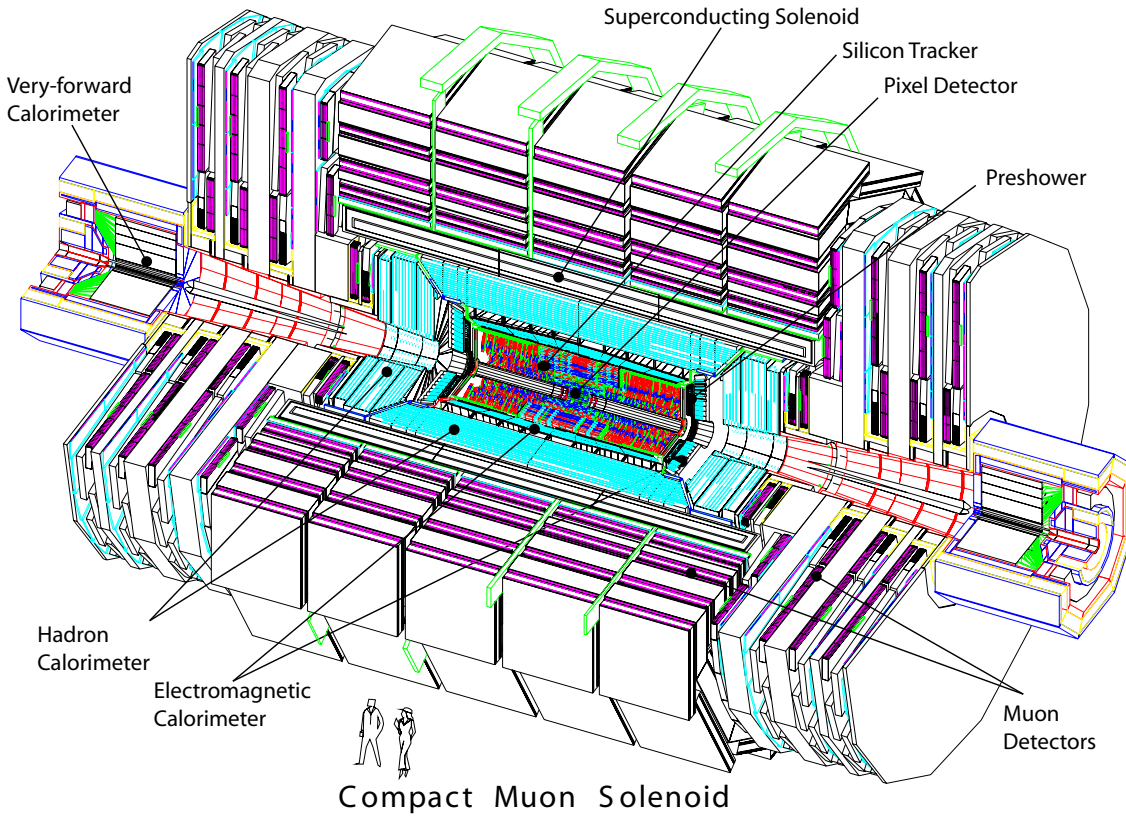


Figure 3.2: The CMS detector and its subsystems [11].

placed in each of the two endcaps. The light yield of the crystals is rather low. Therefore, photodetectors with intrinsic gain are applied. For amplification, silicon avalanche photodiodes (APDs) are used in the barrel, and vacuum phototriodes (VPTs) are used in the endcaps.

The complete ECAL covers a pseudorapidity range of $|\eta| \leq 3.0$. The transition region between barrel and endcap is at $|\eta| = 1.479$.

Its energy resolution can be parametrized [37] as

$$\left(\frac{\sigma_E^2}{E} \right) = \underbrace{\left(\frac{2.8\% \cdot \sqrt{E}}{\sqrt{E}} \right)^2}_{\text{stochastic term}} + \underbrace{\left(\frac{0.12 \text{ GeV}}{E} \right)^2}_{\text{noise term}} + \underbrace{(0.3\%)^2}_{\text{constant term}} . \quad (3.2.1)$$

Hadron calorimeter The hadron calorimeter (HCAL) surrounds the the ECAL system. It is divided into four parts:

The hadron barrel (HB) is installed inside the magnetic coil, and covers a pseudo-

rapidity range of $|\eta| \leq 1.4$. The hadron outer (HO) is located at the outer vacuum tank of the coil. It has a range of $|\eta| \leq 1.26$. The hadron endcap (HE) can measure in a pseudorapidity range of $1.3 \leq |\eta| \leq 3.0$ and the hadron forward (HF) covers a pseudorapidity range of $3.0 \leq |\eta| \leq 5.0$.

The HCAL consists of brass as absorber material which has a short interaction length. It provides a good particle containment, which is needed for the detection of missing transverse energy. To maximize the absorber space inside the barrel, plastic scintillator tiles with embedded wavelength-shifting (WLS) fibers are used as active medium. They require only a minimum of space to carry the light to the readout system of multi-channel hybrid photodiodes (HPDs).

The HCAL in combination with the ECAL can measure hadrons with a resolution of

$$\left(\frac{\sigma_E}{E}\right)^2 \approx \left(\frac{100\% \cdot \sqrt{E}}{\sqrt{E}}\right)^2 + (5\%)^2. \quad (3.2.2)$$

More about the HCAL performance and how it affects the missing transverse energy resolution can be found in Ref. [31].

Solenoid coil A large superconducting solenoid coil for bending of charged particle tracks is used. Supplied with a current of 19.5 kA, it generates a field of 3.8 T at the IP. This provides a momentum resolution of

$$\frac{\Delta p}{p} \approx 10\% \quad (\text{at } p = 1 \text{ TeV}) \quad (3.2.3)$$

which can unambiguously determine the charge of a muon up to $p = 1 \text{ TeV}$ [11].

Muon system Muons originating from the IP are measured with two detector subsystems: the inner tracker in the inner magnetic field and the muon system in the outer magnetic field. The inner tracker can only measure muon momenta with a good resolution up to round 200 GeV. Therefore, the muon system is combined with the inner tracker to the “full system”, which leads to a precise muon resolution over a wide momentum range.

The muon system itself consists of three types of gaseous detectors to cover the large detector surface throughout the different radiation environments. Drift tube (DT) chambers are installed in the barrel region of $|\eta| \leq 1.2$ where the magnetic field and the neutron background is low. In the two endcaps, cathode strip chambers (CSCs) are used. These can operate in the presence of the high magnetic field and neutron background. The endcaps cover a region up to $|\eta| \leq 2.4$. Both systems however lack in time resolution. Additionally, resistive plate chambers (RPCs) are deployed in both

3.2 The CMS Experiment

regions. Driven in avalanche mode, they complete the muon system by providing a good time resolution.

Trigger and data acquisition For the preselection of around 10^9 interactions per second at design luminosity, a trigger system is used to single out the interesting events. This lowers the data rate to $\approx 10^2$ event per second. At this rate, it is possible to store the data on archival media. The data flow through the trigger system is depicted in figure 3.3.

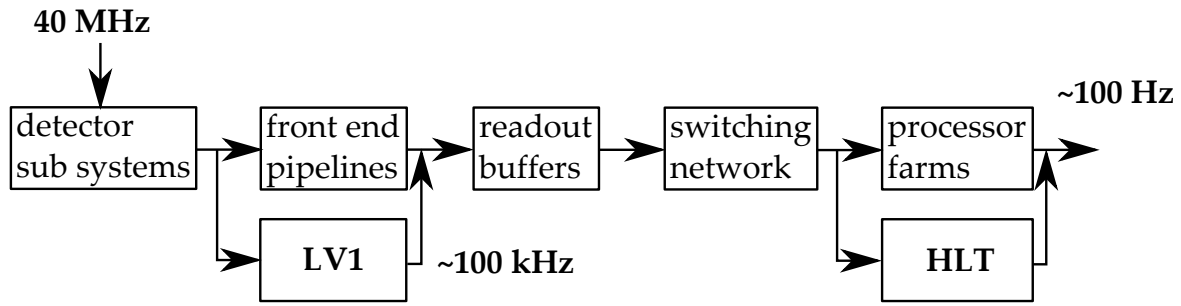


Figure 3.3: The CMS trigger system.

Starting at a bunch crossing rate of 40 MHz, the detector data is first written into a buffer. Within $3.2 \mu\text{s}$ all data is collected from the subsystems, and a decision has to be made whether to keep or reject the event. The Level-1 (LV1) trigger operates in parallel to the buffering. It reaches a decision within $1 \mu\text{s}$ by using only the calorimetry and muon system readouts. The logic behind the decision needs to be executed very fast and is therefore implemented into custom Application Specific Integrated Circuits (ASICs), Field Programmable Gate Arrays (FPGAs), and Programmable Logic Devices (PLDs), amongst others.

After passing the Level-1 trigger, the complete event in the buffer has a size of about 1.5 MB and is transferred to the processor farm. Here, the more complex High Level Trigger (HLT) software decides if the event is stored. By reconstructing the full event data that uses all detector sub systems, it further singles out interesting events and reduces the rate from 100 kHz down to approximately 100 Hz.

The recorded data is stored at the “Tier-0” center and copied to the “Tier-1” and “Tier-2” centers of the Worldwide LHC Computing Grid (WLCG) to be accessed from experimentalists around the world [11].

3.3 Reconstruction of Physics Objects

3.3.1 The Particle-Flow Algorithm

The Particle-Flow (PF) algorithm aims at precisely identifying particle types and their momenta by exploiting all detector sub systems. It creates particle hypotheses within an event by combining information from charged-particle tracks, calorimetry hits, and muon tracks [22].

The algorithm starts with the tracker information by first selecting tracks with very tight criteria originating closely from the IP. Iteratively looser criteria are applied for the selection of the remaining tracks. In the calorimeters, hits are clustered. This is performed by finding cells with high energy maxima (“cluster seeds”). Then, “topological clusters” are constructed by combining the seeds with adjacent cells if they measured an energy over a certain threshold.

One expects that a particle leads to a charged-particle track, and/or hits several calorimeter clusters, and leads to one or no track in the muon system. These pieces of information are linked to reconstruct each single observed particle.

3.3.2 Muon Identification

Muons are identified in three ways:

1. For muons with low momenta, the “Tracker Muon” is defined by extrapolating tracker tracks into the muon system. For this, energy loss and possible multiple scattering of muons from the tracker to the muon system are taken into account. At least one segment of the muon system (DT or CSC) needs to be in coincidence with the extrapolation to claim this muon hypothesis.
2. A “Global Muon” is reconstructed through a fit to the inner tracker and the muon system data. This combination method improves the muon momentum resolution above a transverse momentum of 200 GeV.
3. The “Standalone-Muon track only” is claimed if both previously described methods fail. This is the case if the muon is observed only in the muon system. Due to the high tracker efficiency, those muons often originate from cosmic rays and not from an interaction at the IP [26].

The PF algorithm categorizes the muons further. If the energy deposit in a cone of $\sqrt{\Delta\eta^2 + \Delta\phi^2} < 0.3$ around the muon track is less than 10% of the muon’s transverse momentum, the muon is labeled “isolated”. The remaining “non-isolated” muons are labeled “loose” [23].

3.3.3 Missing Transverse Energy

After the PF reconstruction, the missing transverse energy is calculated. Due to the conservation of momentum, the net transverse momentum should be zero after a collision. One can obtain the missing transverse energy from the net momentum of all reconstructed particles.

Depending on the physics analysis, the missing transverse energy may hints about particles that cannot be detected directly in CMS, e.g. like neutrinos or SUSY particles.

3.3.4 Jet Definition

A jet is a group of particles originating from hadronization of partons. Jet algorithms are used to group reconstructed particles to jets. By summing up the momenta within a jet, an inference about the parton momentum can be made.

Nowadays, the mainly used jet algorithms are the k_T , the anti- k_T , and the Seedless Infrared-Safe Cone (SIS-Cone) algorithms [19, 65]. Each one is considered infrared- and collinear-safe. Figure 3.4 shows exemplary scenarios to explain these two necessary safety features.

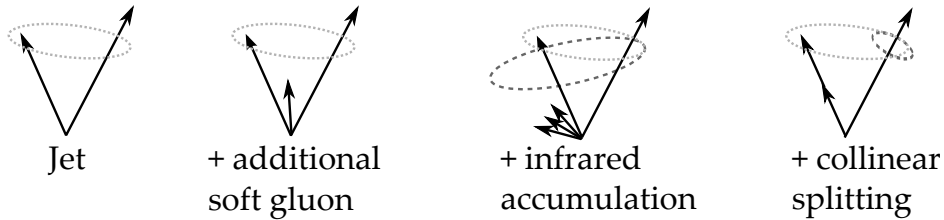


Figure 3.4: Jet definition in different scenarios of additional particles. The dark dotted gray ellipses show the result if not an infrared- and collinear-safe algorithm is used.

Soft gluons which are emitted from a parton during the hadronization produce additional particles with low momenta that should be clustered into the jet. However, lowly energetic particles originating from other interactions should be omitted. This infrared accumulation may sum up and has a significantly incorrect input to the jet. Suppressing this behavior by setting a minimum momentum threshold (“seed”) for the clustering will lead to the wrong result in the collinear limit. Here, jet algorithms should not change their result, if one particle with high momentum is splitted into many collinear particles.

In the CMS jet reconstruction, the anti- k_T algorithm is used. It operates on “proto-jets” which are initially the reconstructed particles. Its core procedure is the iterative calculation of the distances

$$d_{ij} = \min \left(\frac{1}{p_{T,i}^2}, \frac{1}{p_{T,j}^2} \right) \cdot \frac{\Delta_{ij}}{R^2} \quad (3.3.1)$$

and

$$d_i = \frac{1}{p_{T,i}^2} \quad (3.3.2)$$

between all proto-jets i and j . $\Delta_{ij} = \sqrt{\Delta\eta^2 + \Delta\phi^2}$ denotes the distance in the $\eta\phi$ -plane between the two proto-jets and p_T denotes their transverse momenta. After the first calculation of the two distances d_{ij} and d_i , a proto-jet i is considered as a jet if $d_i < d_{ij}$. This jet is then removed from the next iteration. In the case of $d_i > d_{ij}$, the two proto-jets i and j are merged to a new proto-jet by summing their four-momenta $p^{\text{new}} = p^i + p^j$. The algorithm continues until all proto-jets have been considered as jets. Hereby, the parameter R controls the cone sizes of the resulting jets.

3.3.5 Identification of Jets from b-Quarks

Jet algorithms can not determine the original flavor of a hadronized quark. However, the relatively long decay time of B hadrons can be exploited for identifying jets that originate from bottom quarks. In a proton-proton collision, the hard interaction is often boosted with respect to the lab frame. If a long-lived particle such as a B hadron is produced, it will fly a measurable distance d from the primary interaction vertex before decaying.

The CMS reconstruction uses, amongst others, the track-counting method. A “b-tag” discriminator is constructed by using the significance $\frac{\sigma_d}{d}$ that the n -th good track of a jet is not from the primary vertex [64]. In the analysis the track counting algorithm is used, which is based on the significance of the third track of a jet.

3.4 Analysis Software

For performing the analysis in this thesis, various software packages have been used.

3.4.1 CMS Software Framework

The CMS software (CMSSW) framework provides a collection of software packages for simulation and reconstruction [51]. The event data model (EDM) acts as a common interface between the different packages.

3.4 Analysis Software

A analysis with CMSSW is configured by a script file which specifies the inputs and outputs as well as the intermediate analysis module chain. This script file is passed to the “cmsRun” executable.

For splitting and running large numbers of CMSSW analyses on the WLCG, the CMS remote analysis builder (CRAB) provides a convenient configuration and submission of analyses as well as their status tracking [68].

For this analysis, the CMSSW version 4.2.8 is used for the event reconstruction, selection, and simulation.

3.4.2 THETA

The THETA framework provides tools for template-based statistical modeling and inference [60]. A model is defined by a set of histograms (templates), parameters, and observables. As an example, a simple observable O within a model is constructed by

$$O(p_1, p_2, \dots p_n) = \sum_i t_i \cdot p_i \quad (3.4.1)$$

with the templates t_i and the parameters p_i . THETA provides then various methods to perform a statistical inference by e.g. comparing models with data. THETA is able to perform frequentist or Bayesian methods including maximum likelihood estimator (MLE) and marginalization using Markov-Chain Monte-Carlo (MCMC) methods besides others.

In the analysis, THETA is used to generate pseudo experiments for propagation of uncertainties and to obtain a data-driven yield estimate through a fit.

3.4.3 ROOT

ROOT is a C++ framework for various tasks [17]. It is used for analyzing, plotting, storing, and monitoring data in many high energy physics experiments and analyses. For example, the main file format for data exchange in CMSSW is a ROOT tree structure.

3.4.4 Toolkit for Multivariate Data Analysis with ROOT

The Toolkit for Multivariate Data Analysis with ROOT (TMVA) is a C++ analysis framework [49]. It hosts various algorithms for multivariate classification. In high energy physics, such classifications in high dimensional spaces are often used to further discriminate between signal and background events after preselection.

To set up a discriminator for classification, the classifier algorithm is first trained and tested with simulated signal and background events. For evaluation, statistically

independent simulated samples are needed to allow a bias-free comparison with actual data.

The next paragraphs describe the “Projective Likelihood Estimator” and the “Boosted Decision and Regression Tree” algorithms, which are applied in this analysis.

Projective Likelihood Estimator (PLE) For each event in the evaluation, the Likelihood ratio

$$y_L(i) = \frac{L_S(i)}{L_S(i) + L_B(i)} \quad (3.4.2)$$

is defined. $L_{S(B)}$ is the product probability over all input variables from the training that the event is signal- (background-) like. The resulting classifier ranges from 0 (background-like) to 1 (signal-like).

This method has been chosen because it is not sensitive to correlations within the input variables.

Boosted Decision Tree (BDT) A decision tree tries to identify signal- or background-like phase spaces within the n -dimensional input variables space. This is performed by sequentially cutting on the variables to select a signal enhanced region. However, a single trained decision tree can be very unstable due to statistical fluctuations in the training samples. Therefore, many decision trees are constructed. A stabilized discriminator is derived by a majority vote over all trees. Boosting increases the discriminator stability further by applying additional weight factors for each decision tree based on its classification performance. The Boosted Decision Tree (BDT) discriminator can be written as

$$y(\vec{x}) = \frac{1}{N_{\text{trees}}} \cdot \sum_j^{N_{\text{trees}}} \ln(\alpha_j) \cdot h_j(\vec{x}), \quad (3.4.3)$$

where N_{trees} counts the number of decision trees. The decision result of an individual tree is h_j for an event \vec{x} which takes the values $h_j = 1$ for signal-like and $h_j = -1$ for background-like events. α_j notes the additional boosting weight.

The used AdaBoost algorithm calculates the weights α_j from the misclassification rate ϵ by

$$\alpha = \frac{1 - \epsilon}{\epsilon}. \quad (3.4.4)$$

Through the normalization to $\sum \alpha_j = \text{const}$, the BDT discriminator ranges between -1 and 1 .

3.4 Analysis Software

The BDT has been chosen for its stability and high discrimination power. It exploits also correlations between the input variables.

3.4.5 VISPA and PXL

Visual Physics Analysis (VISPA) is a development environment for physics analyses. It utilizes the C++ toolkit Physics eXtension Library (PXL) for designing modular analyses [16]. Within the software, the user can write C++ or Python modules and connect them graphically to create a complex analysis logic. During runtime, data objects are passed along these connections to the user modules. The data objects trigger methods within the modules where the user code is executed.

Data objects are stored in the PXLIO file format. There are various converters available to read Comma-Separated Values (CSV) files, the Les Houches Event format, and the data formats from the experiments CMS, ATLAS, Pierre Auger, and ILC, besides others.

Through the multifaceted areas of application, VISPA is used during this analysis for generator validation, event selection, multivariate classification training and evaluation, and for coordination and analysis of THETA runs and results.

Event Selection and Simulation

Single top quark t-channel events are simulated for comparison with data. Also background processes with the same signature need to be included in the analysis. The signature of the single top quark t-channel production with leptonically W boson decay (signal process) involves two jets, where one of the jets is required b-tagged, a lepton and missing transverse energy (MET) through the escaping neutrino. Figure 4.1 shows the experimental signature of the single top quark t-channel production.

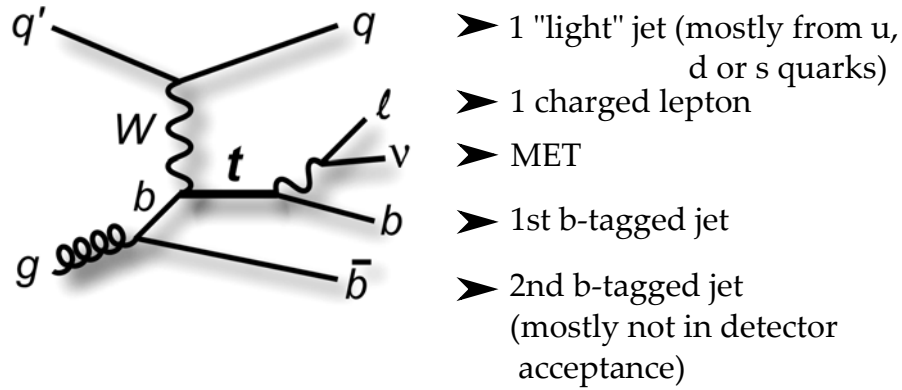


Figure 4.1: Signature of single top quark t-channel production with leptonically decaying W boson .

The signature includes also a second jet with a b-tag. This second jet mostly escapes the detector acceptance because most of its momentum comes from one of the colliding protons. The jet without a b-tag originates often from up, down or strange quarks and is therefore referred to as "light" jet. Additionally, it is often labeled "spectator" because it is not involved in the interaction to produce the top quark at the Wtb -vertex.

This analysis within this thesis focuses on single top quark t-channel events with W bosons decaying into a muon and neutrino. This channel can be measured more precisely and more efficiently than the decay into an electron or tau and a neutrino.

In this chapter, the simulated samples, the dataset and the event selection and reconstruction are described.

4.1 The Simulated Standard Model Samples

4.1 The Simulated Standard Model Samples

The used SM samples for signal and background processes are listed in Table 4.1. Simulated events from the Monte Carlo (MC) generators MadGraph [8], Powheg [7] and Pythia6 [67] have been subjected to a hadronization simulation by interfacing with Pythia6. Then, after passing a Geant4-based [3] simulation of the CMS detector, the resulting events are reconstructed and can be compared to recorded data.

process	generator	simulated events	cross section in pb
single top quark t-channel (t)	Powheg	3900171	41.92 [55]
single top quark t-channel (\bar{t})	Powheg	1944826	22.65 [55]
single top quark s-channel (t)	Powheg	259971	3.19 [52]
single top quark s-channel (\bar{t})	Powheg	137980	1.44 [52]
single top quark tW-channel (t)	Powheg	814390	7.87 [54]
single top quark tW-channel (\bar{t})	Powheg	809984	7.87 [54]
QCD multijet (μ enriched)	Pythia6	25080241	84679 ^(*)
$t\bar{t}$	MadGraph	3701947	157.5 [53]
$W(\rightarrow l\nu) + \text{jets}$	MadGraph	81352581	31314 [59]
$W(\rightarrow l\nu) + \text{exclusive 1 jets}$	MadGraph	76042128	matched to inclusive
$W(\rightarrow l\nu) + \text{exclusive 2 jets}$	MadGraph	25424787	matched to inclusive
$W(\rightarrow l\nu) + \text{exclusive 3 jets}$	MadGraph	7685944	matched to inclusive
$W(\rightarrow l\nu) + \text{exclusive } \geq 4 \text{ jets}$	MadGraph	13133738	matched to inclusive
$Z/\gamma^*(\rightarrow l^+l^-) + \text{jets}$	MadGraph	36277961	3048 [59]
WW	Pythia6	4225916	47.04 [20]
WZ	Pythia6	4265243	18.57 [20]
ZZ	Pythia6	4187885	6.46 [20]

Table 4.1: The simulated SM samples.^(*) Cross section has been calculated by Pythia6.

There are two ways to theoretically define the “single top quark tW-channel” process: diagram removal [70], and diagram subtraction [12]. This ambiguity is due to the methodology how the interference effects with the $t\bar{t}$ production in next to leading order are treated. In the analysis, the diagram removal samples are used.

The inclusive $W(\rightarrow l\nu) + \text{jets}$ sample is enriched in statistics by adding exclusive

contributions from the W boson plus one to four additional jet events. Furthermore, the $W(\rightarrow l\nu) + \text{jets}$ samples are mainly dominated by light flavored jets. The signal selection requires however a b-tagged jet. This selection criterion enriches the selected data with W plus heavy flavored jet content (“heavy” = c, b quarks). The inclusive and exclusive $W(\rightarrow l\nu) + \text{jets}$ events are sorted into the following three categories with respect to their flavor content to gain confidence into the flavor modeling:

- “W+bX” are all events with at least one bottom quark during generation.
- “W+cX” are the remaining events with at least one charm quark during generation.
- “W+light jets” are all other events without a bottom or charm quark.

This splitting is also performed for the $Z/\gamma^*(\rightarrow l^+l^-) + \text{jets}$ sample which leads to the naming scheme “Z+bX”, “Z+cX”, and “Z+light jets” (alternatively “DY+light jets”).

4.2 Simulated Signal Events with WHIZARD

The WHIZARD event generator [56] is used for the simulation of single top quark t-channel events with anomalous couplings. Such samples are needed to test the analysis strategy and to evaluate if the event selection introduce a potential bias on those scenarios.

The generator provides a pre-implemented model called “SM_top_anom” where the anomalous top quark couplings V_L , V_R , g_L and g_R can be configured.

4.2.1 Sample Generation

The generated processes which contribute to the single top t-channel production are listed in table 4.2. The used notation follows the summing rule of WHIZARD. A process is defined by selecting one particle from each of the comma separated lists. The WHIZARD internal O’Mega matrix element generator constructs the possible leading order processes between all combinations of the specified initial and final state particles. From those combinations, only events are generated which contain a resonant produced top quark. Technically, this is performed by requiring that the last three particles in the final state are originating from a decaying top quark.

There are no contributions involving Wqq' -vertices due to the trivial CKM matrix implementation within the chosen model, where the quarks are not from the same generation. The WHIZARD generator automatically mixes each defined process with a certain fraction according to the internally calculated cross sections into one sample.

The next steps in the simulation are performed with the CMSSW framework. Subsequent tau decays are simulated by interfacing with the Tauola Monte Carlo generator

4.2 Simulated Signal Samples with WHIZARD

Table 4.2: The simulated processes with WHIZARD. l^\pm means charged leptons (e^\pm, μ^\pm, τ^\pm).

initial state		spectator		top quark decay	
b, \bar{b}	$+ u, \bar{u}, d, \bar{d}$	$\rightarrow u, \bar{u}, d, \bar{d}$	$+ b, \bar{b}$	$+ l^-, l^+$	$+ \nu, \bar{\nu}$
b, \bar{b}	$+ s, \bar{s}$	$\rightarrow c, \bar{c}$	$+ b, \bar{b}$	$+ l^-, l^+$	$+ \nu, \bar{\nu}$
b, \bar{b}	$+ c, \bar{c}$	$\rightarrow s, \bar{s}$	$+ b, \bar{b}$	$+ l^-, l^+$	$+ \nu, \bar{\nu}$
b, \bar{b}	$+ u, \bar{u}, d, \bar{d}$	$\rightarrow u, \bar{u}, d, \bar{d}$	$+ b, \bar{b}$	$+ u, \bar{u}, d, \bar{d}$	$+ u, \bar{u}, d, \bar{d}$
b, \bar{b}	$+ s, \bar{s}$	$\rightarrow c, \bar{c}$	$+ b, \bar{b}$	$+ u, \bar{u}, d, \bar{d}$	$+ u, \bar{u}, d, \bar{d}$
b, \bar{b}	$+ c, \bar{c}$	$\rightarrow s, \bar{s}$	$+ b, \bar{b}$	$+ u, \bar{u}, d, \bar{d}$	$+ u, \bar{u}, d, \bar{d}$
b, \bar{b}	$+ u, \bar{u}, d, \bar{d}$	$\rightarrow u, \bar{u}, d, \bar{d}$	$+ b, \bar{b}$	$+ s, \bar{s}$	$+ c, \bar{c}$
b, \bar{b}	$+ s, \bar{s}$	$\rightarrow c, \bar{c}$	$+ b, \bar{b}$	$+ s, \bar{s}$	$+ c, \bar{c}$
b, \bar{b}	$+ c, \bar{c}$	$\rightarrow s, \bar{s}$	$+ b, \bar{b}$	$+ s, \bar{s}$	$+ c, \bar{c}$

[71]. The hadronization simulation is performed with Pythia6. Then, the Fast Simulation package is used to simulate the detector. Fast Simulation provides a 100 - 1000 faster simulation than the Geant4-based simulation (Fullsim) by approximating the detector response [39, 11].

Approximately 2,000,000 events have been simulated for various coupling scenarios. Most extreme deviations from the SM coupling case have been used. Therefore, four samples with pure V_L , V_R , g_L and g_R couplings were generated. Thus, the anomalous coupling scenarios allow an extreme test of the analysis strategy. Additionally, six samples have been generated to include interference effects. Those contain mixes of $V_L = 1$ and one additional V_R , g_L or g_R coupling. In total, ten scenarios have been simulated including the SM coupling case. The SM scenario has been simulated in order to allow a comparison of the WHIZARD Fastsim and Powheg Fullsim simulations.

For simplicity, imaginary parts of couplings have been neglected $\Im(V_L) = \Im(V_R) = \Im(g_L) = \Im(g_R) = 0$. Such complex couplings may introduce a new CP violation.

4.2.2 Results

From the generated samples events are selected for comparison where the W boson decays into a muon and neutrino. The distributions of the angles $\cos \theta_{B,X}$ between the spin bases B and the spin analyzers X are observables for the anomalous couplings. The resulting $\frac{d\sigma}{d \cos \theta_{B,X}}$ distributions for the muon, bottom quark and neutrino as spin analyzer X in the spectator basis B are shown in figure 4.2. WHIZARD reproduces the expected linear shape from theory [5]. The SM coupling case ($V_L = 1, V_R = g_L = g_R = 0$)

is highlighted as bold black line and a subset of anomalous coupling scenarios are drawn as colored lines. The legend denotes only the couplings which are non-zero.

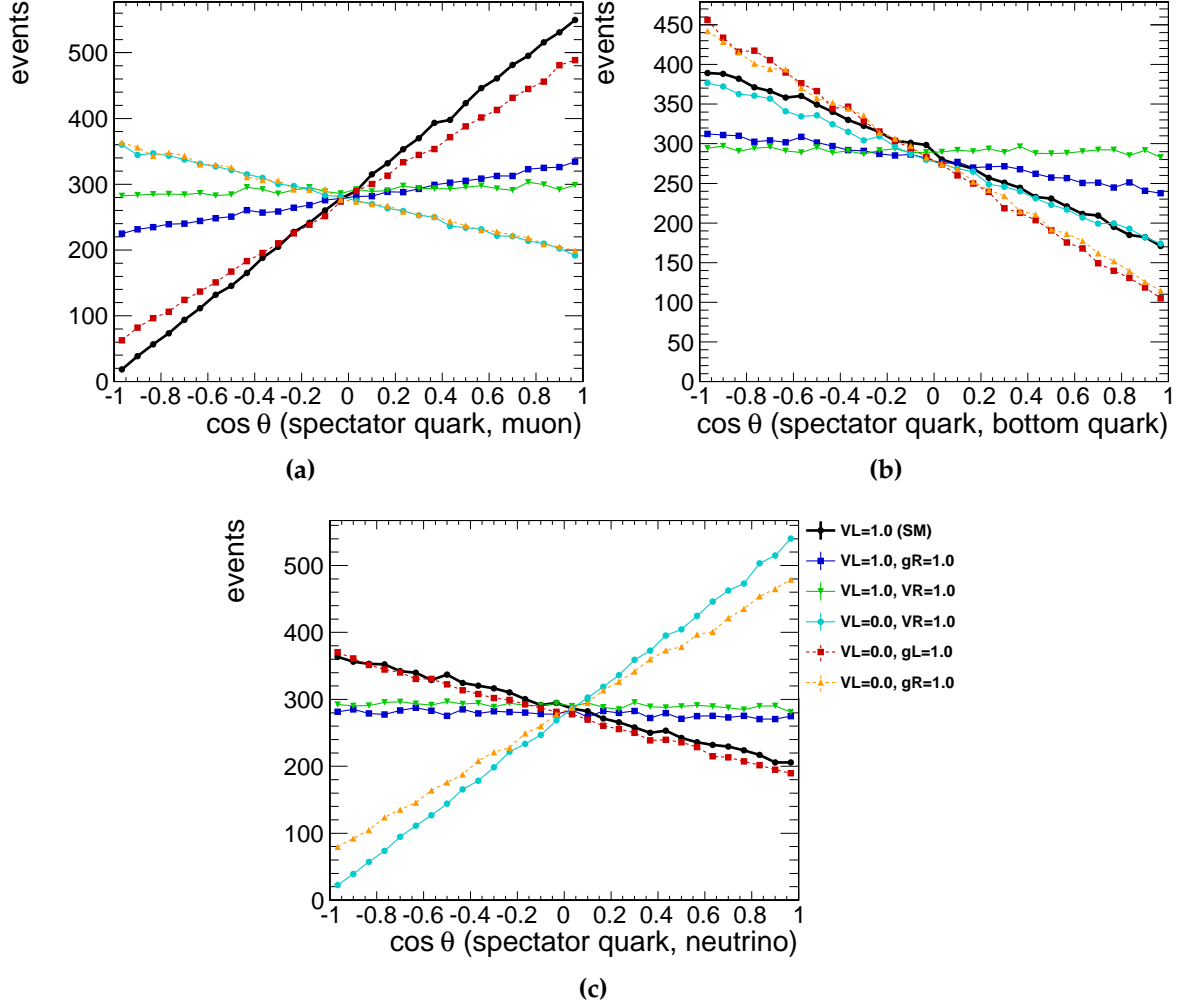


Figure 4.2: The simulated $\frac{d\sigma}{d\cos\theta_{B,X}}$ distributions for the lepton (a), bottom quark (b), and neutrino (c) as spin analyzer X in the spectator basis B for different coupling scenarios by WHIZARD.

The distributions demonstrate that the effect of anomalous couplings can have a significant impact on the differential angular distributions. In addition, some coupling scenarios yield only shape differences for one or two of the three spin analyzers. As an example, the two scenarios with the couplings $V_L = 0$, $V_R = 1$, $g_L = g_R = 0$ and $V_L = V_R = g_L = 0$, $g_R = 1$ differ for the bottom quark and the neutrino spin analyzer in shape, but not for the muon. Thus, it is crucial to measure all three distributions and their related top quark spin asymmetries to obtain an insight into possible realized anomalous couplings.

4.3 Dataset

Another distribution which is influenced by the anomalous couplings is $\frac{d\sigma}{d\cos\theta^*}$. Here, $\cos\theta^*$ is the angle between the W boson in the top quark rest frame and the muon in the W boson rest frame. $\cos\theta^*$ is shown in figure 4.3 and used to obtain the W boson helicity fractions. The W boson helicity fractions are used as a cross check for comparison with the theoretical prediction in this analysis.

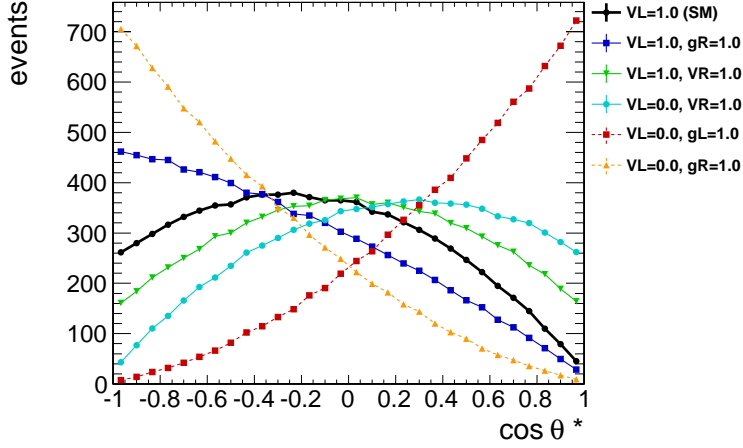


Figure 4.3: The resulting W boson helicity fractions. WHIZARD SM sample (bold black line) compared to a selection of anomalous coupling scenarios (colored lines).

Table 4.3 summarizes the top quark spin asymmetries and W boson helicity fractions as generated by WHIZARD for the ten different coupling scenarios. The W boson helicity fractions are estimated by a χ^2 fit in $\cos\theta^*$. The statistical uncertainty for the asymmetries and W boson helicity fractions is below $\lesssim 0.004$.

The W boson helicity fractions are compatible with the theoretical prediction [5]. However, the top quark spin asymmetries agree only for the Standard Model coupling case with the theory calculation [5]. Furthermore, the samples with the couplings $V_L = 1.0, V_R = 0.0, g_L = 0.0, g_R = 0.5$ and $V_L = 0.0, V_R = 0.0, g_L = 0.0, g_R = 1.0$ yield an unexpected significant higher polarization ρ in the beamline basis as in the spectator basis. This feature is very contradicting to the theory and those two samples are therefore excluded from the analysis.

During the analysis, the WHIZARD samples are only used to estimate a potential bias within the analysis procedure. Therefore, the influence on the measurement by using those samples anyway is marginal.

4.3 Dataset

Data from the first half of the 2011 proton-proton collision run at 7 TeV is analyzed. The trigger “HLT_IsoMu17” for the selection of muon events is required to be fired in the

Table 4.3: The resulting top quark spin asymmetries and W boson helicity fractions.

coupling				top quark spin asymmetries						W boson helicity fractions	
V_L	V_R	g_L	g_R	$A_l^{\text{spec.}}$	$A_l^{\text{beam.}}$	$A_b^{\text{spec.}}$	$A_b^{\text{beam.}}$	$A_{\nu}^{\text{spec.}}$	$A_{\nu}^{\text{beam.}}$	F_-	F_0
1.0	0.0	0.0	0.0	+0.480	+0.427	-0.205	-0.181	-0.148	-0.133	0.292	0.679
1.0	1.0	0.0	0.0	+0.013	+0.005	-0.003	-0.001	-0.007	+0.001	0.164	0.665
1.0	0.0	1.0	0.0	+0.431	+0.413	-0.286	-0.272	-0.160	-0.150	0.111	0.338
1.0	0.0	0.0	1.0	+0.096	+0.039	-0.071	-0.036	-0.009	+0.011	0.563	0.417
1.0	0.5	0.0	0.0	+0.255	+0.225	-0.079	-0.068	-0.128	-0.112	0.246	0.667
1.0	0.0	0.5	0.0	+0.456	+0.419	-0.239	-0.219	-0.159	-0.145	0.209	0.514
1.0	0.0	0.0	0.5	+0.077	+0.132	-0.158	-0.273	+0.100	+0.172	0.040	0.917
0.0	1.0	0.0	0.0	-0.151	-0.139	-0.191	-0.182	+0.476	+0.445	0.032	0.659
0.0	0.0	1.0	0.0	+0.398	+0.401	-0.318	-0.321	-0.163	-0.166	0.006	0.106
0.0	0.0	0.0	1.0	-0.149	-0.168	-0.297	-0.338	+0.367	+0.417	0.869	0.124

4.4 Event Selection

recorded data events. The analyzed data corresponds to an integrated luminosity of 1165.60 pb^{-1} .

4.4 Event Selection

To select single top t-channel events from the recorded data and MC samples the following lists of requirements are applied:

Muon selection Besides that the HTL trigger is fired the muon needs to fulfill the following criteria:

- a transverse momentum $p_T > 20 \text{ GeV}$,
- measured within a pseudorapidity range $|\eta| < 2.1$,
- originated less than $< 0.02 \text{ cm}$ away from the beamspot (2D impact parameter),
- a relative isolation of $\frac{\text{charged hadron iso} + \text{neutral hadron iso} + \text{photon hadron iso}}{p_T} < 0.15$ within a cone of $\Delta R = 0.4$,
- is a "Global Muon",
- has more that > 10 hits in the silicon part of the inner tracker,
- has at least 1 hit in the pixel tracker.

Also, veto for additional leptons are applied. Events are rejected if they contain one of the following:

- a "loose" "Global Muon" with $p_T > 10 \text{ GeV}$ in $|\eta| < 2.5$ and a relative isolation of < 0.2 ,
- a "loose" electron with $E_T > 15 \text{ GeV}$ in $|\eta| < 2.5$ and a relative isolation of < 0.2 .

Missing transverse energy The undetected neutrino reveals itself in large missing energy. Events are selected if the missing transverse energy in combination with the muon leads to a transverse W boson mass above $M_T^W > 40 \text{ GeV}$. The transverse W boson mass can be calculated from the transverse energy of the muon E_T^μ and the missing transverse energy E_T^{miss} by

$$M_T^W = \sqrt{2 \cdot E_T^{\text{miss}} E_T^\mu \cdot (1 - \cos \Delta\phi(\mu, E_T^{\text{miss}}))}. \quad (4.4.1)$$

$\Delta\phi(\mu, E_T^{\text{miss}}) = |\phi_\mu - \phi_{E_T^{\text{miss}}}|$ denotes the difference of the ϕ angles in the xy-plane.

Jets Two PF jets are required. Jets are reconstructed with the anti- k_T algorithm ($R = 0.5$). The light jet originates from the quark which recoils against the W boson. Therefore, single top quark t-channel events involve often at least one very forward jet.

Jets have to fulfill the following criteria:

- a transverse momentum $p_T > 30 \text{ GeV}$,
- detected in a pseudorapidity range $|\eta| < 4.5$,
- and it has to consist of more than one PF-object.

For jets within the detector barrel ($|\eta| < 2.4$), additional requirements are applied:

- the neutral and charged EM energy fractions are below 0.99,
- the neutral hadron energy fraction is below 0.99,
- the charged hadron fraction is larger 0,
- and the charged multiplicity is larger than 0.

Those quality requirements are motivated by the fact that a real jet consists out of a mixture of charged and neutral particles measured in the ECAL and HCAL.

To consider a jet as b-tagged, the discriminator of the Track Counting High Purity (TCHP) algorithm has to be larger than 3.41 [64]. This b-tagged jet has to be measured within the tracker ($|\eta| < 2.4$).

Table 4.4 lists the number of data events and the predicted event yields from the simulated samples for the integrated luminosity of 1165.60 pb^{-1} after the full event selection. Only the MC statistical uncertainties are denoted. The theoretical uncertainties are discussed in section 6.1.

The observed disagreement between the data and the expected events from simulation maybe due to an underestimated background process. This discrepancy will be further investigated during the measurement.

The simulated single top t-channel events which pass the event selection are not entirely from the direct W boson decay into a muon and neutrino. There are extra events which contain processes where the W boson decays into a tau and a neutrino. Then, the tau decays further into a muon and a second neutrino. In that decay chain the spin information of the top quark is lost due to the unknown relative directions of two escaping neutrinos. Therefore, those events are singled out and have to be considered as an additional background contribution.

After applying the event selection requirement of $M_T^W > 40 \text{ GeV}$, the remaining contribution from the simulated QCD multijet background contains only very few simulated MC events. Figure 4.4 shows the normalized distribution of the transverse W boson mass M_T^W before the selection requirement. In general, a good agreement between simulation and data is observed. The QCD multijet background contribution is therefore neglected in this analysis.

4.5 Top Quark Reconstruction

Table 4.4: Event yields of data and MC samples after event selection. MC statistical uncertainties only.

single top quark t-channel ($t \rightarrow \mu + X$)	432.13 ± 2.15
single top quark t-channel ($\bar{t} \rightarrow \mu + X$)	244.66 ± 1.68
single top quark t-channel ($t \rightarrow \tau + X$)	15.25 ± 0.41
single top quark t-channel ($\bar{t} \rightarrow \tau + X$)	8.53 ± 0.31
single top quark s-channel (t)	35.41 ± 0.56
single top quark s-channel (\bar{t})	16.67 ± 0.35
single top quark tW-channel (t)	81.57 ± 0.89
single top quark tW-channel (\bar{t})	80.49 ± 0.88
$t\bar{t}$	994.98 ± 5.85
QCD multijet (μ enriched)	67.78 ± 25.62
$W(\rightarrow l\nu) + \text{light flavor}$	196.11 ± 3.84
$W(\rightarrow l\nu) + bX$	944.72 ± 6.75
$W(\rightarrow l\nu) + cX$	711.98 ± 6.29
$Z/\gamma^*(\rightarrow l^+l^-) + \text{light flavor}$	11.74 ± 1.20
$Z/\gamma^*(\rightarrow l^+l^-) + cX$	18.46 ± 1.28
$Z/\gamma^*(\rightarrow l^+l^-) + bX$	113.52 ± 3.04
WW	19.20 ± 0.48
WZ	21.15 ± 0.27
ZZ	1.92 ± 0.05
Total MC	3948.49 ± 28.51
Data	4776.00

4.5 Top Quark Reconstruction

The reconstruction of the top quark is depicted in figure 4.5. It shows a view of an event which is used as top quark hypothesis within the analysis development environment VISPA. Before the top quark can be reconstructed, a neutrino hypothesis has to be obtained from the missing transverse energy.

The neutrino escapes the detector and is only indirectly observed through the missing

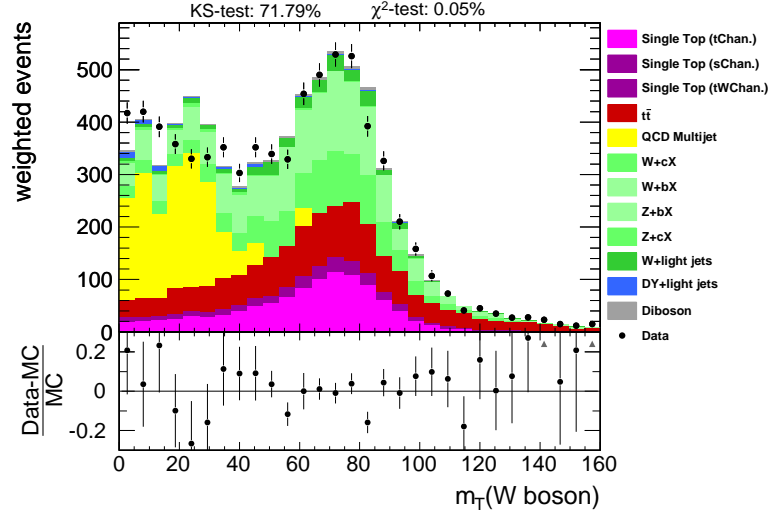


Figure 4.4: QCD background in the transverse W boson mass distribution

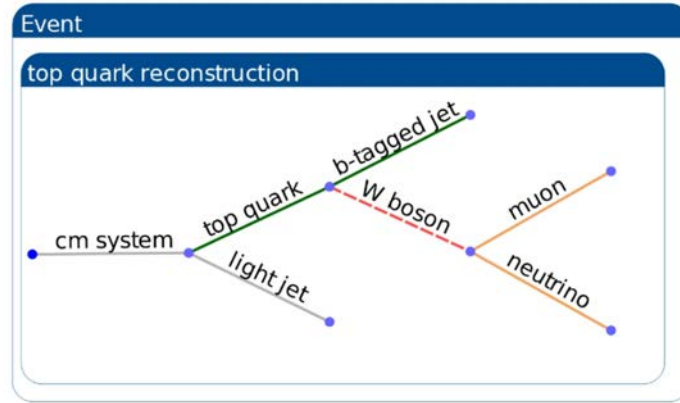


Figure 4.5: The “top quark event view” inside VISPA.

transverse energy $E_T^{\text{miss}} = p_{\nu, T}$. Its momentum $p_{\nu, z}$ along the beamline is unknown, but can be calculated. This is performed by exploiting the conservation of energy and momentum at the $W\mu\nu$ -vertex

$$m_W^2 = \begin{pmatrix} E_W \\ \vec{p}_W \end{pmatrix}^2 = \left[\begin{pmatrix} E_\mu \\ \vec{p}_\mu \end{pmatrix} + \begin{pmatrix} E_\nu \\ \vec{p}_\nu \end{pmatrix} \right]^2. \quad (4.5.1)$$

By applying a W boson mass constraint of $m_W = 80.4 \text{ GeV}$, the equation 4.5.1 can be solved with respect to $p_{\nu, z}$.

In the approximation of a massless muon and neutrino the equation 4.5.1 leads to

4.6 Validation

$$m_W^2 = \underbrace{m_\mu^2 + m_\nu^2}_{\approx 0} + 2 \cdot \begin{pmatrix} E_\mu \\ p_{\mu,x} \\ p_{\mu,y} \\ p_{\mu,z} \end{pmatrix} \cdot \begin{pmatrix} E_\nu \\ p_{\nu,T} \cdot \cos \phi_\nu \\ p_{\nu,T} \cdot \sin \phi_\nu \\ p_{\nu,z} \end{pmatrix}. \quad (4.5.2)$$

After rearranging, two solutions are given by

$$p_{\nu,z}^{1,2} = \frac{1}{E_\mu^2 - p_{\mu,z}^2} \left(a \cdot p_{\mu,z} \pm E_\mu \sqrt{a^2 - E_\mu^2 \cdot p_{\nu,T}^2 + p_{\mu,z}^2 \cdot p_{\nu,T}^2} \right) \quad (4.5.3)$$

with

$$a = \frac{m_W^2}{2} + p_{\nu,T} \cdot p_{\mu,T} \cdot \cos(\phi_\mu - \phi_\nu) + p_{\mu,z} \cdot p_{\nu,z}. \quad (4.5.4)$$

A more detailed derivation of the $p_{\nu,z}$ solution is given in Ref. [57]. For the solution, two cases can arise which has to be dealt with:

1. The $p_{\nu,z}^{1,2}$ solutions are real. Here it has been demonstrated that it is correct to chose the solution with the smaller absolute longitudinal momentum $p_{\nu,z} = \min(p_{\nu,z}^1, p_{\nu,z}^2)$ in 60% of this case [57].
2. The $p_{\nu,z}^{1,2}$ solutions are complex. This case can occur due to a mismeasurement of the missing transverse energy. Furthermore, the W boson mass constrain assumes only on-shell W bosons but the W boson can also be off-shell. This yields in 36% of all cases a larger virtual W boson mass than the constrain [69]. This case is solved by varying E_x^{miss} and E_y^{miss} independently until a real solution emerges.

After the neutrino $p_{\nu,z}$ solution is calculated, the top quark four-momentum is reconstructed by adding the four-momenta of the b-tagged jet, the muon, and the neutrino.

A second top quark hypothesis is obtained by requiring that the resulting top mass is in the vicinity of $m_t = 172 \text{ GeV}$. This exploits also the possibility that the light jet instead of the b-tagged jet is from the top quark decay. The resulting top quark is called “best top” and the used jet “best jet” as an alternative hypothesis.

Additionally, the hadronic final state (HFS) object is constructed from the momenta of the two jets.

4.6 Validation

The WHIZARD SM coupling scenario ($V_L = 1$, $V_R = g_L = g_R = 0$) is compared to the Powheg single top t-channel sample after the event selection and top quark reconstruction to gain confidence in the WHIZARD simulation and the “Fast simulation” of the

detector. This is also interesting if there is a visible effect between the next-to-leading order simulation of Powheg and the leading order simulation of WHIZARD. Figure 4.6 shows kinematic distributions in variables related to the single top quark production process. The WHIZARD distributions are normalized to the Powheg prediction.

There is a good agreement in the simulation of the transverse momentum of the leading jet and the muon. The distributions in pseudorapidity for the muon fits also well. However, a discrepancy in the prediction in the pseudorapidity distribution of the light jet is visible for $|\eta| \gtrsim 3$. This is a known behavior of the Fast simulation for jets simulated within the hadron forward (HF) calorimeter. Nevertheless, the distributions of the reconstructed transverse W boson mass and the top mass shows no obvious discrepancies.

In figure 4.7, the $\frac{d\sigma}{d\cos\theta_{B,X}}$ distributions are shown for all three spin analyzers (muon, b-tagged jet, and neutrino) in the two bases (spectator and beamline). The agreement between the Powheg and WHIZARD predictions in those distributions fit very well and show only a slight deviation for the muon as spin analyzer (figure 4.7a and 4.7b).

Through the event selection, a drop in the distributions for the muon and b-tagged jet as spin analyzer occurs for $\cos\theta_{B,X} \rightarrow 1$. This can be explained as follows.

For $\cos\theta_{B,X} = 1$, the spin analyzer X and the light jet are in the same direction in the top quark rest frame. This is often also the case if the situation is viewed in the lab rest frame. Thus, by requiring that the muon is isolated, the observed drop in 4.7a and 4.7b occurs. Furthermore, a minimum distance $\Delta R = \sqrt{\Delta\eta^2 + \Delta\phi^2}$ between the light jet and the b-tagged jet is imposed through the jet clustering which explains also the drop in 4.7c and 4.7d.

In conclusion, the simulation of the SM coupling scenario with WHIZARD reproduces the Powheg prediction. Thus, it is applicable to use the anomalous coupling samples as cross check samples.

4.6 Validation

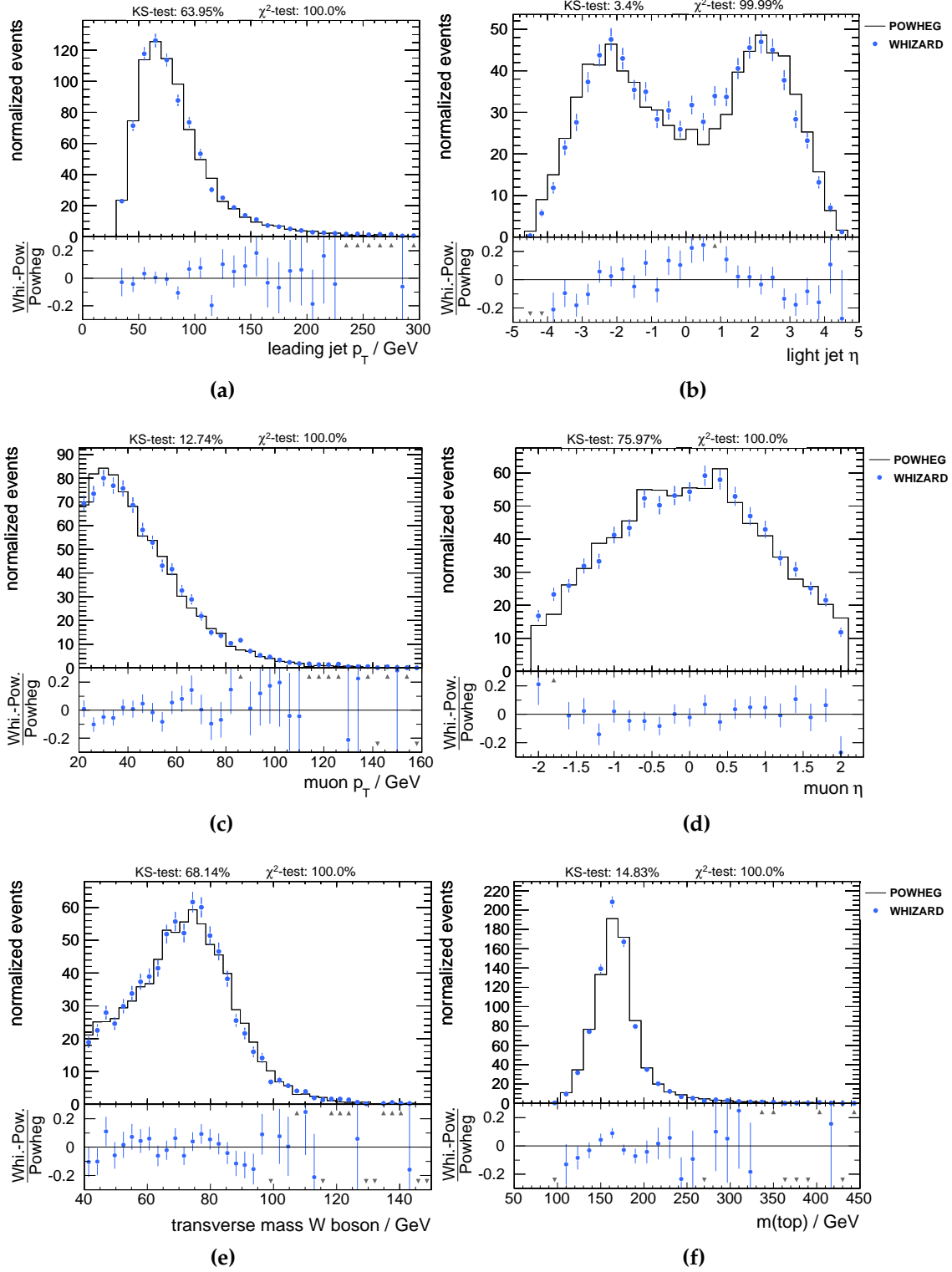


Figure 4.6: WHIZARD SM and Powheg comparison in kinematic variables. (a): The transverse momentum of the leading jet. (b): The pseudorapidity of the light jet. (c): The transverse momentum of the muon. (d): The pseudorapidity of the muon. (e): The transverse W boson mass before the neutrino solution. (f): The reconstructed top quark mass.

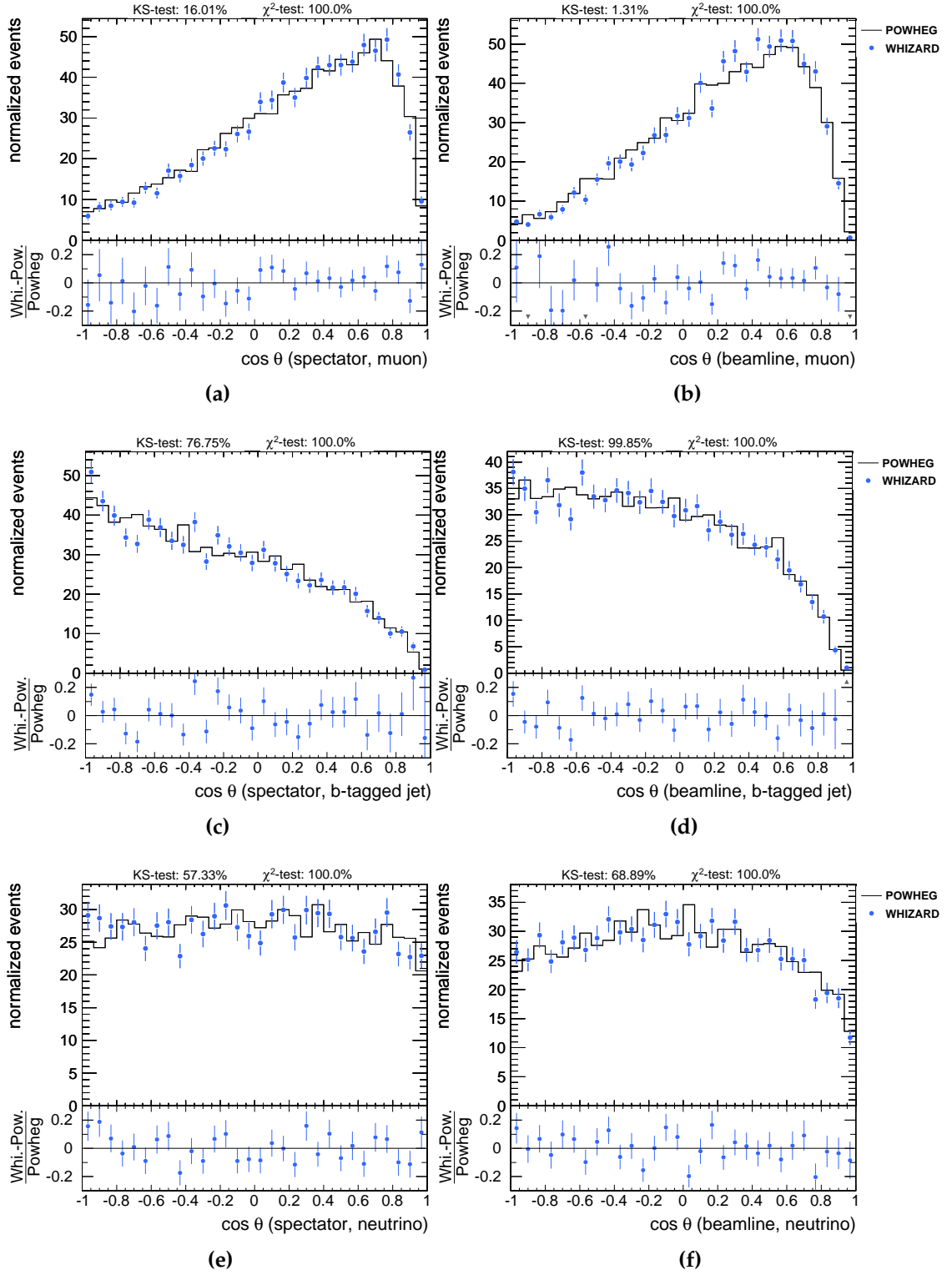


Figure 4.7: WHIZARD SM and Powheg comparison in $\cos \theta_{B,X}$ with the spectator jet or the beamline as spin basis B and the muon, b-tagged jet, or the neutrino as spin analyzer X.

Analysis Strategy

The core of this analysis is the measurement of the top quark spin asymmetries. The analysis strategy can be divided into the following two steps which are described in detail in this chapter:

- Measurement of the single top quark t-channel differential $\frac{d\sigma}{d \cos \theta_{B,X}}$ distributions. X denotes the spin analyzer (muon, b-tagged jet, or neutrino) and B denotes the spin basis (spectator or beamline). Multivariate analysis techniques are used to separate signal and background events.
- Unfolding of the distributions to correct for reconstruction and detector effects.

From the unfolded distributions the top quark spin asymmetries are calculated.

5.1 The Observables

Figure 5.1 shows the $\frac{d\sigma}{d \cos \theta_{B,X}}$ distributions after the event selection. The background processes are already normalized to their data-driven estimate as described in chapter 6.1.

There is a good agreement between data and the simulated events for the neutrino spin analyzers and the b-tagged jet spin analyzers in the spectator and beamline basis (figure 5.1e, 5.1f, 5.1c, and 5.1d). However the muon spin analyzer tends to have lower values in data than predicted from simulation (figure 5.1a, and 5.1b).

The contributions from background processes are still very high after the event selection. Boosted Decision Trees (BDTs) are trained in order to separate signal and background events. The discriminator output is then used to select a highly pure signal phase space.

Projective Likelihood Estimators (PLEs) are trained for comparison as an additional cross check of the BDT separation power.

5.2 Discrimination of Signal and Background

As an input to multivariate classification techniques, input variables have to be chosen. The choice for a certain variable which is e.g. based on the event kinematics is often made according to its discrimination power within the multivariate training phase. This is applicable if one is solely interested in the best background discrimination with a minimum set of variables.

For this analyses it is crucial to minimize a potential bias on the shape of the differential

5.2 Discrimination of Signal and Background

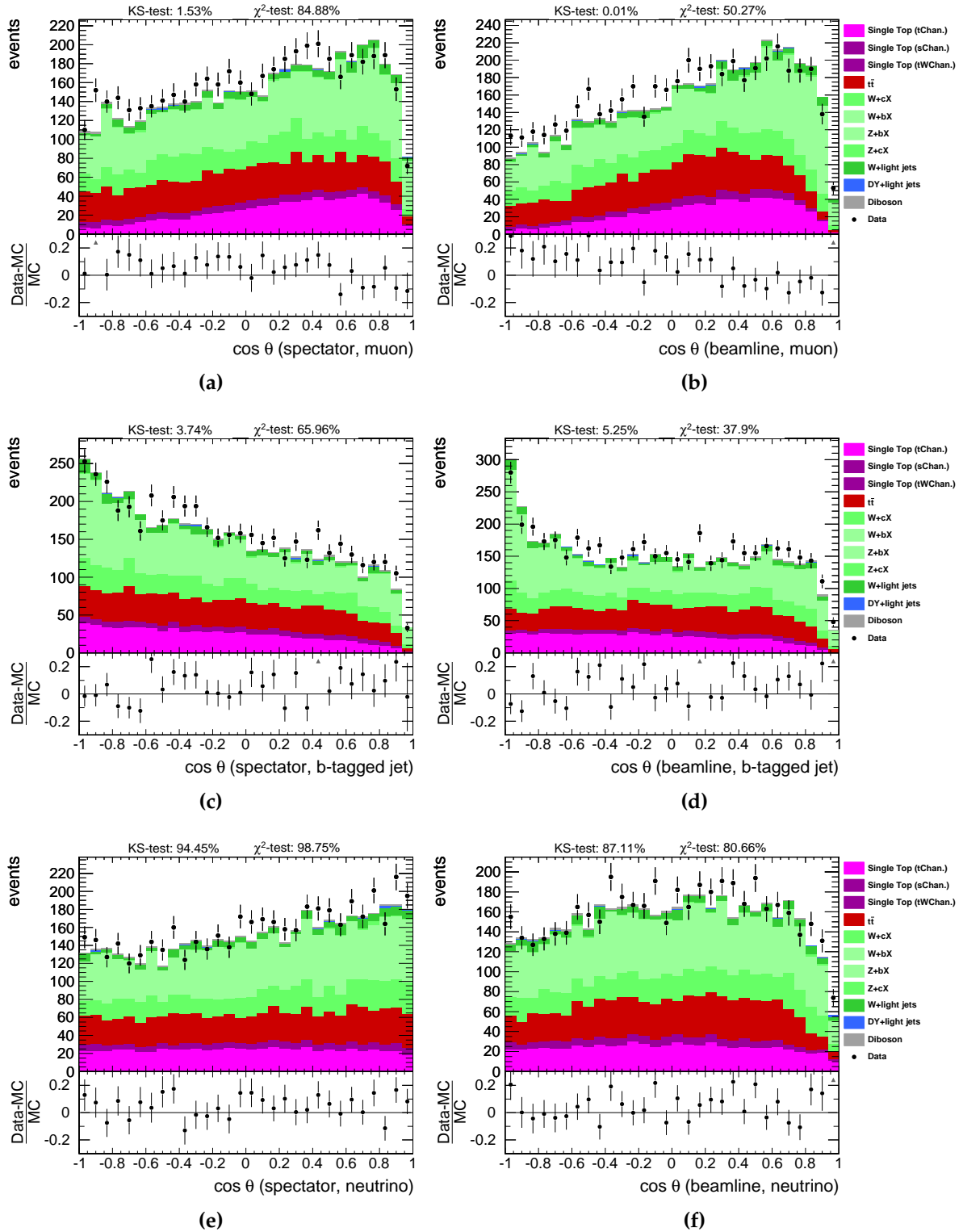


Figure 5.1: The $\frac{d\sigma}{d \cos \theta_{B,X}}$ distributions after the event selection. $\cos \theta_{B,X}$ for the muon spin analyzer in the spectator (a) and beamline (b) basis, the b-tagged jet spin analyzer in the spectator (c) and beamline (d) basis, and the neutrino spin analyzer in the spectator (e) and beamline (f) basis.

distributions after a discriminator requirement is applied. A shape bias can occur if a multivariate method becomes sensitive to the specific coupling scenario which is used for the training of the classifier. Non-correlated variables to the $\cos \theta_{B,X}$ angles are chosen as input variables. This is not a sufficient condition to obtain a bias free discriminator. The actual bias is evaluated by using the dedicated set of anomalous coupling samples.

5.2.1 Choice of Independent Variables

One way of estimating a correlation between two variables is provided by the Pearson product-moment correlation coefficient. It is calculated between the variables x and y by

$$r = \frac{\sum_i (x_i - \bar{x})(y_i - \bar{y})}{\sqrt{\sum_i (x_i - \bar{x})^2} \sqrt{\sum_i (y_i - \bar{y})^2}} \quad (5.2.1)$$

where \bar{x} and \bar{y} are the means of the distributions \vec{x} and \vec{y} . This correlation estimator is only sensitive to a linear dependence between two variables. To detect even non-linear dependencies a more sophisticated method is used.

An algorithm to test an independence hypothesis has been proposed in reference [42]. It is based on a χ^2 -test. In the following, this algorithm is elaborated.

The algorithm can be divided into two steps. Suppose the distributions of x and y are subjected to testing for independence between them.

First, the distributions of x and y are flattened. This is performed by constructing a copula in which $x \rightarrow \tilde{x}$ and $y \rightarrow \tilde{y}$ are transformed so that the distributions are only within the interval $\tilde{x}, \tilde{y} \in [0; 1]$. For a finite amount N of (x, y) pairs this can be performed by sorting $\vec{x} = (x_1, \dots, x_N)$ and $\vec{y} = (y_1, \dots, y_N)$ independently. Each value is then replaced according to its position after the sorting

$$x_i^{\text{sorted}} \rightarrow \tilde{x}_i \equiv \frac{i}{N}, \quad y_i^{\text{sorted}} \rightarrow \tilde{y}_i \equiv \frac{i}{N}. \quad (5.2.2)$$

Second, from the flattened distributions an $n \times n$ histogram h with equidistant binning is generated. If the distributions of x and y are independent, the histogram content is expected to be compatible with a two-dimensional uniform distribution. To quantify the independence hypothesis a χ^2 -test is performed by calculating

$$\chi^2 = \sum_i \sum_j \frac{(h_{ij} - e)^2}{\sigma_e^2} \quad (5.2.3)$$

with the expectation value and its uncertainty for the flat hypothesis

5.2 Discrimination of Signal and Background

$$e = \frac{N}{n^2}, \quad \sigma_e = \sqrt{\frac{N}{n^2}}. \quad (5.2.4)$$

The probability of this hypothesis follows a χ^2 -distribution with $n^2 - (2n - 1)$ degrees of freedom. The additional $2n - 1$ degrees of freedom are not present due to the copula transformation in the first step.

The algorithm is fed with over 700 variables. This includes the transverse momentum p_T , the polar angle ϕ , the pseudorapidity η and energy E of each reconstructed object. Additionally, more variables are calculated by choosing two particles and calculating their Δp_T , $\Delta\eta$, $\Delta\phi$, $\Delta R = \sqrt{\Delta\eta^2 + \Delta\phi^2}$, included angle, invariant mass, and total transverse momentum

$$P_T^{ij} = \sqrt{(p_x^i + p_x^j)^2 + (p_y^i + p_y^j)^2}. \quad (5.2.5)$$

The search for independent variables to $\cos\theta_{B,\chi}$ is performed with the Powheg sample with approximately 55000 events. Each bin in the histogram h is filled with a statistically sufficient amount of simulated events of approximately 100. For the Powheg sample, this leads to $\frac{55000}{100} \approx 23^2$ bins in h and 484 degrees of freedom.

Confidence is gained in the algorithm as it first suggests the ϕ angles of all particles to be the most independent variables. Those variables are expected to be most independent to $\cos\theta_{B,\chi}$ due to the detector geometry. As these angles do not add any discrimination power between signal and background processes, they are omitted.

The complete ranking is listed in the appendix. The ranking is obtained by testing each variable for independence against the six $\cos\theta_{B,\chi}$ angles and summing up the resulting χ^2 values. This analysis uses only the first 100 variables. Figure 5.2 shows the first and the 100th variable in the histogram h against the $\cos\theta_{\text{spec., muon}}$ angle. For the first variable, no obvious correlation is visible. The 100th variable presents a slight correlation because the regions around the points (1.0, 0.0) and (0.0, 1.0) contain less events.

5.2.2 MVA Training

Twenty different discriminators for each BDT and PLE method are trained with certain sets of input variables. The input variables are taken from the ranking in increasing sets of five variables and up to 100 variables in total (5, 10, 15, ... 100). Later in the analysis a discriminator with a certain set is chosen. If a discriminator with a set of fewer variables is used it may be independent from the observables but has less discrimination power. Otherwise a discriminator trained with a set of many variables provides a high background suppression but can introduce a potential bias through the possibly higher correlation with $\cos\theta_{B,\chi}$.

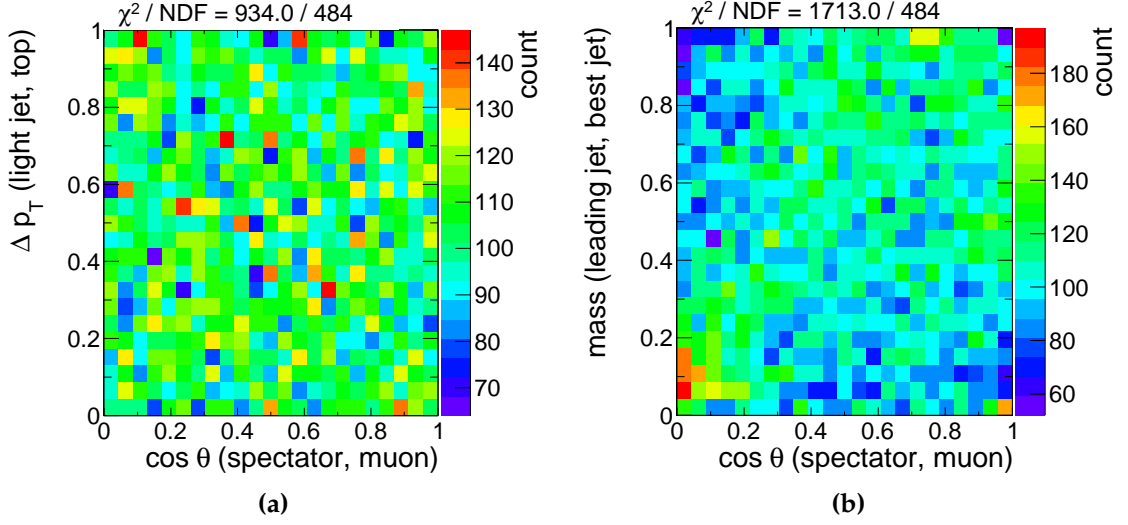


Figure 5.2: Correlation of the first (a) and 100th (b) variable to $\cos \theta_{\text{spec., muon}}$.

Figure 5.3 shows some of the most uncorrelated input variables. In figure 5.3a, the transverse momentum of the W boson plus the hadronic final state (HFS) is shown. Figure 5.3b shows the transverse momentum of the “best” top quark hypothesis. The $\Delta\phi$ and Δp_T between the top quark and the light jet is shown in figure 5.3c and 5.3d.

Those variables are well modeled in the simulation. The distributions agree with the expectation from data within the statistical uncertainties and show no significant deviations in shape.

5.2.3 Discrimination Power

The resulting 40 multivariate classifiers after the training can be characterized by their discrimination power. Figure 5.4 shows the discriminator outputs for the BDTs and PLEs trained with sets of 20, 45 and 100 input variables. The discriminator outputs have a good agreement with the data and present no discrepancies in shape.

The discrimination power can be quantified by the area under the “Receiver Operating Characteristic” (ROC) curve [15]. In figure 5.5, a subset of the ROC curves are shown for the BDT and PLE method. These curves are obtained by using certain discriminator working points and calculating the amount of remaining signal event (efficiency) and background events (purity). The ROC curve shapes for some PLEs possess a TMVA internal artifact at small or large signal efficiencies which should be ignored here.

With up to 45 variables, the separation power seems to saturate. The additional gain when using up to 100 variables is only about 4%.

5.3 Unfolding

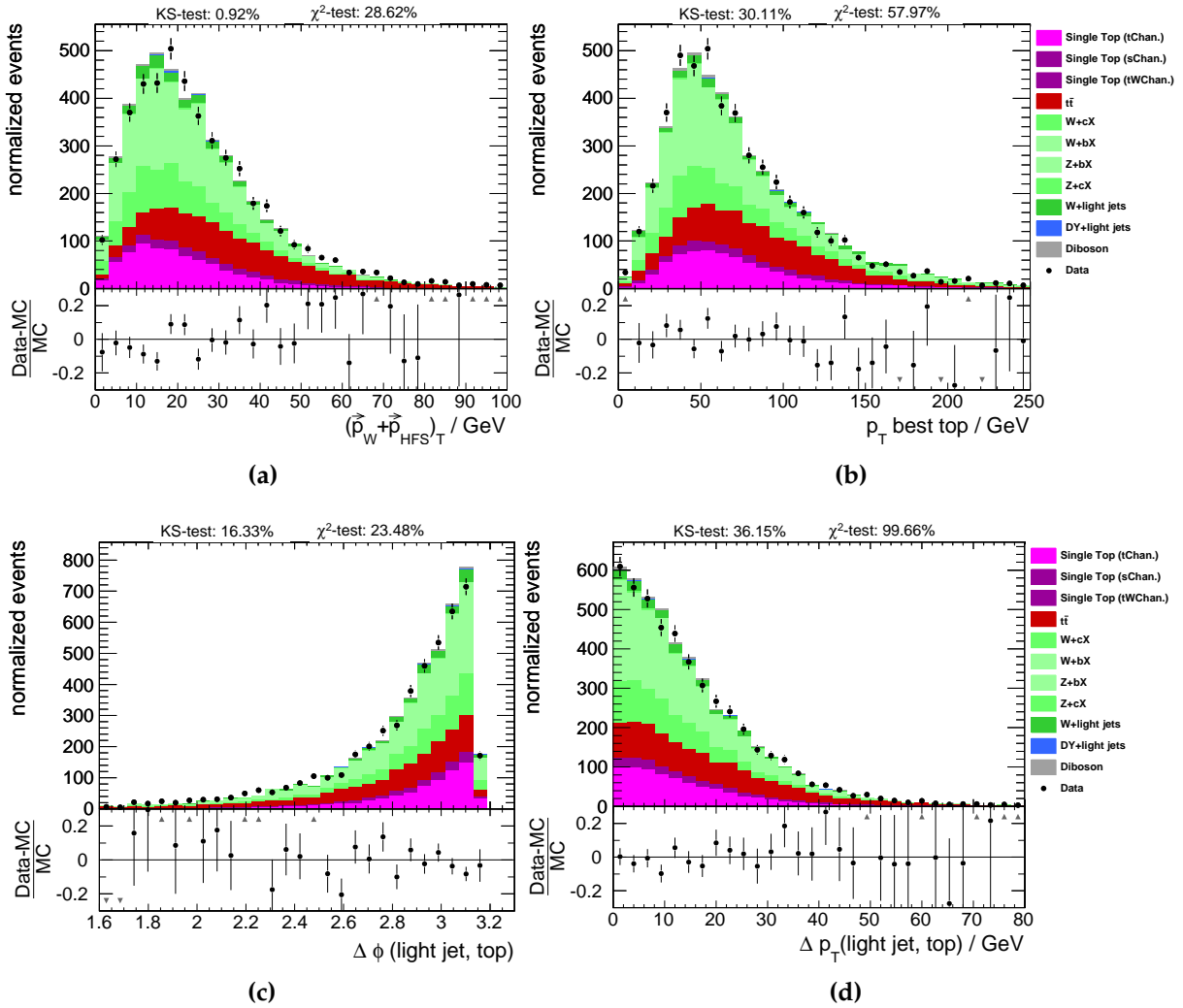


Figure 5.3: Some of the input variables used for the training of the multivariate discriminators. (a): The total transverse momentum of the W boson and the hadronic final state (HFS). (b): The transverse momentum of the “best” top quark. (c): The $\Delta\phi$ between the lightjet and the top quark. (d): The Δp_{T} between the lightjet and the top quark.

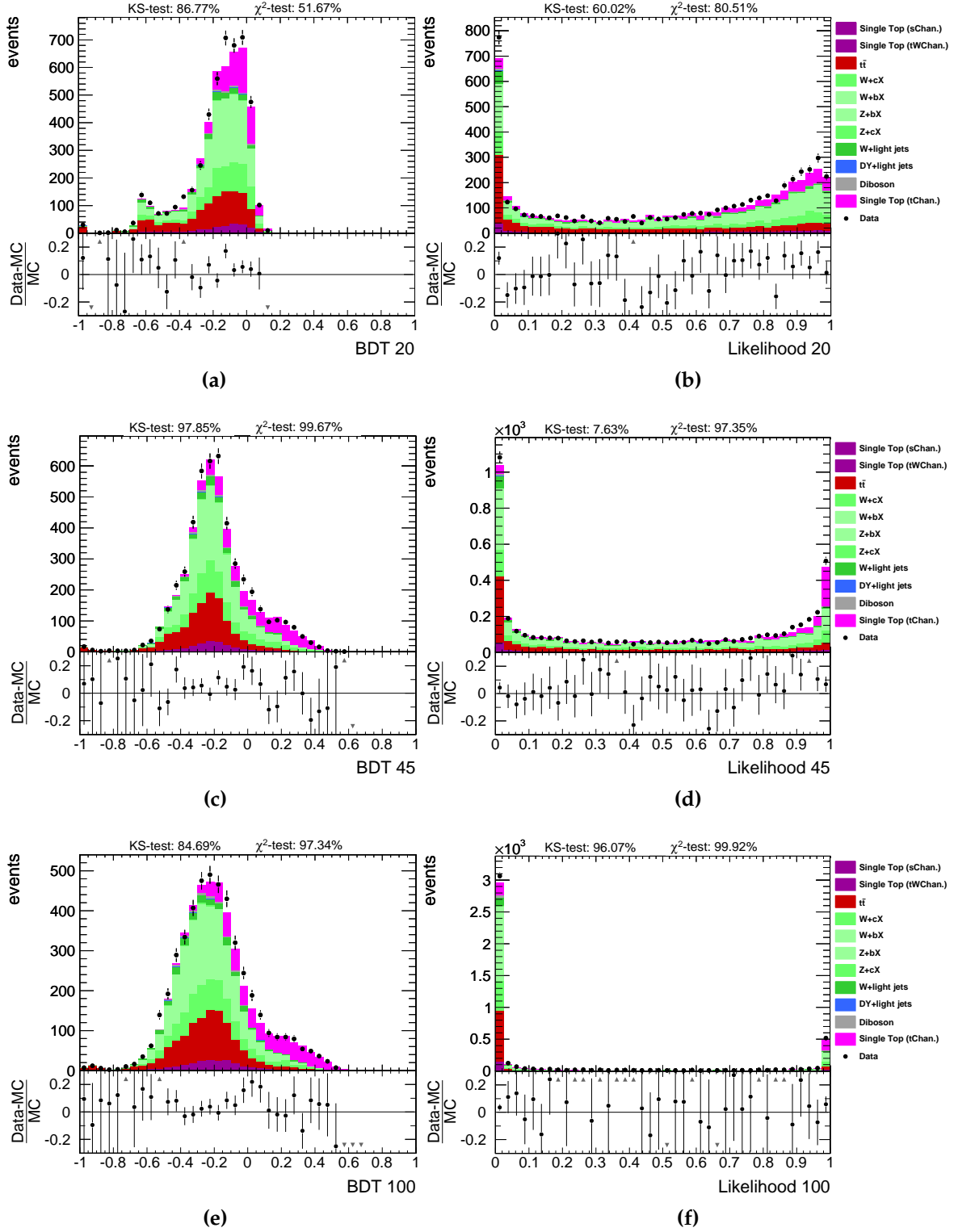


Figure 5.4: Discriminator outputs for some trained BDTs and PLEs. The discriminator outputs for the BDT by using 20 (a), 45 (c), and 100 (e) input variables and for the PLE by using 20 (b), 45 (d), and 100 (f) input variables.

5.3 Unfolding

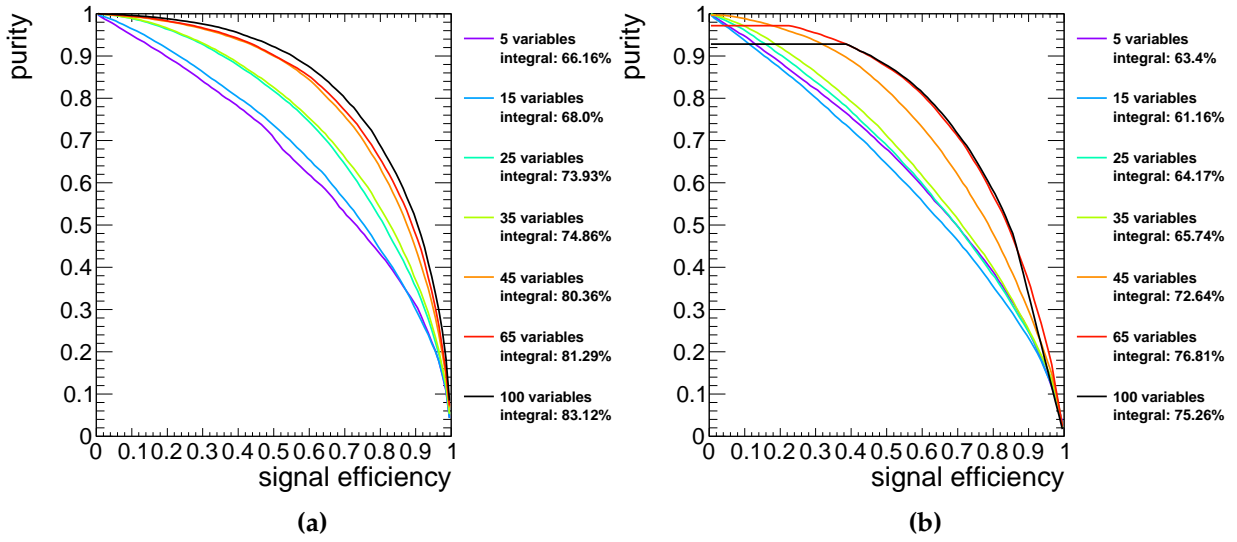


Figure 5.5: Exemplary discrimination power of the BDT and PLE methods. (a): BDT, (b): PLE.

5.3 Unfolding

A signal-enriched phase space is obtained by using a multivariate discriminator. Smearing effects, finite resolution, the acceptance of the detector and the event selection change the differential $\frac{d\sigma}{d\cos\theta_{B,X}}$ -shape. Thus, the calculation of the top quark spin asymmetries from the $\frac{d\sigma}{d\cos\theta_{B,X}}$ -distributions can not yet be compared to the theory prediction. Unfolding is a method to correct for these effects and to allow a comparison with the theoretical prediction.

5.3.1 Introduction

Suppose a true distribution $f(x)$ leads to a measured distribution $g(y)$ due to smearing, finite resolution, and acceptance effects. This can be modeled by

$$g(y) = \int f(x)A(y, x)dx \quad (5.3.1)$$

which is called a Fredholm integral equation of the first kind [14]. The function $A(y, x)$ encodes the behavior of the detector for a variable transformation $x \rightarrow y$. This transformation may even include non-linear detector responses. One is then interested in solving this equation to obtain the true distribution $f(x)$ from the measured one $g(y)$.

By discretizing the distributions within histograms, equation 5.3.1 can be written as

$$\vec{y} = A \cdot \vec{x}, \quad (5.3.2)$$

where \vec{y} denotes the measured binned distribution and \vec{x} denotes the true binned distributions. The matrix A is called “response matrix” and encodes the effects of the detector. An element a_{ij} of the response matrix is proportional to the probability that a true value in bin j is measured in bin i . The response matrix can be constructed by using a simulated event sample in which both distributions \vec{x} and \vec{y} are accessible. Therefore, the unfolding relies on the correctness of the detector simulation.

Equation 5.3.2 can simply be solved by

$$\vec{x} = A^{-1}\vec{y}. \quad (5.3.3)$$

However, this solution can be very unstable because unfolding is actual an ill-posed problem [14]. An example is shown in figure 5.6. Here, using the true distribution 5.6a and the measured distribution 5.6b (solid line), a response matrix is generated. The dashed distribution is then subjected to unfolding by inversion of the response matrix. The result is shown in figure 5.6c. Large oscillations can appear if one tries to unfold other distributions with an inverted response matrix. Only the measured distribution which is used to construct the matrix does not inherit these oscillations. The oscillations

5.3 Unfolding

can already arise if a distribution from a statistical fluctuation of the used measured distribution is unfolded. The origin of these oscillations is described in the following.

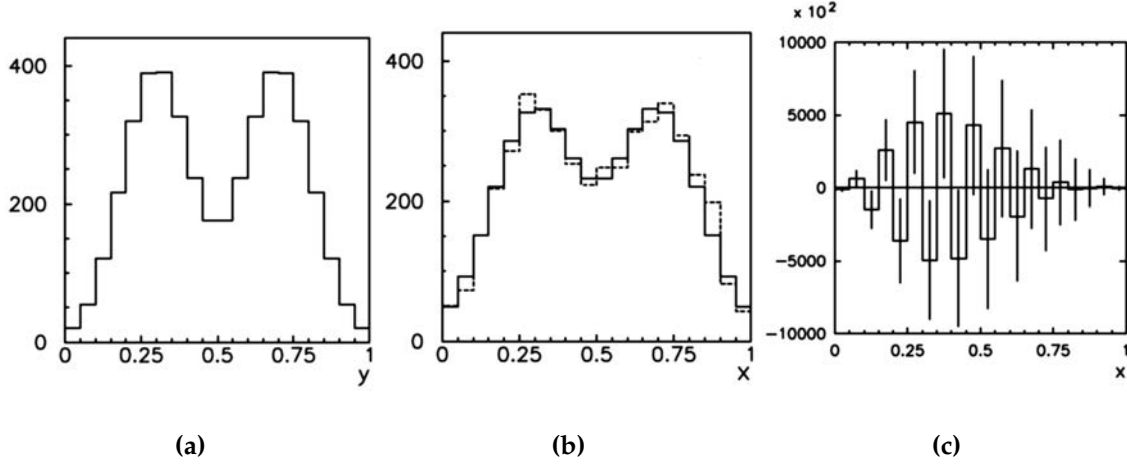


Figure 5.6: The ill-posed unfolding problem. (a): The true distribution. (b): The measured distribution for constructing the response matrix in solid and a second dashed distribution subjected to unfolding. (c): The result from the unfolding of the dashed distribution by inversion of the response matrix. Figures are taken from Ref. [38].

The singular value decomposition (SVD) helps to understand the problem [48]. SVD can be used to decompose even non-quadratic matrices A into the form

$$A = U \cdot D \cdot V \quad (5.3.4)$$

with the diagonal matrix D . The diagonal elements D_{ii} are called singular values. For the unfolding problem, they are per convention normalized as $D_{11} = 1$ and sorted as $D_{ii} > D_{i+1,i+1} > 0$. As a simple example, the response matrix

$$A = \frac{1}{2} \cdot \begin{pmatrix} 1 + \epsilon & 1 - \epsilon \\ 1 - \epsilon & 1 + \epsilon \end{pmatrix}, \quad \epsilon \in [0; 1] \quad (5.3.5)$$

of a fictitious detector with the parameter ϵ shall be analyzed. If ϵ goes to 1 the detector is able to measure a variable in both bins ideally. For $\epsilon \rightarrow 0$, both bins are smeared until they are indistinguishable by the detector.

The SVD applied to A leads to the solution

$$\vec{x} = \underbrace{(U \cdot D \cdot V)^{-1}}_{A^{-1}} \cdot \vec{y} \quad (5.3.6)$$

$$= \underbrace{\frac{1}{\sqrt{2}} \begin{pmatrix} 1 & 1 \\ 1 & -1 \end{pmatrix}}_{=V^{-1}} \cdot \underbrace{\begin{pmatrix} 1 & 0 \\ 0 & \frac{1}{\epsilon} \end{pmatrix}}_{=D^{-1}} \cdot \underbrace{\frac{1}{\sqrt{2}} \begin{pmatrix} 1 & 1 \\ 1 & -1 \end{pmatrix}}_{=U^{-1}} \cdot \begin{pmatrix} y_1 \\ y_2 \end{pmatrix} \quad (5.3.7)$$

$$= \underbrace{\frac{1}{D_{11}^{-1}}}_{D_{11}^{-1}} \cdot \frac{1}{2} \begin{pmatrix} 1 \\ 1 \end{pmatrix} \cdot (y_1 + y_2) + \underbrace{\frac{1}{\epsilon}}_{D_{22}^{-1}} \cdot \frac{1}{2} \underbrace{\begin{pmatrix} 1 \\ -1 \end{pmatrix}}_{\text{anti correlation}} \cdot (y_1 - y_2) \quad (5.3.8)$$

for the unfolding problem. The last term in equation 5.3.8 induces a negative correlation between x_1 and x_2 . If the singular value D_{22} goes to zero, this term leads to oscillations. The oscillation term dominates the first term in equation 5.3.8 through the inequation $\frac{1}{D_{11}} < \frac{1}{D_{22}}$.

In conclusion, this means that differences between two bins get unphysically amplified through a simple inversion if the response matrix contains very small singular values. In order to avoid unphysically large oscillations the unfolding procedure is regularized.

5.3.2 Regularization

A simple regularization method is performed by a singular value decomposition of the response matrix and dropping a certain amount of SVDs during the matrix inversion. This method is often called “SVD Unfolding”. The regularization can be referred to as a hard cut-off which leads to

$$x_i \rightarrow \tilde{x}_i = \sum_k^n \tilde{A}_{ik}^{-1} \cdot x_k \quad (5.3.9)$$

$$= \sum_k^n \left(\sum_j^\tau V_{ij}^{-1} \frac{1}{D_{jj}} U_{jk}^{-1} \right) \cdot x_k, \quad (5.3.10)$$

where the parameter $\tau < n$ denotes the index of the smallest considered singular value $D_{\tau\tau}$. The regularized solution \tilde{x}_i inherits a bias. The choice of the parameter τ defines a priori the maximal curvature of the unfolded distribution. Therefore, regularized unfolding can only be applied if a sufficiently “smooth” unfolded distribution is expected a priori, e.g. from theory.

5.3 Unfolding

However, this analysis uses a more sophisticated regularization method [66]. The solution \vec{x} of equation 5.3.3 can be rewritten as the minimization of the function

$$\chi^2 = (\vec{y} - A\vec{x})^T \cdot V_y^{-1} \cdot (\vec{y} - A\vec{x}) + \Re(\vec{x}, \vec{y}), \quad (5.3.11)$$

where V_y denotes the covariance matrix of \vec{y} . If the measured distribution \vec{y} does not contain correlated entries, the covariance matrix can be expressed as $V_{y,jj} = \sqrt{y_j}$. This assumes Poisson uncertainties. The optional term

$$\Re(\vec{x}, \vec{y}) = \tau^2 \vec{x} \cdot L^T L \cdot \vec{x} + \left(\sum y_i - \epsilon^T \vec{x} \right) \quad (5.3.12)$$

is added to suppress large fluctuations. The matrix L approximates numerically the second derivatives from \vec{x} . It utilizes the general formula

$$\frac{d^2 f(x)}{dx^2} \approx \frac{x_{i+1} - 2 \cdot x_i + x_{i-1}}{h^2} \quad (5.3.13)$$

for the second derivative of a discretizing generic function $f(x)$ with the step width h [63]. Additionally, the second term in equation 5.3.12 invokes a constrain on the total number of events in the unfolded distribution by using the diagonal efficiency matrix ϵ . Thus, by minimizing equation 5.3.11 the additional term \Re suppresses solutions \vec{x} with large curvatures and corrects simultaneously for acceptance effects. Oscillating solutions have high curvatures and are therefore rejected.

The regularization parameter τ controls the influence of the second derivatives in the minimization and has to be chosen carefully. If it is chosen too small, unphysical oscillations are not sufficiently suppressed. If τ is chosen too large, the solution is biased towards a solution with the smallest curvature. This regularization method is a special case of the Tikhonov-Phillips regularization method.

In this analysis, the optimal value of the parameter τ is estimated by evaluating the correlations in the unfolded solution. The procedure is demonstrated for a similar detector given in equation 5.3.5. Here, the detector is extended to measure in four different bins. The resulting correlations in the unfolded distribution are calculated as follows:

The covariance matrix V_x of the unfolded distribution is obtained by propagation of uncertainty

$$V_x = J \cdot V_y \cdot J^T = \tilde{A}^{-1} \cdot V_y \cdot \left(\tilde{A}^{-1} \right)^T, \quad (5.3.14)$$

where the Jacobi matrix J is equivalent to the regularized inverted response matrix \tilde{A}^{-1} . Then, the correlation between two bins i and j is given by

$$\rho_{ij} = \frac{\text{cov}_{ij}}{\sqrt{\text{var}_i \cdot \text{var}_j}} = \frac{V_{x,ij}}{\sqrt{V_{x,ii} \cdot V_{x,jj}}}. \quad (5.3.15)$$

In this particular analysis, the correlation coefficients are averaged as

$$''\langle \rho_{i,i+j} \rangle'' \equiv \frac{1}{n-j-1} \cdot \sum_i^{n-j-1} \rho_{i,i+j}.$$

Negative correlations between directly adjacent bins lead to $\langle \rho_{i,i+1} \rangle < 0$. This is an indicator for the previously observed unphysical oscillations. Figure 5.7 shows the averaged correlation for a simple matrix inversion ($\tau = 0$) against the detector parameter ϵ .

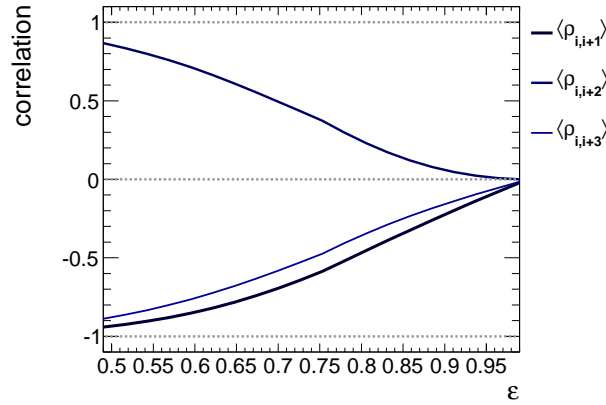


Figure 5.7: Correlations in an unregularized unfolded distribution.

A perfect detector ($\epsilon = 1$) does not have any artificial correlations. For $\epsilon < 1$, the unfolded distribution is dominated by negative correlations between adjacent bins.

The situation changes if the regularization proposed in equation 5.3.12 is turned on ($\tau > 0$). Figure 5.8a shows the resulting correlations for $\epsilon = 0.95$ against the parameter τ . In the limit case $\tau \rightarrow \infty$ the unfolded distribution is artificially influenced by large positive correlations. Thus by using the described regularization method the unfolded distribution can be artificially biased in this limit case. On the other hand the occurring negative correlations are small and an unregularized unfolding might even apply.

Figure 5.8b shows the variation in the correlations against the parameter τ for $\epsilon = 0.7$. The parameter τ can be optimized such that minimal correlations are present in the unfolded distribution.

This fact motivates the optimization for a certain τ during the analysis. The optimization resembles a tradeoff between negative and positive correlations in the unfolded distribution. The shown correlation minima (green and red curves) in figure 5.8 are estimated from the global correlation coefficients

5.3 Unfolding

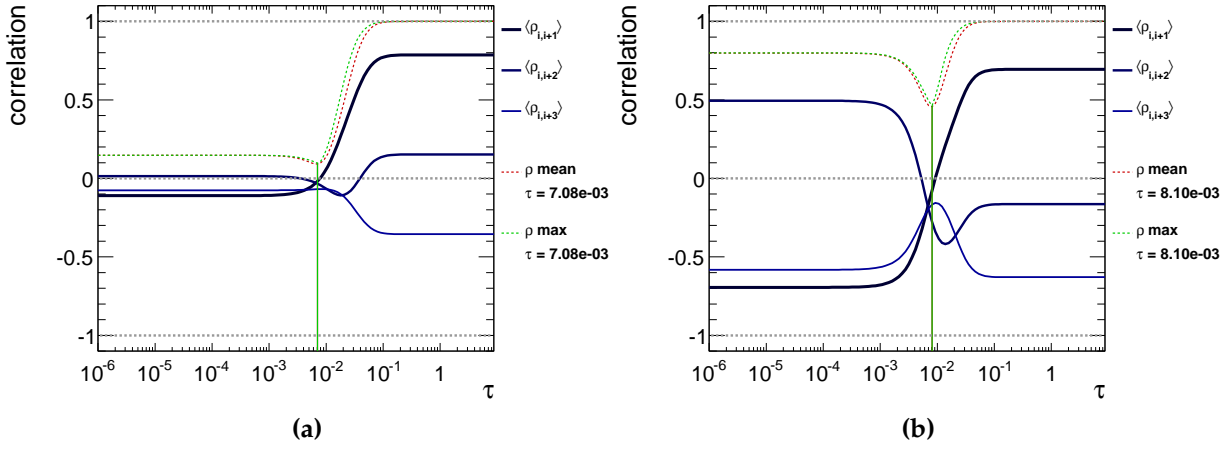


Figure 5.8: Regularized correlations for an exemplary detector. (a): $\epsilon = 0.7$, (b): $\epsilon = 0.95$.

$$\rho_i = \sqrt{1 - V_{x,ii} \cdot (V_x^{-1})_{ii}}$$

with

$$\rho_{\text{mean}} = \frac{1}{n} \cdot \sum_i \rho_i, \quad \rho_{\text{max}} = \max[\rho_1; \dots; \rho_n].$$

From those, the regularization parameter is then chosen as $\tau = \frac{\tau(\rho_{\text{mean}}) + \tau(\rho_{\text{max}})}{2}$.

This estimation of the regularization parameter is only dependent on the response matrix. It is derived without knowledge about the measured distribution which is unfolded.

Figure 5.9 shows an exemplary result from the correlation analysis of the response matrix for the angle $\cos \theta_{\text{spec., muon.}}$. The correlations between the bins in the unfolded distribution can be very complex. No optimal choice for the regularization parameter τ exists so that all correlations would vanish. However, the estimate for τ from the global correlation coefficients provides a good tradeoff.

5.3.3 Construction of the Response Matrix

The response matrix is carefully constructed using the simulation. This involves the correct categorization of events from the inclusive simulated sample. In figure 5.10, the response matrix construction procedure is shown.

From the inclusive events, those are singled out which pass the event selection on the reconstructed objects. If the selected events are single top t-channel events with a W boson decaying into a muon, they contain a muon on generation level and can be

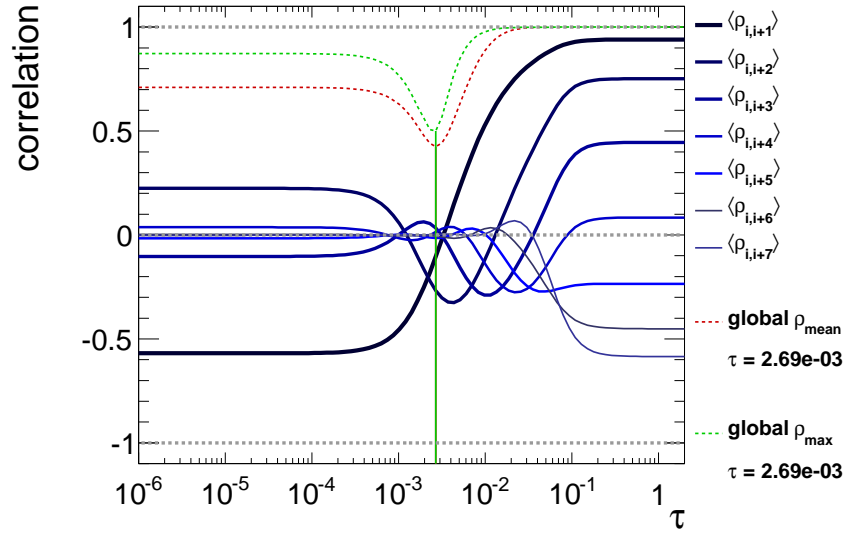


Figure 5.9: Exemplary optimization for the $\cos \theta_{\text{spec., muon}}$ angle.

used to construct the response matrix. However, events that do not contain a muon on generator level can pass the event selection as well. In those events, reconstructed muons stems from subsequent tau decays. Those events are called “fake” events and are treated as an additional background process.

All events that fail the event selection but contain a muon on generator level are used also as input to the unfolding method. From those events, the reconstruction efficiencies are calculated.

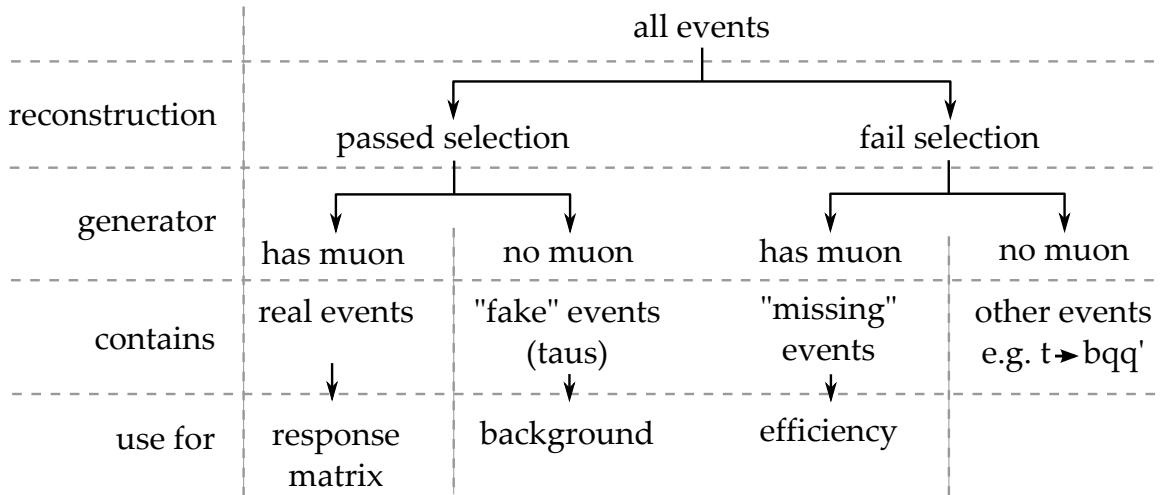
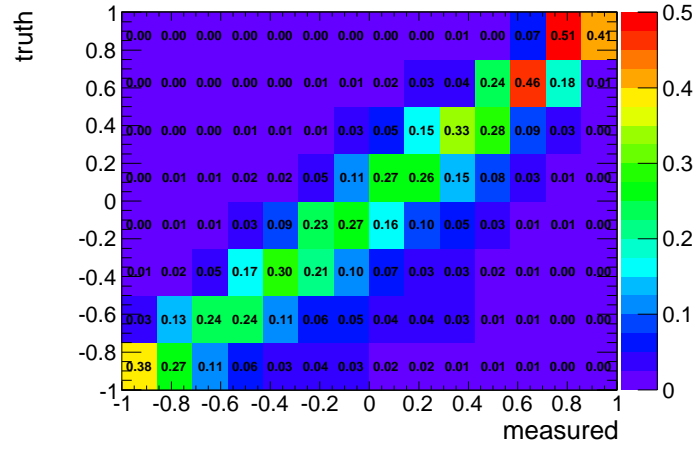


Figure 5.10: Construction of the response matrix.

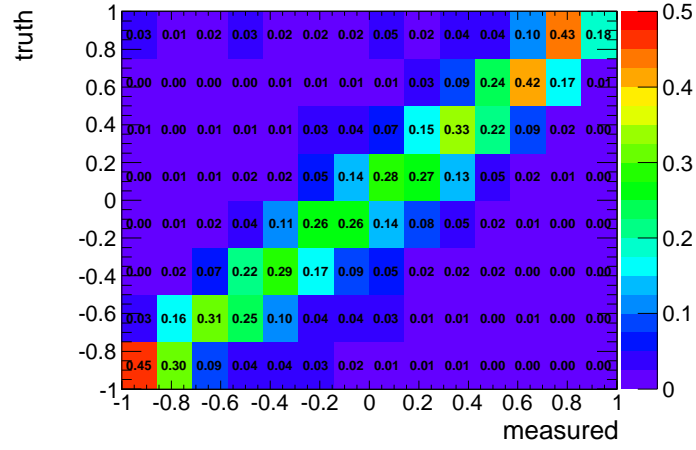
Figure 5.11 shows the resulting response matrices for the $\cos_{B,X}$ observables in the spectator basis. The response matrices are normalized to the transition probability

5.3 Unfolding

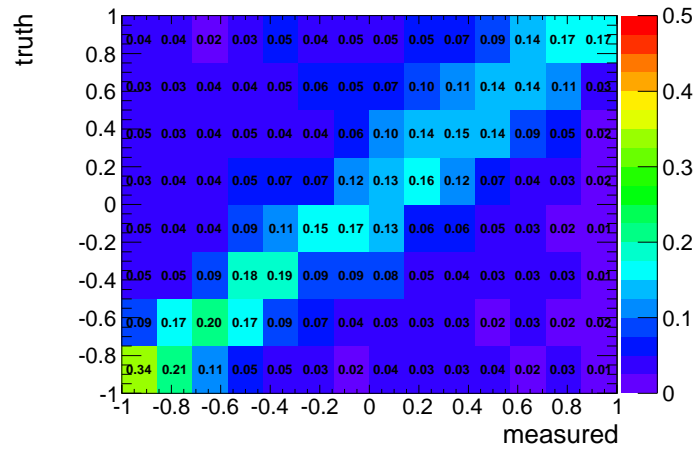
$P(\text{true} \rightarrow \text{measured})$. To stabilize the χ^2 minimization in the unfolding procedure, fourteen bins are chosen for the measured distribution and eight for the true distribution. The resolution in $\cos_{B,X}$ is optimal for X as the muon spin analyzer. For the b-tagged jet, the resolution is slightly more worse. Thus, the response matrix is more smeared. The response matrix of the neutrino is far more smeared, because the neutrino is measured indirectly via the missing transverse energy.



(a)



(b)



(c)

Figure 5.11: The response matrices for the muon (a), the b-tagged jet (b), and the neutrino (c) in the spectator basis. The color code denotes the transition probability.

Measurement Technique and Results

Before the top quark spin asymmetries from the $\frac{d\sigma}{d\cos\theta_{B,X}}$ distributions are measured from data, the influence of systematic uncertainties is investigated. The systematic uncertainties are divided into theoretical uncertainties and uncertainties which arise due to the resolution of the CMS detector and its reconstruction accuracy.

After that, the measurement procedure is described. The measurement procedure is optimized for the top quark spin asymmetry measurement with the smallest uncertainty.

Finally, the results for the top quark spin asymmetries are presented. In an additional step, the asymmetries are used with additional information from cross section measurements and W boson helicity fractions measurement to obtain limits on the anomalous top quark couplings.

6.1 Systematic Uncertainties

6.1.1 Sources

The considered source of systematic uncertainties are described in the following.

Jet energy scale The energy measurement of particles with the CMS detector is mainly performed with the calorimeters. It involves the translation of the calorimeter readouts into the actual deposited energy by a particle. The energy of a jet is then constructed by a jet algorithm. The jet construction intrinsically utilizes the readout-energy translation and depends therefore on its scale and accuracy. Furthermore, the translation depends on the measured pseudorapidity η of a jet through the geometry of the calorimeter and on the transverse momentum p_T of a jet through the resolution of the calorimeter. The jet energy scale (JES) combines those effects into correction factors [29].

The JES and its uncertainty is included into the analysis by varying the four-momenta of all simulated jets. After that, the missing transverse energy is recalculated. The missing transverse energy depends on the vector sum of all reconstructed particle momenta and receives therefore also an uncertainty from this source.

Jet energy resolution This systematic uncertainty accounts for smearing effects in the measurement of the jet energy and momentum by the detector. It is included into the analysis by varying the reconstructed energy and momentum of a jet against its

6.1 Systematic Uncertainties

generated energy and momentum [24].

The variations in resolution $\text{res}(\eta)$ depend on the pseudorapidity of the jet. Scale factors $\text{SF}(\eta, p_T)$ are applied by

$$p_{\text{jet}}^{\text{reco}} = p_{\text{jet}}^{\text{reco}} \cdot \underbrace{\left(1 + \frac{(p_{\text{jet},T}^{\text{reco}} - p_{\text{jet},T}^{\text{gen}}) \cdot \text{res}(\eta)}{p_{\text{jet},T}^{\text{reco}}} \right)}_{=\text{SF}(\eta, p_T)}, \quad (6.1.1)$$

where $p_{\text{jet}}^{\text{reco}}$ denotes the four-momenta before and $p_{\text{jet}}^{\text{reco}}$ after the smearing.

B-tagging and mis-tagging The track counting b-tagging algorithm is used at the “high purity” working point of its discriminator (TCHP). The b-tagging efficiency at the working point states how often a b-tagged jet is correctly identified to originate from a bottom quark. The mis-tagging efficiency states how often a b-tagged jet has received an incorrect b-tag. Mis-tagged jets can originate from up, down, strange, charm quarks or gluons. The “high purity” working point ensures a certain minimum of mis-tagged jets.

However, the measured efficiencies differ from the efficiencies in the simulation [28]. Therefore, the treatment of the b-tagging and mis-tagging efficiency and their systematic uncertainties leads to permutations of the simulated events. The required permutation procedure is described in the following.

The single top quark t-channel signature requires two jets. This leads in total to six permutations that an event from the zero, one or two b-tagged jet category can end up in the same or another b-tag category due to misidentification. Table 6.1 lists these permutations and their probabilities for a generic b-tagging efficiency ϵ .

Table 6.1: The scale factors for the b-tagging efficiency.

		after b-tagging efficiency		
		0 b-tag	1 b-tag (signal)	2 b-tags
before	0 b-tag	1 · 1	-	-
b-tagging	1 b-tag	(1 - ϵ) · 1	ϵ · 1	-
efficiency	2 b-tags	(1 - ϵ) · (1 - ϵ)	(1 - ϵ) · ϵ · 2	ϵ · ϵ

The signal selection requires events with exactly one b-tagged jet. Such selected events have a probability of ϵ to arise from a simulated event where the jet has actually originated from a bottom quark. However, there is a probability that events can be

selected in which both simulated jets originated from a bottom quark. Those events have a probability of $(1 - \epsilon) \cdot \epsilon \cdot 2$ to be measured with only one b-tagged jet due to the possibility that the second jet is not tagged.

To account for those effects, the simulated events are duplicated and allowed to migrate into the different b-tag categories. Their event weight is adjusted to include the corresponding probabilities. The b-tagging efficiency depends furthermore on the transverse momentum of the jet. Additionally, efficiencies for mis-tagged jets are considered.

The migration of simulated events between the b-tag categories is influenced by varying the b-tagging and miss-tagging efficiencies within their measured uncertainties.

Unclustered energy The scale uncertainty and resolution of the missing transverse energy can be factorized into the following objects and their contributing uncertainties: jets, taus, electrons, photons, muons, and unclustered energy. Only jets, muons, and the unclustered energy are relevant for the analysis. The small uncertainty from the muon energy scale and resolution is neglected due to the larger contributions from jets and unclustered energy. For the variations of jets, the JES affect the missing transverse energy as described before. The unclustered energy is varied additionally and the missing transverse energy is recalculated.

An uncertainty of $\pm 10\%$ is applied to the unclustered energy in each simulated event. The procedure follows Ref. [35].

Pile up Multiple interactions can occur in a proton bunch crossing. Those additional interactions (pile up) lead to particles originating from additional vertices. During the event simulation, a uniform distribution with up to ten pile up interactions is assumed. The distribution of the pile up interactions needs to be reweighted to the estimated number of pile up interactions from data. The estimation of the number of pile up interactions in data itself depends on the total inelastic proton-proton cross section $\sigma_{pp \rightarrow X} = 68 \text{ mb} \pm 5\%$ [30]. The uncertainty on the cross section leads to different pile up reweighing factors in the number of vertices distribution.

The number of vertices distribution before the pile up reweighing is shown in figure 6.1a. The assumed uniform distribution from simulation is folded by a Poisson distribution due to the reconstruction of the detector. Figure 6.1b shows the resulting number of vertices distribution of the simulated events after applying the pile up reweighing. The simulated distribution agrees well with the shape from data.

W+jets modeling In figure 6.2a, the distribution for $\cos_{\text{spec., muon}}$ in the control region with two jets and non b-tagged jet is shown. The control region is dominated by

6.1 Systematic Uncertainties

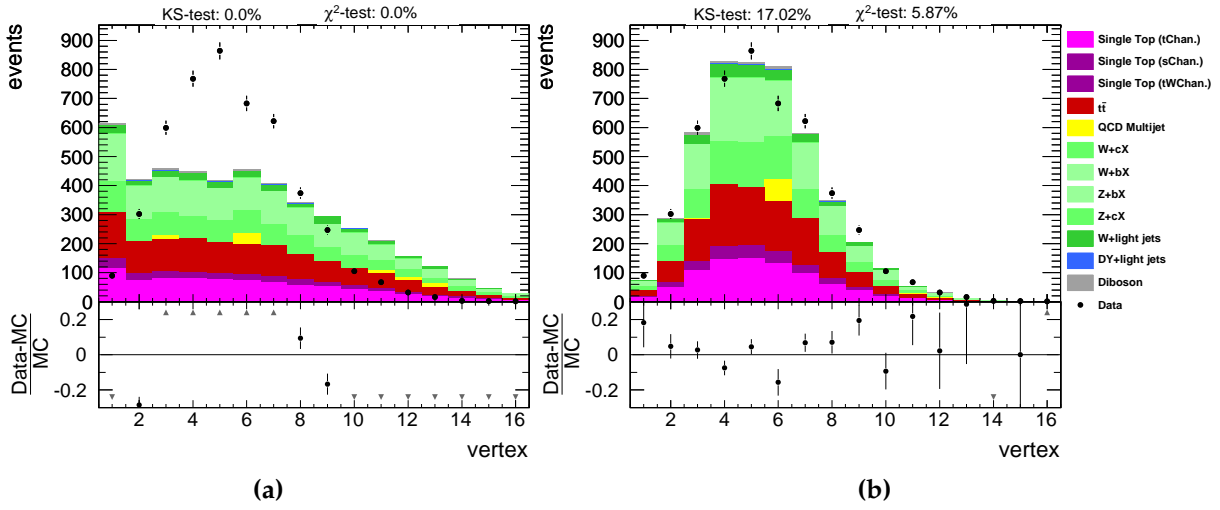


Figure 6.1: Number of vertices distribution for the simulated events with Powheg. The simulated distributions are normalized to data. The figures show the distributions before (a) and after (b) the pile up reweighting.

$W(\rightarrow l\nu) + \text{jets}$ contributions. The simulation of the $W(\rightarrow l\nu) + \text{jets}$ samples does not agree in shape with the data.

Scale factors are derived from the control region for the $W(\rightarrow l\nu) + \text{jets}$ samples (figure 6.2b). The scale factors are used for reweighting in the two jets and one b-tagged jet signal region to account for the $W(\rightarrow l\nu) + \text{jets}$ modeling. The $W(\rightarrow l\nu) + \text{jets}$ shape uncertainty is considered by varying around the reweighted distribution. Variations without scale factors and doubled scale factors are used to estimate the uncertainties of the shape extrapolation from this control region to the signal region.

Trigger efficiency Muon trigger efficiencies depending on the pseudorapidity of the muon are applied. The uncertainty is conservatively estimated by $\pm 3\%$ over the measured pseudorapidity range.

Luminosity The luminosity of the recorded data is measured by counting the number of the hit pixel clusters for each event [43]. The amount of total interactions is a linear function of that number. Together with the beam profile and the inclusive proton-proton cross section the luminosity is calculated [27]. The uncertainty of the luminosity measurement is estimated to $\pm 2.2\%$ [43].

Cross sections Each of the simulated processes have been assigned with a certain weight which scales its yield according to the theoretical cross section. To account for

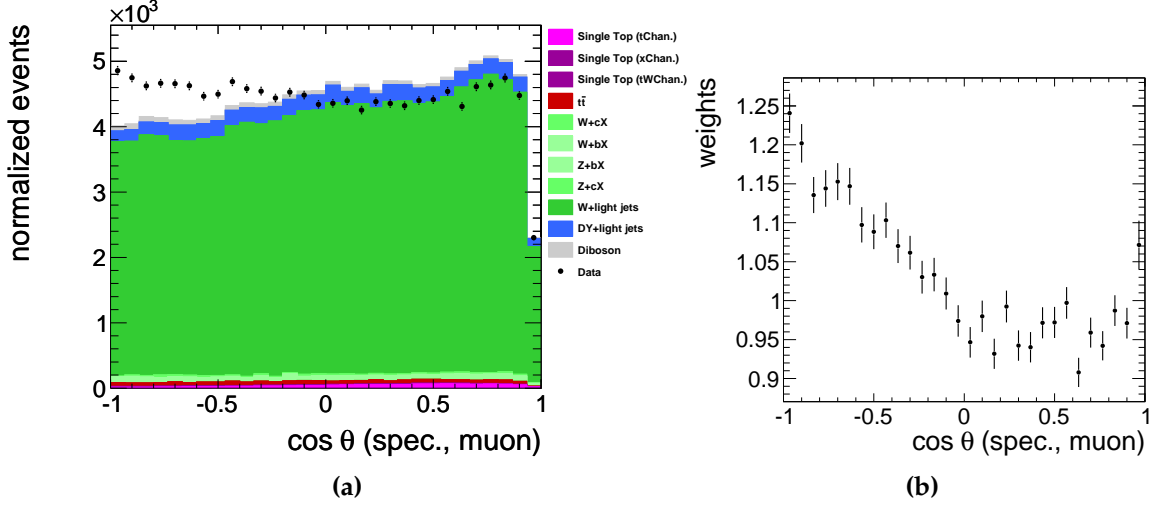


Figure 6.2: Distribution of $\cos_{\text{spec., muon}}$ in the two jet and non b-tagged jet control region.

uncertainties on the cross section and modeling, in the particular phase space of this analysis, the following variations of the cross sections are applied:

- The single top quark t-channel cross section including the W boson decaying into tau and neutrino ($t \rightarrow b\tau\nu$) is varied by $\pm 10\%$.
- The single top quark s-channel and tW-channel cross sections are varied each by $\pm 30\%$.
- A $\pm 15\%$ variation is used for the $t\bar{t}$ cross section.
- The contributions from the “DY+light flavor”, “Z+bX”, and “Z+cX” samples are independently varied by $\pm 30\%$ to account also for the possible modeling uncertainties of their branching ratios.
- For the “W+light jets” process, an uncertainty of $\pm 50\%$, and for the “W+cX” and “W+bX” processes, an uncertainty of $\pm 100\%$ is assigned independently.
- The di-boson processes, WW, WZ, and ZZ, are each varied independently by $\pm 30\%$.

The described uncertainties are implemented in a THETA model. The differential $\frac{d\sigma}{d\cos\theta_{B,X}}$ distributions are implemented as observables. Nuisance parameters are assigned to each uncertainty. Gaussian distributions are mainly used for the nuisance parameters. The nuisance parameters for the cross section uncertainties are allowed to vary in the interval $[0; \infty]$. The mean and variance of such truncated Gaussian distributions can change significantly if they are used for large uncertainties, e.g. “W+bX”. Therefore, log-normal distributions are used instead of Gaussian distributions for all cross section uncertainties.

6.1 Systematic Uncertainties

Uncertainties which influence the $\frac{d\sigma}{d\cos\theta_{B,X}}$ shape are implemented using histogram templates. THETA automatically morphs the $\frac{d\sigma}{d\cos\theta_{B,X}}$ shape by extrapolating between the provided templates according to the nuisance parameter.

6.1.2 Fit to the top quark mass

Figure 6.3a shows the distribution of the reconstructed top quark mass. The overall yield from the simulated events underestimates the data events. Therefore, a maximum likelihood fit of the signal and background processes to the data is performed. The resulting yield estimates from the fit are taken to scale the simulated events to the observed data.

Figure 6.3b shows the top quark mass distribution of the simulated $W(\rightarrow l\nu) + \text{jets}$ background and of the different anomalous coupling scenarios. The following two facts motivate to use the reconstructed top quark mass distribution as the fit variable:

First, the shape between the $W(\rightarrow l\nu) + \text{jets}$ and single top quark t-channel top quark mass distribution is quite different. The fit profits from the shape differences by constraining background and signal contributions nearly uncorrelated to each other.

Second, there are neglectable shape differences between the anomalous coupling scenarios. A potential bias on the top quark spin asymmetries by a fit to the top quark mass is minimized.

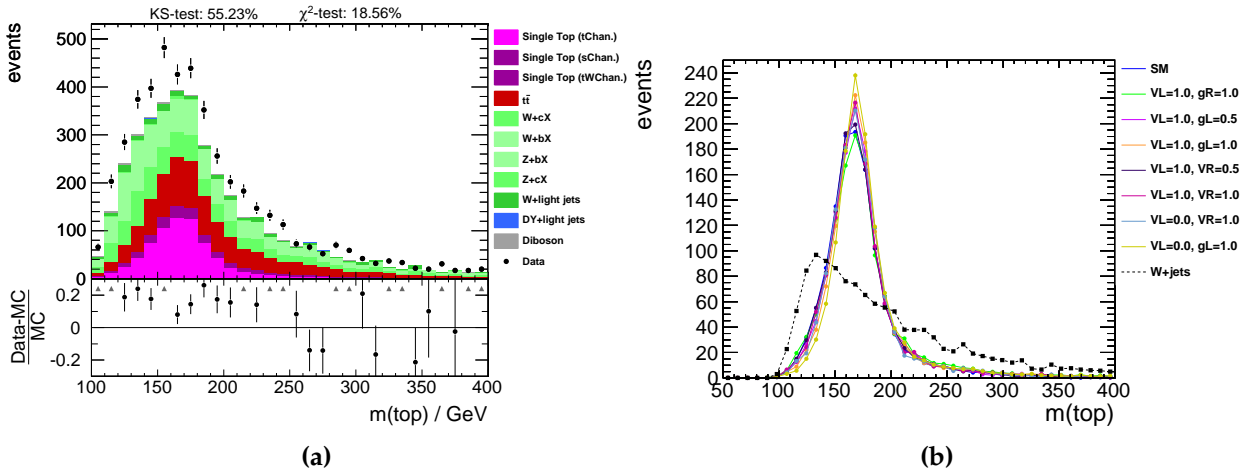


Figure 6.3: The reconstructed top quark mass distribution before the data-driven $W+\text{jets}$ estimation.

Table 6.2 lists the nuisance parameters before and after the maximum likelihood fit of the signal and background processes to data. Nuisance parameters that influence the shape morphing are denoted as δ parameters. A width of 1.0 means a $\pm 1\sigma$ variation.

Nuisance parameters that change only the simulated event yields are denoted as β parameters.

The fit constrains the JES, JER, b-tag efficiency, mis-tag efficiency, unclustered energy, pile up, and W+jet shape uncertainties. The mean values of the JES, JER, b-tag efficiency, mis-tag efficiency, unclustered energy, pile up, and W+jet shape uncertainties after the fit are compatible with the pre-fit input values.

The fit indicates that the “W+bX” contribution is underestimated by a factor of 1.67. The “W+bX” yield uncertainty is also negatively correlated to the “W+cX” yield by $\rho = -0.86$. This negative correlation is taken into account for the evaluation of the $\frac{d\sigma}{d\cos\theta_{B,X}}$ distributions. The full correlation matrix from the fit is shown in the appendix.

The fit constrains the events yield uncertainties of the single top quark t-channel (signal), single top quark s-channel, single top quark tW-channel, $t\bar{t}$, W+light jets, Z+jets, WW, WZ, and ZZ contributions only marginally. Those constraints are also neglected.

In conclusion, the fit to the reconstructed top quark mass distribution shows that the simulated “W+bX” contribution needs to be rescaled. The reconstructed top quark mass distribution with the rescaled “W+bX” yield is shown in figure 6.4. It shows an improved agreement with data.

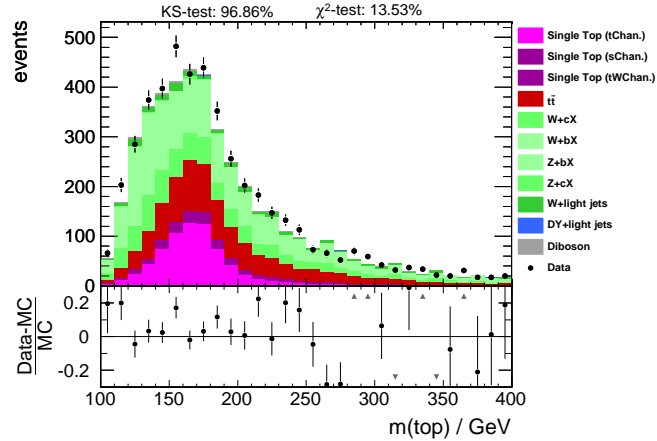


Figure 6.4: The reconstructed top quark mass distribution after scaling the W+bX contribution to the fit result.

An improved agreement is also present in other variables. In figure 6.5, the pseudorapidity of the light jet, the HFS mass, and the missing transverse energy is shown before (6.5a, 6.5c, 6.5e) and after the rescaling (6.5b, 6.5d, 6.5f). Those distributions demonstrate that the excess of the “W+bX” contribution is reasonable not only for the reconstructed top quark mass, but also for other variables.

6.1 Systematic Uncertainties

systematic uncertainty	before fit		after fit	
	mean	uncertainty	mean	uncertainty
δ_{JES}	0.000	1.000	-0.091	0.688
δ_{JER}	0.000	1.000	0.181	0.717
$\delta_{\text{b-tag efficiency}}$	0.000	1.000	0.564	0.911
$\delta_{\text{mis-tag efficiency}}$	0.000	1.000	-0.007	0.987
$\delta_{\text{unclustered energy}}$	0.000	1.000	0.117	0.362
$\delta_{\text{pile up}}$	0.000	1.000	-0.227	0.974
$\delta_{\text{W+jets shape}}$	0.000	1.000	0.251	0.961
$\beta_{\text{signal \& (t} \rightarrow \text{b}\tau\nu)}$	1.000	0.100	1.051	0.086
$\beta_{\text{luminosity}}$	1.000	0.022	1.005	0.022
$\beta_{\text{muon trigger efficiency}}$	1.000	0.030	1.010	0.029
$\beta_{\text{single top quark s-channel (t)}}$	1.000	0.300	0.933	0.273
$\beta_{\text{single top quark s-channel (}\bar{\text{t}}\text{)}}$	1.000	0.300	0.929	0.271
$\beta_{\text{single top quark tW-channel (t)}}$	1.000	0.300	0.940	0.278
$\beta_{\text{single top quark tW-channel (}\bar{\text{t}}\text{)}}$	1.000	0.300	0.942	0.268
$\beta_{\text{t}\bar{\text{t}}}$	1.000	0.150	1.001	0.126
$\beta_{\text{W+light jets}}$	1.000	0.500	0.830	0.323
$\beta_{\text{W+cX}}$	1.000	1.000	0.948	0.596
$\beta_{\text{W+bX}}$	1.000	1.000	1.670	0.521
$\beta_{\text{DY+light jet}}$	1.000	0.300	0.941	0.269
$\beta_{\text{Z+cX}}$	1.000	0.300	0.948	0.275
$\beta_{\text{Z+bX}}$	1.000	0.300	0.964	0.299
β_{WW}	1.000	0.300	0.928	0.275
β_{WZ}	1.000	0.300	0.927	0.277
β_{ZZ}	1.000	0.300	0.924	0.263

Table 6.2: Results from fit to the reconstructed top quark mass. Uncertainties are denoted in standard deviations for shape systematic (δ) and in percental fractions for yield systematic (β).

6.1.3 Impact of Uncertainties

Pseudo experiments are performed to generate $\frac{d\sigma}{d\cos\theta_{B,X}}$ distributions by dicing around the systematic uncertainties. The expected nominal background from each generated distribution is subtracted. A probability distribution for the asymmetry is obtained from the pseudo experiments. The mean and uncertainty of the asymmetry is estimated by calculating the $\pm 1\sigma$ and 50% quantiles from the distribution.

Table 6.2 presents the impact of each source of systematic on the asymmetry for the angle between the muon spin analyzer in the spectator basis ($\cos_{\text{spec.}, \mu\text{on}}$). The BDT with 70 input variables and a discriminator value of 0.075 is used to calculate the values in this table. The impact of each single systematic uncertainty is calculated by generating only pseudo experiments for each systematic separately. The total uncertainty is obtained by varying all systematic uncertainties together.

Table 6.3: Impact of systematic uncertainties.

JES	$0.465^{+0.015}_{-0.004}$	signal	$0.465^{<+0.001}_{<-0.001}$
JER	$0.465^{+0.031}_{-0.014}$	fake (tau) events	$0.465^{<+0.001}_{<-0.001}$
b-tagging efficiency	$0.465^{+0.079}_{-0.054}$	single top s-channel	$0.465^{+0.002}_{-0.002}$
mis-tagging efficiency	$0.465^{<+0.001}_{<-0.001}$	single top tW-channel	$0.464^{+0.011}_{-0.012}$
unclustered energy	$0.473^{+0.048}_{-0.010}$	$t\bar{t}$	$0.464^{+0.042}_{-0.039}$
pile up	$0.465^{+0.004}_{-0.003}$	W+light jets	$0.465^{+0.024}_{-0.032}$
W+jet shape	$0.466^{+0.144}_{-0.155}$	W+bX / W+cX	$0.454^{+0.141}_{-0.105}$
muon efficiency	$0.465^{+0.043}_{-0.033}$	DY+jets	$0.465^{+0.006}_{-0.008}$
luminosity	$0.465^{+0.030}_{-0.026}$	WW, WZ, ZZ	$0.464^{+0.005}_{-0.006}$
total	$0.472^{+0.197}_{-0.183}$		

It is concluded from table 6.2 that the main uncertainty on the asymmetry measurement originates from the considered W+bX / W+cX uncertainty and from the W+jet shape modeling. The smallest impact on the asymmetry measurement originates from the signal uncertainty, the uncertainty from the fake (tau) events, and from the mis-tagging efficiency uncertainty. For those uncertainties, their impact is estimated by less than ± 0.001 .

6.1 Systematic Uncertainties

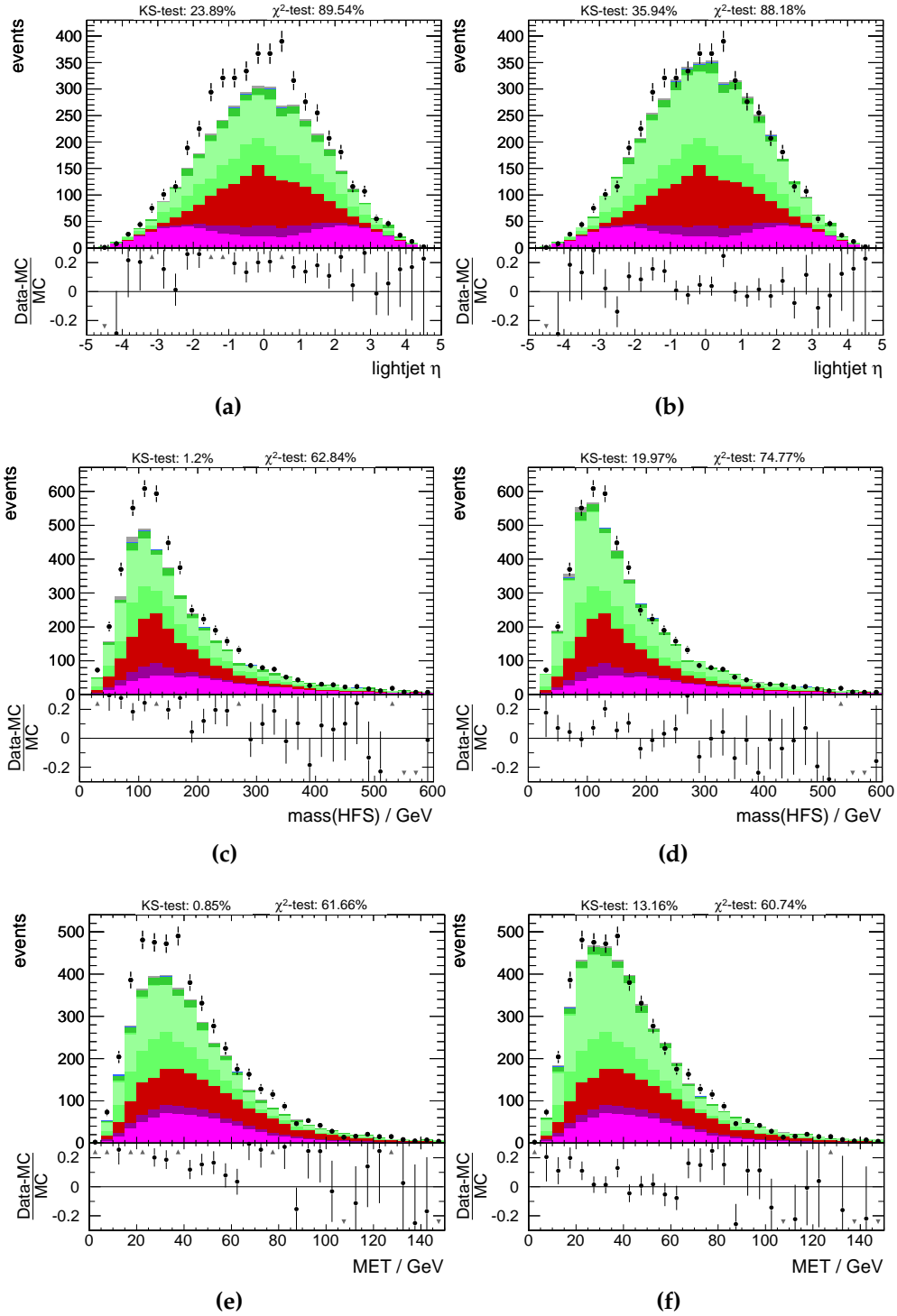


Figure 6.5: Event variables before and after the fit to the reconstructed top quark mass. The pseudorapidity of the light jet before (a) and after (b) the fit. The HFS mass before (c) and after (d) the fit. The missing transverse energy before (e) and after (f) the fit.

6.2 Measurement Procedure

The measurement procedure is presented in figure 6.6. The simulated anomalous coupling events are combined with the simulated background events.

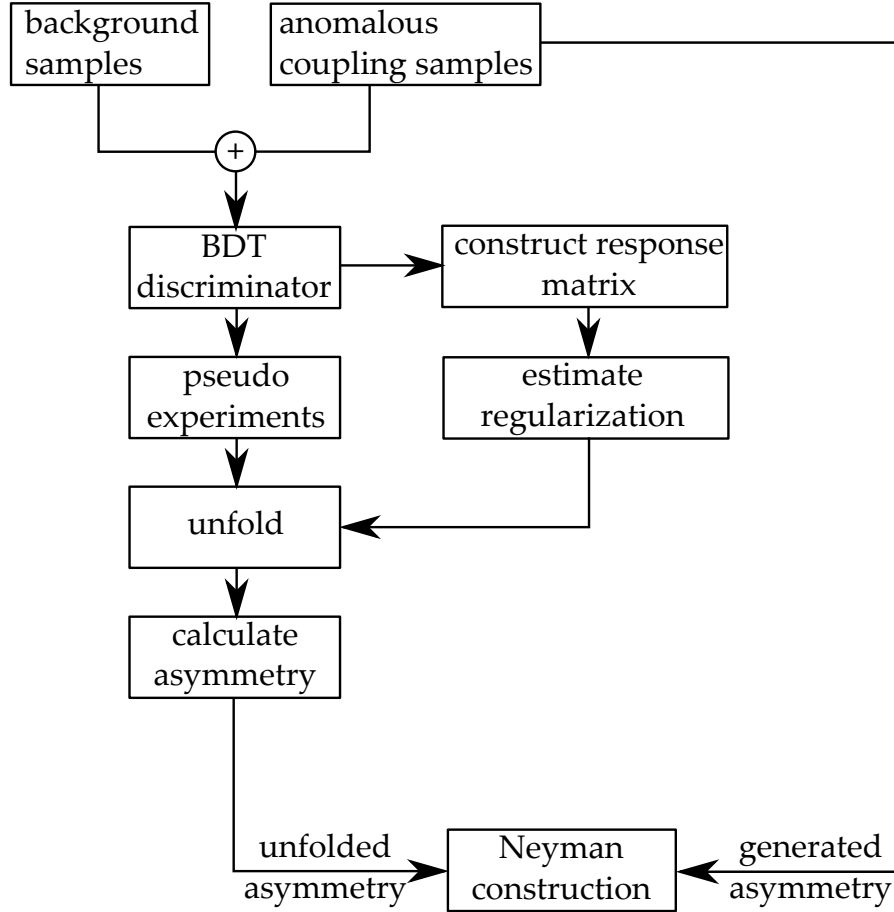


Figure 6.6: Measurement procedure with Neyman construction.

A Boosted Decision Tree separates between the signal and background processes. Pseudo experiments are generated to propagate the uncertainties through the unfolding procedure. The propagation of uncertainty is performed by unfolding each generated pseudo distribution. For a certain bin after the unfolding, the resulting yield distribution over all pseudo experiments is then equal to a probability density. The standard deviation is obtained from the resulting probability distribution by calculating the 50% and $\pm 1\sigma$ quantiles for each bin.

The response matrix for the unfolding is always constructed from the anomalous coupling sample with $V_L = V_R = 1$, $g_L = g_R = 0$. This sample provides a nearly uniform $\frac{d\sigma}{d\cos\theta_{B,X}}$ distributions for all spin analyzers X (figure 6.7) at generation level.

6.2 Measurement Procedure

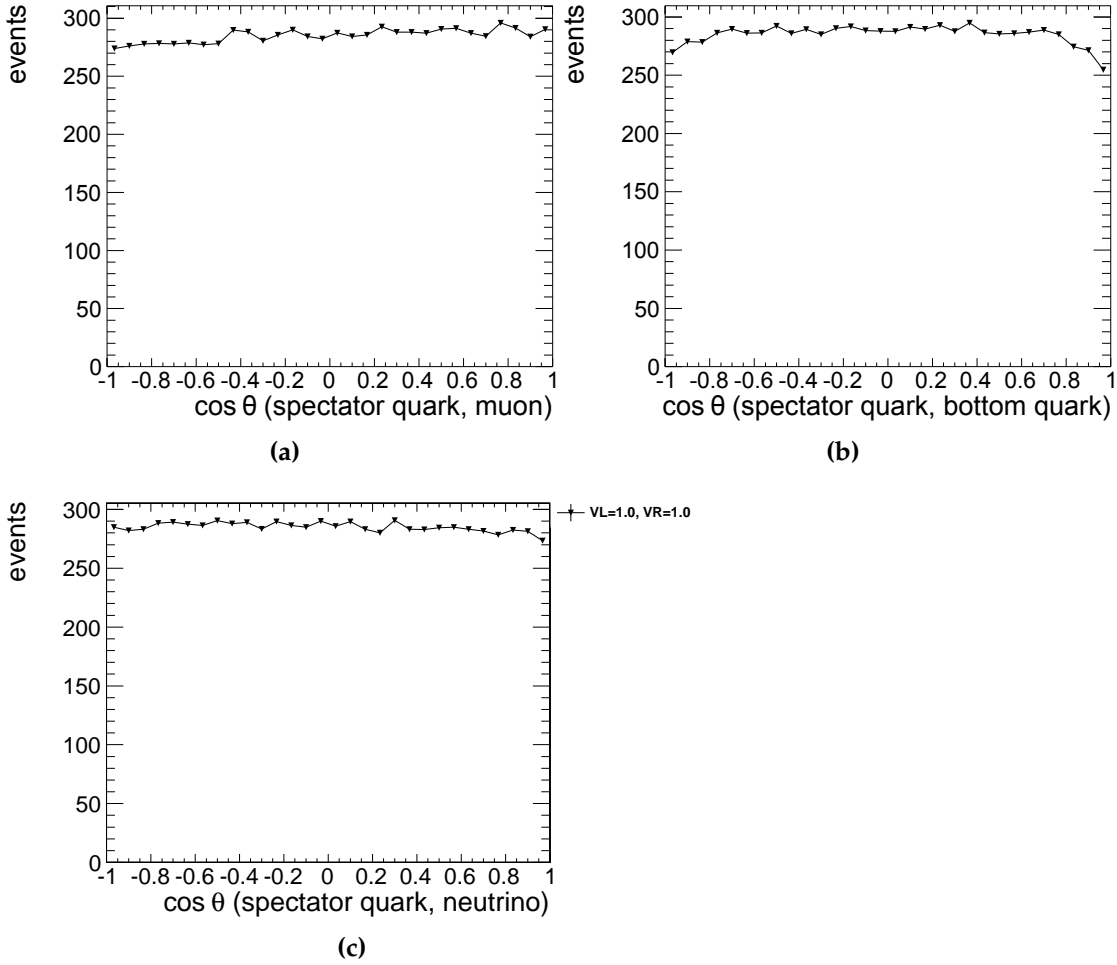


Figure 6.7: The anomalous coupling sample with $V_L = V_R = 1$, $g_L = g_R = 0$ from which the response matrices are constructed. The $\frac{d\sigma}{d\cos\theta_{B,X}}$ distributions for the (a) muon , (b) the b-tagged jet, and (c) the neutrino as spin analyzer in the spectator basis.

The uniformity ensures that the influence on the response matrix due to the limited simulated event statistics can be neglected. After the construction of the response matrix, the regularization parameter is estimated.

The unfolded asymmetry is calculated from each unfolded pseudo $\frac{d\sigma}{d\cos\theta_{B,X}}$ distribution. The mean and uncertainty of the reconstructed asymmetry is obtained from the asymmetry distribution over all pseudo experiments by calculating the 50% and $\pm 1\sigma$ quantiles.

Each simulated anomalous coupling scenario is evaluated with the described measurement procedure. For each simulated anomalous coupling scenario, the reconstructed asymmetry and the generated asymmetry are compared. This so-called Neyman construction is presented schematically in figure 6.8.

The total uncertainty on an asymmetry measurement from data is obtained by constructing an uncertainty belt in parallel to the angle bisector. The uncertainty belt has to cover a potential bias which may occur due to the event selection, the signal separation, or the unfolding. Furthermore, only a few anomalous coupling scenarios are tested. Therefore, the uncertainty belt has to account for the extrapolation from a few anomalous coupling scenarios into the complete coupling space. The uncertainty belt is estimated conservatively by using the most distant 68% confidence levels amongst the unfolded distributions from all anomalous coupling samples. The distance is calculated from the angle bisector.

Additionally, the asymmetry measurement is checked for compatibility with the SM coupling case. This is performed by calculating the significance of the data from the probability distribution of the simulated SM asymmetry from the pseudo experiments.

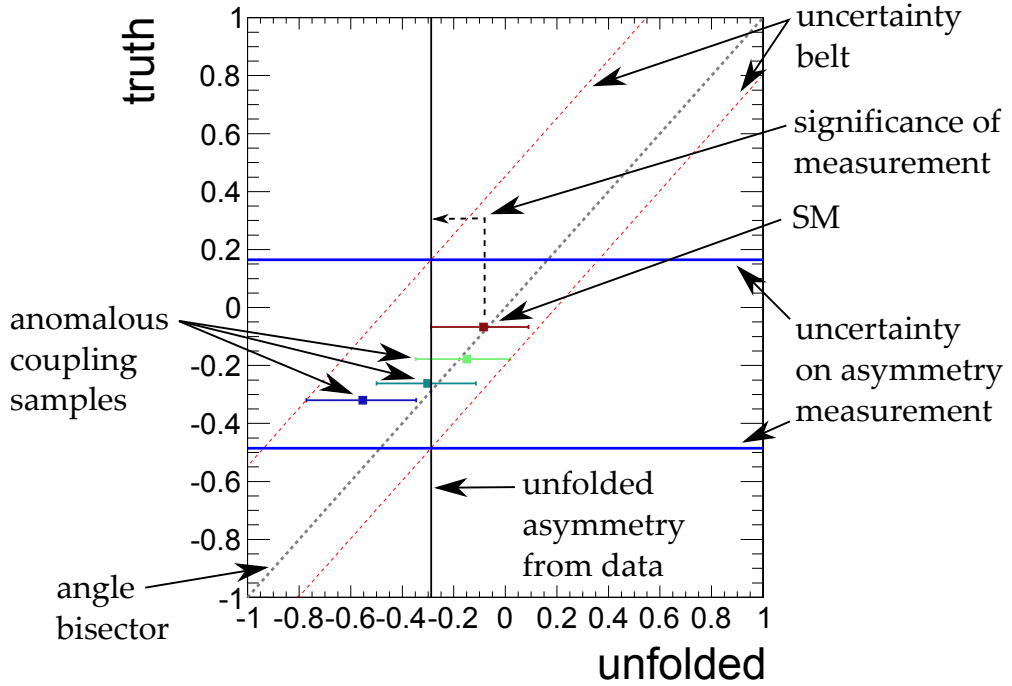


Figure 6.8: Schematic Neyman construction.

6.3 Optimization

The measurement procedure depends on the used Boosted Decision Tree and its working point. Twenty Boosted Decision Trees are trained within this analysis. Each is trained with a certain amount of less-correlated variables to $\cos_{B,X}$. An optimization is applied to find the best Boosted Decision Tree and its working point with the smallest expected total uncertainty.

6.3 Optimization

First, all Boosted Decision Tree discriminator outputs are scanned for the best working point to find the smallest uncertainty after the unfolding. Some discriminator outputs and the results from the scanning for the muon spin analyzer in the spectator basis ($\cos_{\text{spec.}, \mu\text{on}}$) are shown in figure 6.9. The stacking order is changed to visualize the purity of the signal over the background contributions at the high discriminator output.

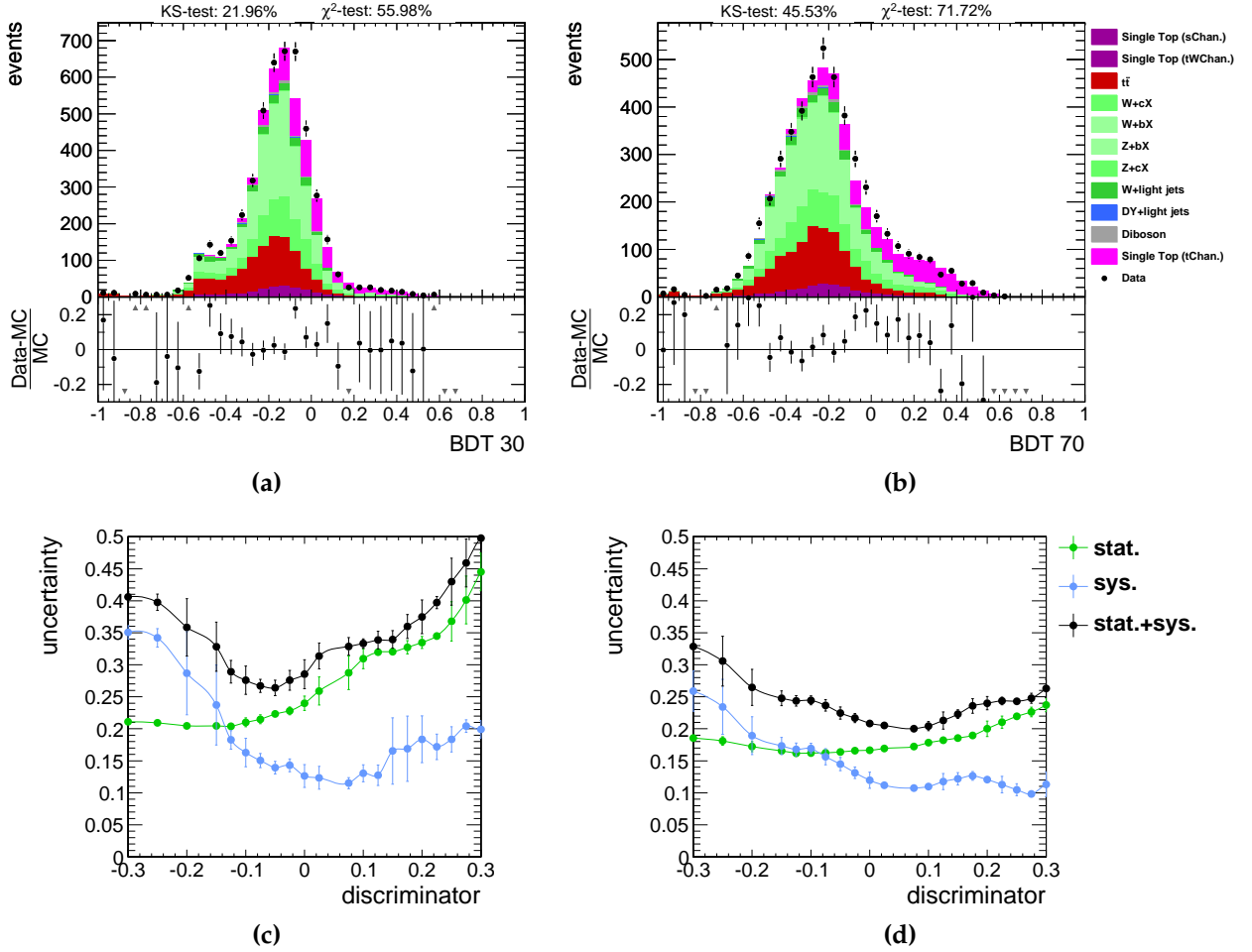


Figure 6.9: BDT outputs and asymmetry uncertainty for different discriminator values. The BDT discriminator output with thirty input variables (a) and 70 input variables (b). The resulting uncertainty on the asymmetry by scanning the BDT 30 output (c) and BDT 70 output (d).

In figure 6.9a the discriminator output for the BDT from the first thirty less correlated input variables is shown. The resulting uncertainty on the asymmetry measurement is calculated as a function of the discriminator output in figure 6.9c. The green curve corresponds to the resulting statistical uncertainty on the asymmetry measurement. The blue curve shows the influence of the systematic uncertainties. The lines are produced

by generating pseudo experiments and excluding either the statistical or the systematic uncertainty. The black curve shows the total uncertainty. The lines are smoothed by averaging each point over its two adjacent points. The vertical bar on each point shows the corresponding variations through the averaging.

For small discriminator values, the systematic uncertainty becomes the dominant contribution because the background processes and their uncertainties are large. For high discriminator values, only the systematic uncertainty from the signal process remains. However, the statistical uncertainty increases as the signal selection efficiency decreases. The optimal discriminator value (working point) is set to the minimum of the both uncertainties (black line). This point resembles a tradeoff between the systematic and statistical uncertainties.

In figure 6.9b, the BDT output for the first 70 input variables is shown. Figure 6.9d shows the scanning result. A working point for this discriminator is found again by selecting the minimum.

Figure 6.10 shows the resulting top quark spin asymmetries and their uncertainties for the muon, b-tagged jet, and neutrino spin analyzer in the spectator basis against the number of used input variables for the BDT.

It is expected that a BDT with a few variables results in a large uncertainty for the asymmetry measurement, because it is much less discriminant than a BDT with a high number of input variables. On the other hand, a BDT with more variables may introduce a bias by favoring events with the coupling scenario that has been used for its training. This bias would be visible in an increase in the asymmetry uncertainty. However, figure 6.10 does not present a significant increase in uncertainty for a BDT with many input variables. It is concluded that both effects, the discrimination power versus a potential bias, are happening at different scales.

For the measurement, the BDT with 70 input variables is chosen. It has for all three top quark asymmetries (figures 6.10b, 6.10d, 6.10f) the smallest uncertainties.

As a cross check, the signal separation in the measurement procedure is switched from the BDTs to Projective Likelihood Estimators (PLEs). The discriminator output of the PLE trained with 50 and 70 variables are shown in figure 6.11. The discriminator output distribution of the PLEs highly differs in shape from the BDT discriminator output. Events are nearly exclusively found at output values of -1.0 or 1.0 . The scanning of the optimal working point for the PLEs is skipped due to this extreme output shape.

A discriminator value of 0.9 is used to investigate the uncertainty on the asymmetry measurement with the PLE method. Figure 6.12 shows the asymmetry of the muon spin analyzer in the spectator basis against the number of used input variables.

The asymmetry and its uncertainty seems to converge when at least 50 input variables are used. A local minimum is also present if the PLE is trained with 70 input variables.

6.3 Optimization

The measurement procedure is conducted with PLE with 70 input variables for the comparison of the measurement results obtained with the BDT. For the chosen PLE, the asymmetry measurement has a larger uncertainty than the measurement with the BDT.

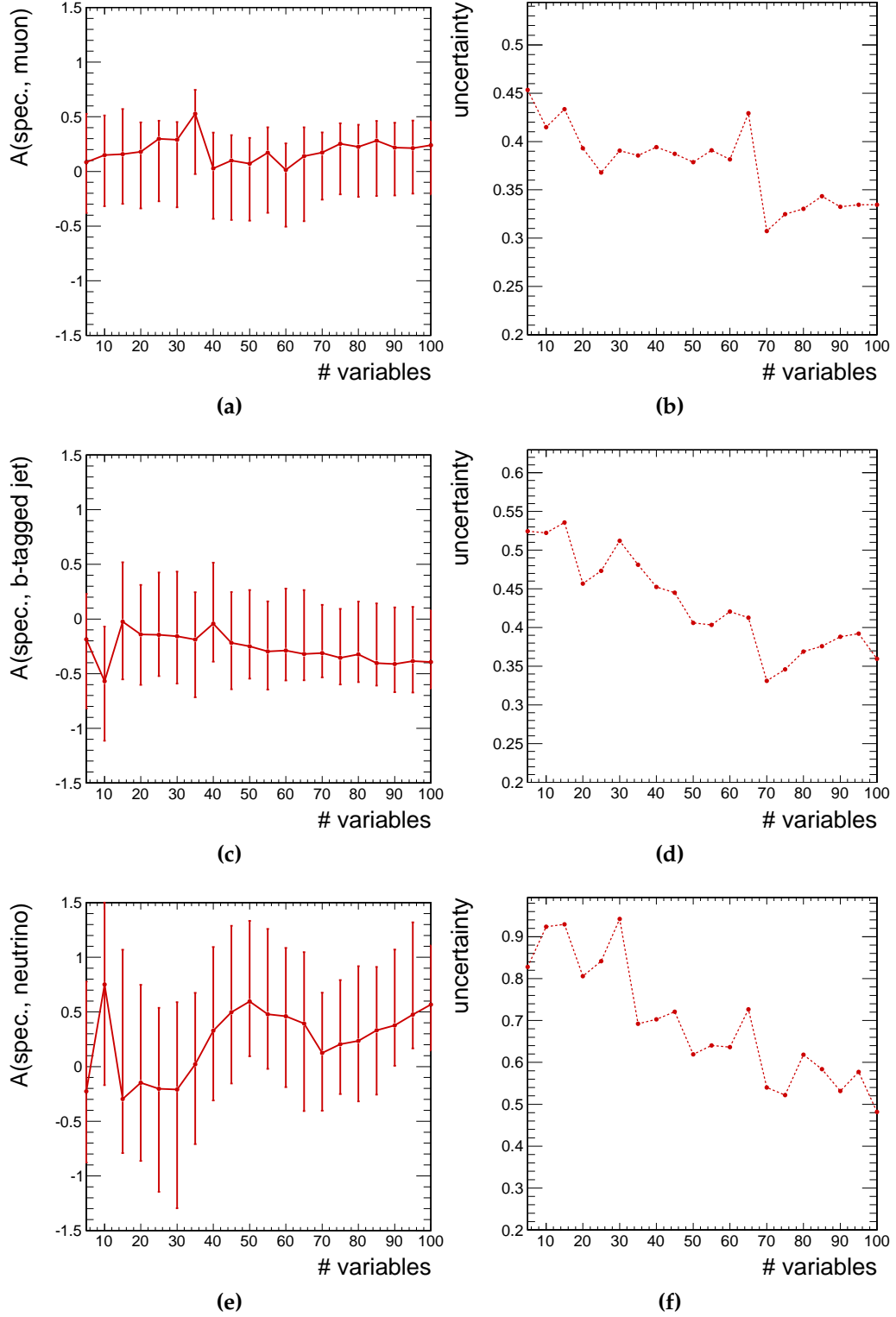


Figure 6.10: Top quark spin asymmetries and their uncertainties in the spectator basis after the Neyman construction with the BDT method. (a) , (c), and (e): The asymmetry for the muon, b-tagged jet, and neutrino spin analyzer and their corresponding uncertainties (b), (d), and (f).

6.3 Optimization

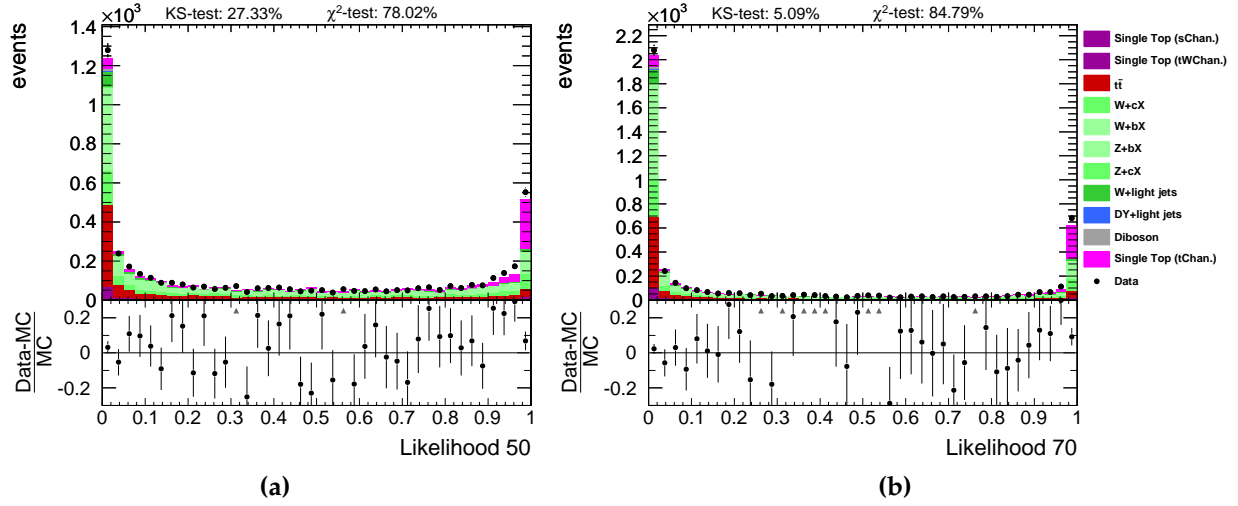


Figure 6.11: Exemplary PLE outputs. (a) shows the PLE output with 50 and (b) with 70 input variables.

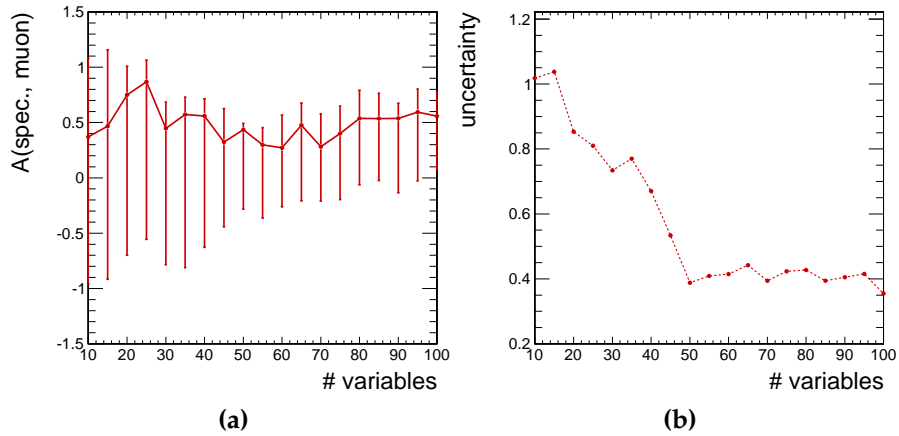


Figure 6.12: Top quark spin asymmetries and their uncertainties in the spectator basis after the Neyman construction with the PLE method.

6.4 Results

6.4.1 The Unfolded Distributions

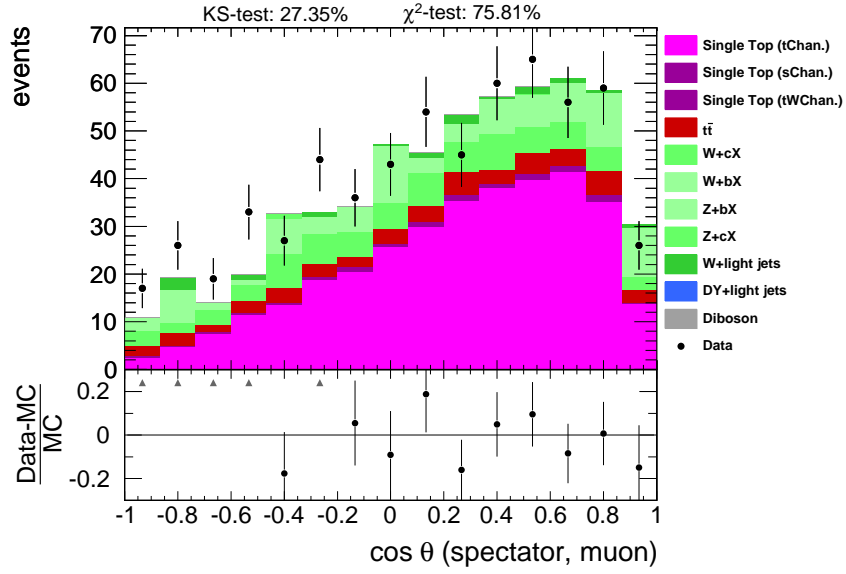
During the measurement procedure, the $\frac{d\sigma}{d\cos\theta_{B,X}}$ distributions are unfolded into the inclusive phase space (with only the selection criterion of $p_{\text{lightjet}} > 20 \text{ GeV}$). Figure 6.13a shows the $\frac{d\sigma}{d\cos\theta_{B,X}}$ distribution with statistical uncertainties for the muons spin analyzer X in the spectator basis B. The BDT selection criterion is applied to these events.

The statistical and systematic uncertainties are evaluated using the pseudo experiments and applied to the data. Figure 6.13b shows the unfolded distribution after the expected background from simulation is subtracted from data. The blue line shows the expected distribution from the simulated SM scenario.

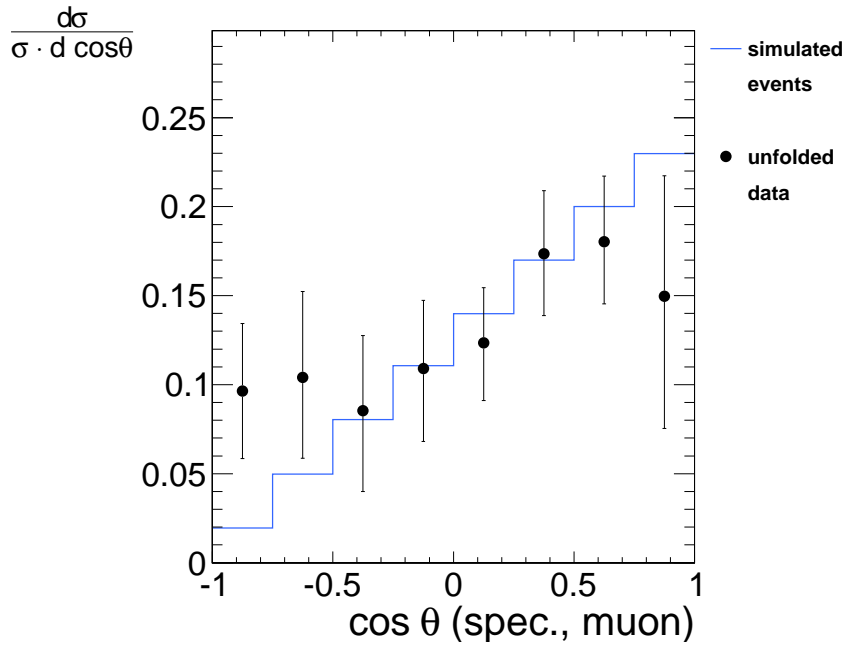
The distributions for the b-tagged jet and the neutrino spin analyzer in the spectator basis before and after the unfolding are shown in figures 6.14 and 6.15. The distribution for the neutrino spin analyzer (figure 6.15a) and the b-tagged jet spin analyzer (figure 6.14a) are well compatible to the simulated events.

The distributions for the beamline basis are shown in the appendix.

6.4 Results

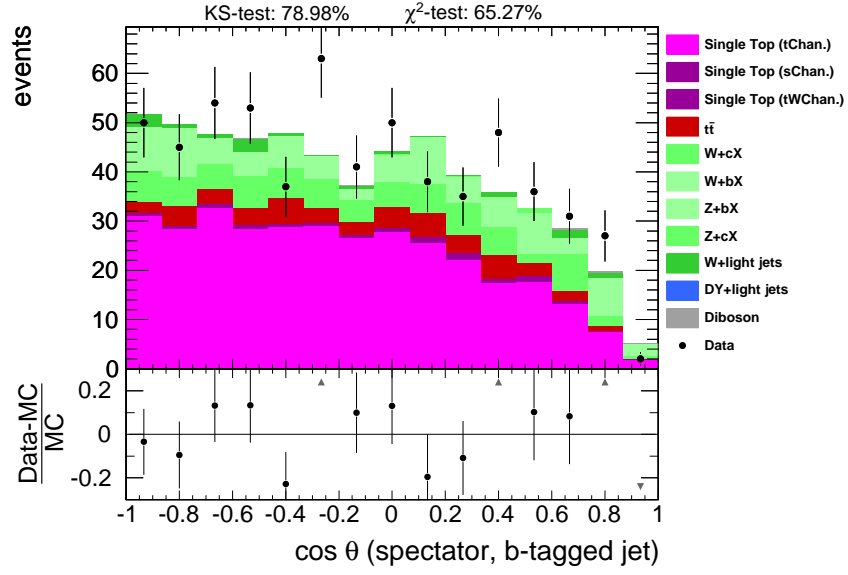


(a)

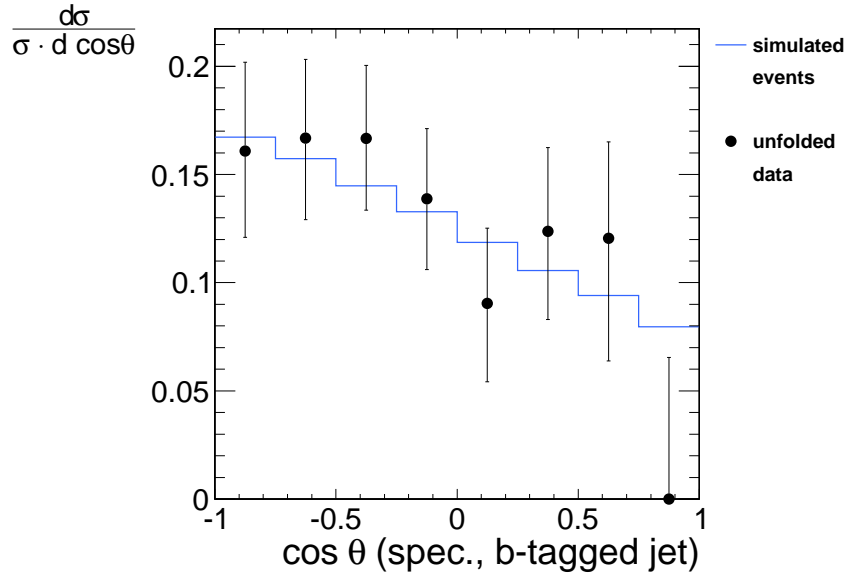


(b)

Figure 6.13: The $\frac{d\sigma}{d \cos \theta_{\text{spec, muon}}}$ before (a) and after (b) the unfolding.



(a)



(b)

Figure 6.14: The $\frac{d\sigma}{d \cos \theta_{\text{spec, b-tagged jet}}}$ before (a) and after (b) the unfolding.

6.4 Results

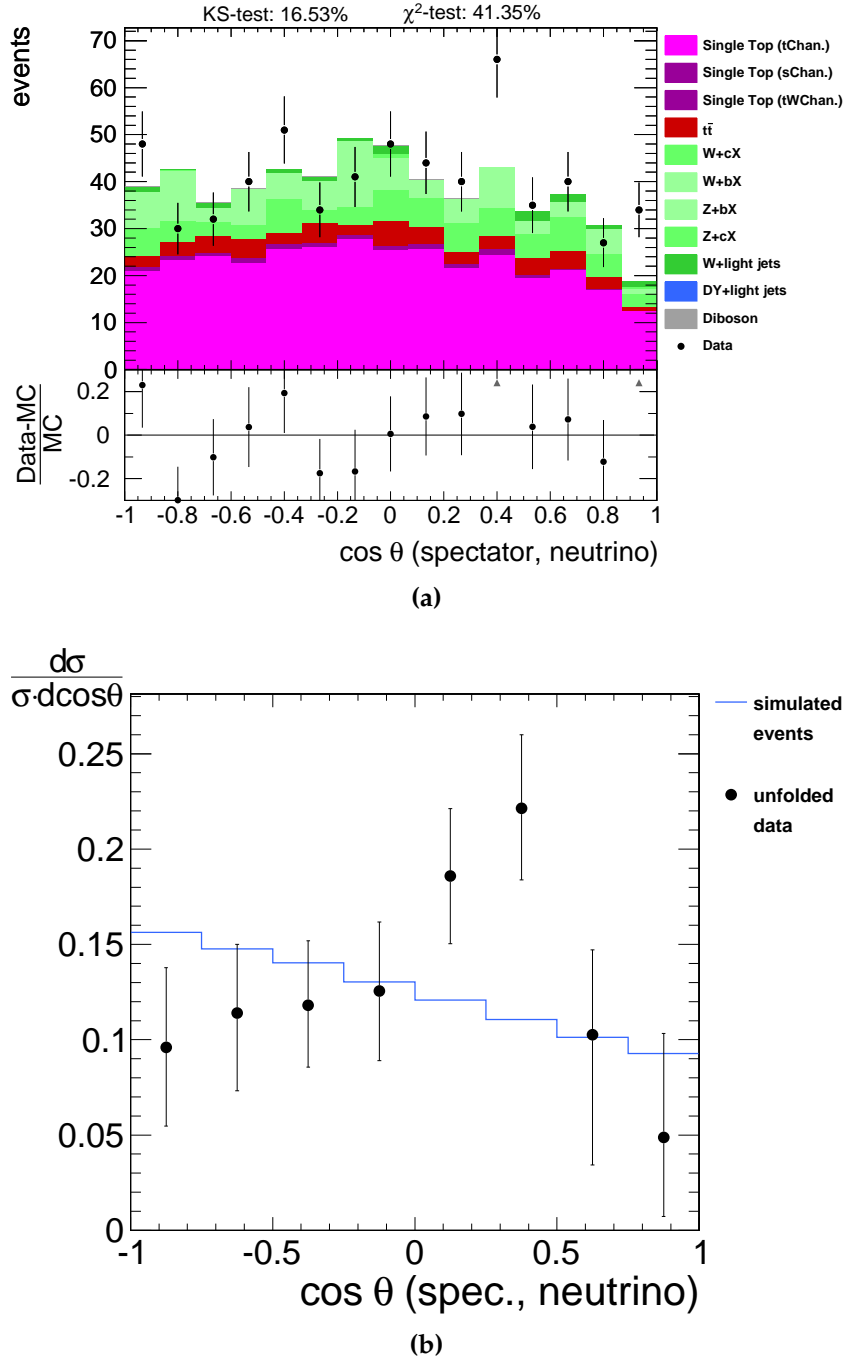


Figure 6.15: The $\frac{d\sigma}{d\cos\theta_{\text{spec, neutrino}}}$ before (a) and after (b) the unfolding.

6.4.2 The Top Quark Spin Asymmetries

The measured top quark spin asymmetries are obtained from the Neyman constructions shown in figures 6.17, 6.18, and 6.19. The legend for the plots is shown in figure 6.16. The figures present the final result of the measured top quark spin asymmetries for the three spin analyzers (muon, b-tagged jet, neutrino) in the two basis (spectator, beamline).

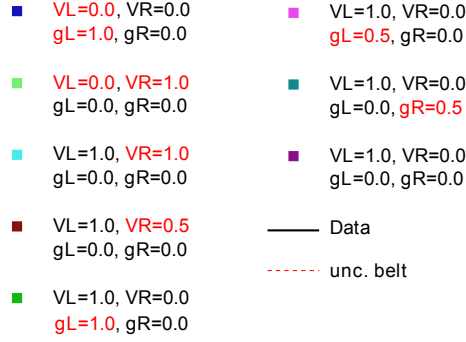


Figure 6.16: The used legend for the Neyman constructions.

The figures show the final results of the top quark spin asymmetries measurement. Table 6.4 lists the measured asymmetries. Slightly smaller uncertainties are obtained by using the spectator basis.

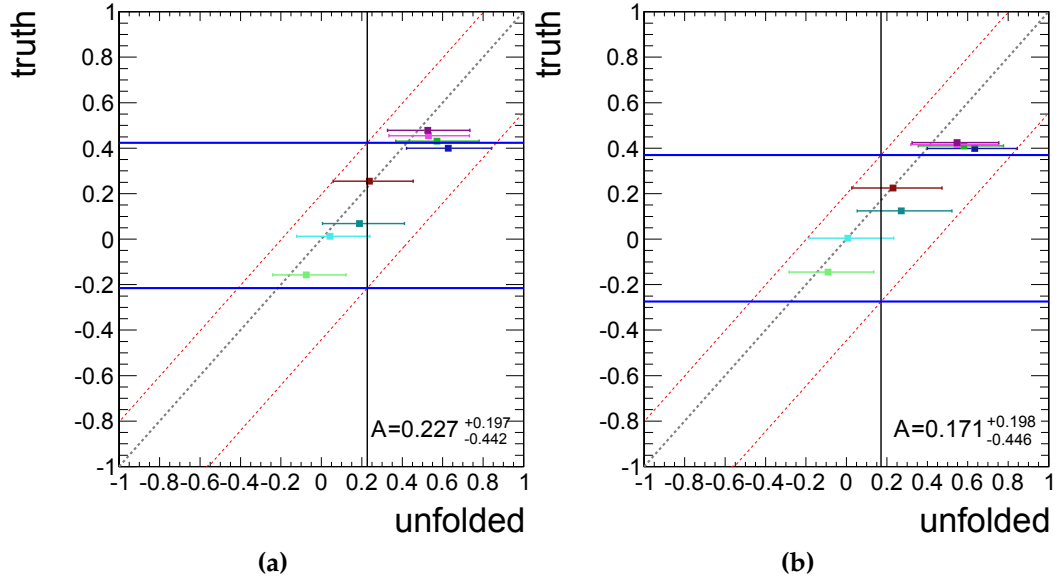


Figure 6.17: The top spin asymmetry measurement for the muon spin analyzer. (a): spectator basis, (b) beamline basis.

6.4 Results

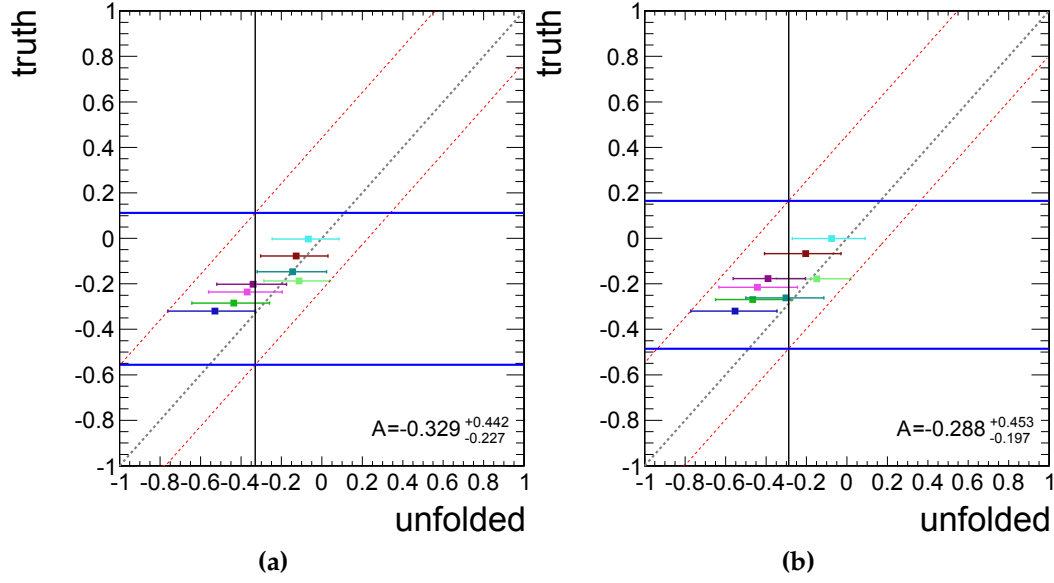


Figure 6.18: The top spin asymmetry measurement for the b-tagged jet spin analyzer. (a): spectator basis, (b) beamline basis.

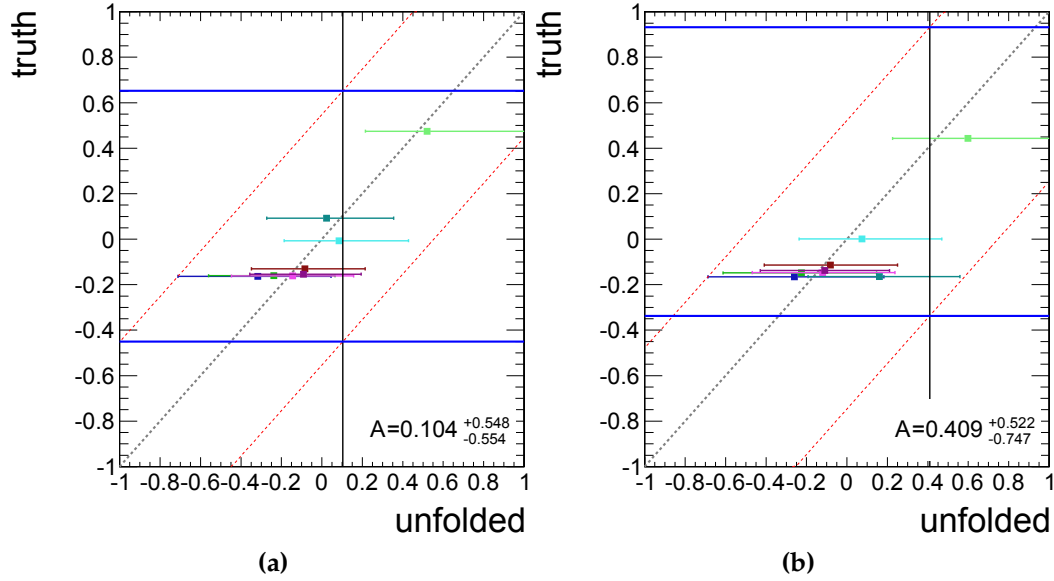


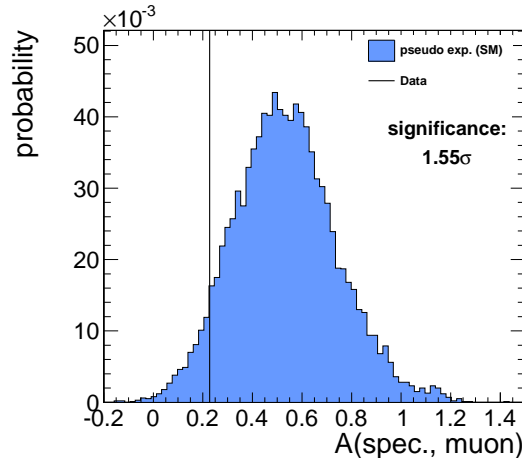
Figure 6.19: The top spin asymmetry measurement for the neutrino spin analyzer. (a): spectator basis, (b) beamline basis.

The observed deviation between the data and the SM prediction is translated into a significance. The calculation of the p-value and the significance using the pseudo experiments is exemplary shown in figure 6.20 for $A_{\mu}^{\text{spec.}}$.

The measured asymmetry of $A_{\mu}^{\text{spec.}} = 0.23$ for the muon spin analyzer in the spectator

Table 6.4: The measured top spin asymmetries.

		spin analyzer		
		muon spin	b-tagged jet	neutrino
spin basis	spectator basis	$0.23^{+0.20}_{-0.44}$	$-0.33^{+0.44}_{-0.23}$	$0.10^{+0.55}_{-0.55}$
	beamline basis	$0.17^{+0.20}_{-0.44}$	$-0.29^{+0.45}_{-0.20}$	$0.41^{+0.52}_{-0.75}$

**Figure 6.20:** The significance for the asymmetry measurement for the muons spin analyzer in the spectator basis.

basis has a significance of 1.55σ with respect to the SM expectation of $A_{\text{theo.,}\mu}^{\text{spec.}} = 0.49$.

The given measured asymmetry for the b-tagged jet spin analyzer is shifted, because the simulated SM scenario does not lie on the angle bisector (figure 6.18). The shifted measured asymmetry for the b-tagged jet spin analyzer $A_b^{\text{spec.}} = -0.13$ agrees well with the SM expectation of $A_{\text{theo.,}b}^{\text{spec.}} = -0.19$. It has a significance of 0.06σ . For the neutrino spin analyzer, the measured asymmetry of $A_\nu^{\text{spec.}} = 0.10$ has a significance of 0.72σ with the SM expectation of $A_{\text{theo.,}\nu}^{\text{spec.}} = -0.17$.

6.4.3 Fit to Anomalous Couplings

The program “TopFit” [5] can be used to constrain anomalous top quark couplings by combining results from cross section measurements [33, 35], W boson helicity fractions measurement [36] and the measured top quark spin asymmetries from this analysis. The exclusion limits for the anomalous top quark couplings V_L , V_R , g_L , and g_R are shown in figures 6.21 and 6.22. The limits on the right are obtained with the top quark spin asymmetry measurement and the limits on the left are obtained without the top quark spin asymmetry measurement.

In figure 6.22, the presented measurement of the top quark spin asymmetries provide nearly an exclusion of $g_R > 0$ at a confidence limit of 68%.

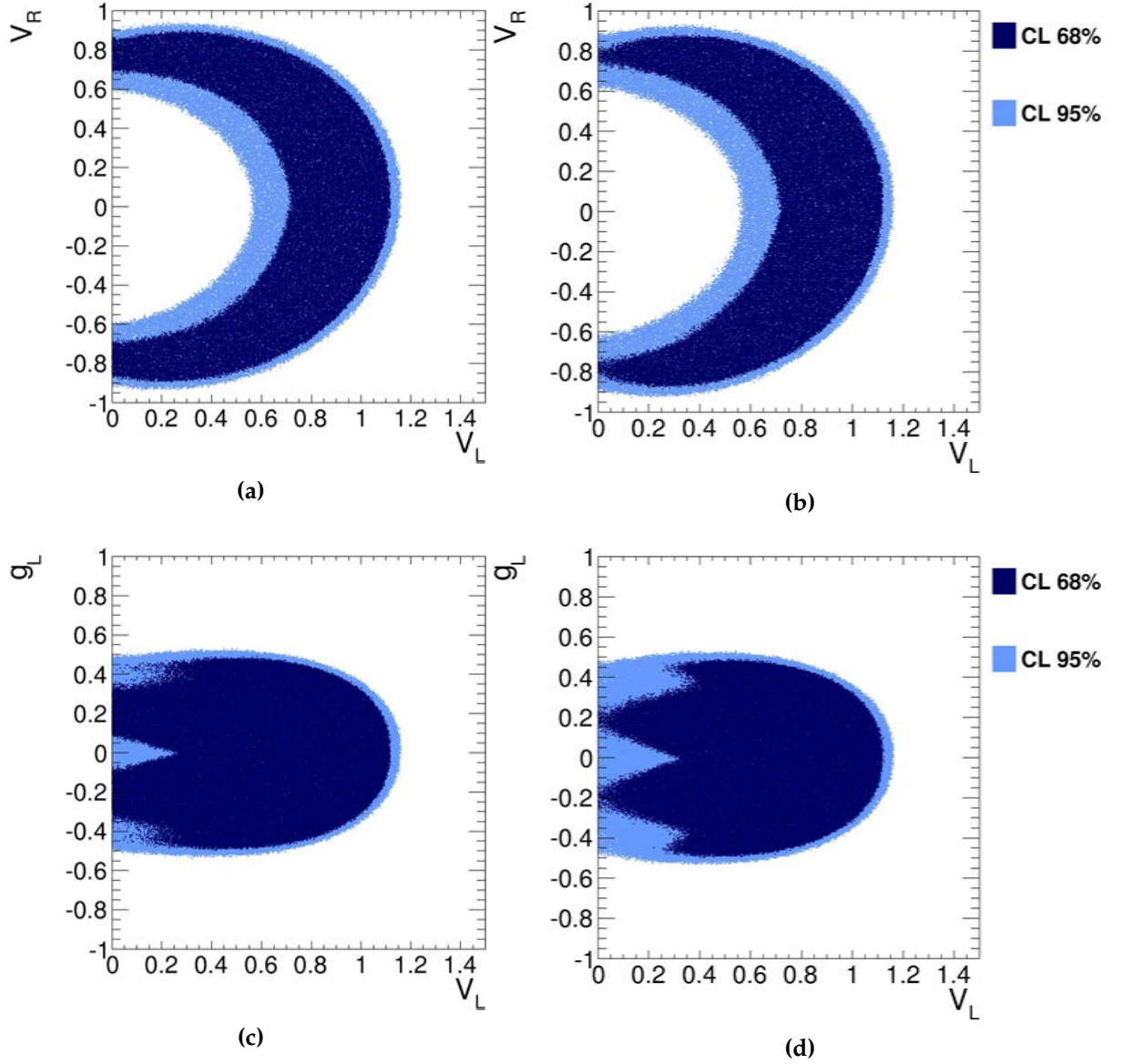


Figure 6.21: Limits on anomalous couplings using the program TopFit. The limits are shown for V_L vs. V_R without (a) and with (b) the top quark spin asymmetries and for V_L vs. g_L without (c) and with (d) the top quark spin asymmetries.

6.4 Results

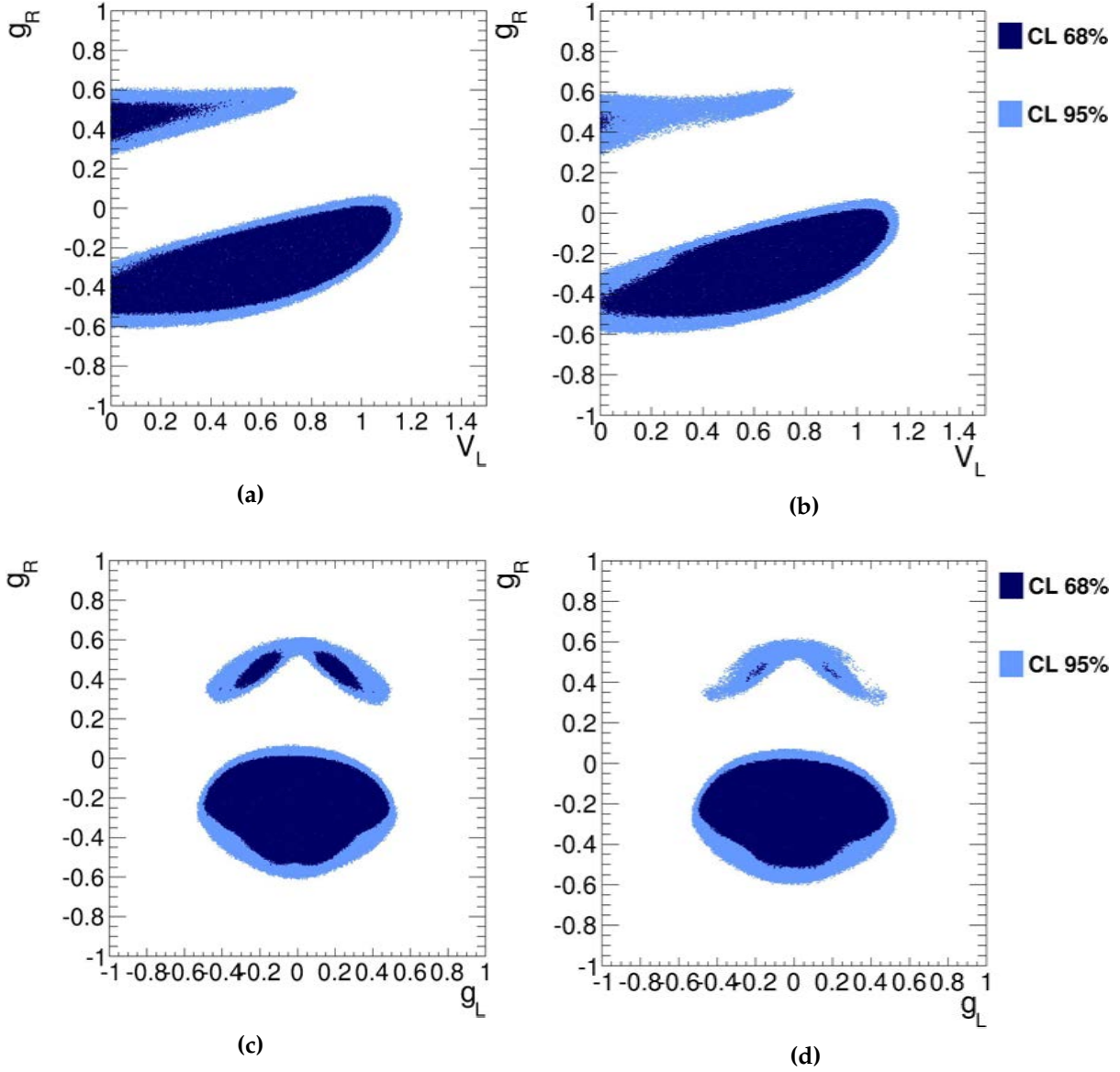


Figure 6.22: Limits on anomalous couplings using the program TopFit. The limits are shown for V_L vs. g_R without (a) and with (b) the top quark spin asymmetries and g_L vs. g_R without (c) and with (d) the top quark spin asymmetries.

Conclusion

This thesis presents a first measurement of the top quark spin asymmetries in single top quark t-channel production. The analysis uses 1.17 fb^{-1} of proton-proton collision data recorded with the Compact Muon Solenoid (CMS) experiment at a center-of-mass energy of $\sqrt{s} = 7 \text{ TeV}$. For the measurement a new analysis strategy is developed.

It is expected from the theory of the Standard Model of Particle Physics (SM) that top quarks have a “vector”-“axialvector” (V-A) coupling structure in electroweak interactions. This is probed by the top quark spin asymmetries.

The asymmetries are calculated from distributions of the angles $\cos \theta_{B,X}$ between the spin analyzers X and the top quark spin bases B in the top quark rest frame. The muon, the bottom quark and the neutrino from leptonically decaying top quarks are chosen as the spin analyzers. The direction of the spectator quark or its projection onto the beamline serves as the top quark spin basis.

The SM predicts the top quark spin asymmetries $A_{\mu}^{\text{spec.}} = 0.49$, $A_b^{\text{spec.}} = -0.19$, and $A_{\nu}^{\text{spec.}} = -0.17$ in the spectator basis. In an effective extension of the SM, the anomalous top quark couplings V_L , V_R , g_L , and g_R arise which can influence these asymmetries.

After the event selection, the contributions from background processes are still very high. Therefore, multivariate classification methods are used to further discriminate between signal and remaining background contributions. Boosted Decision Trees with high discriminating power are applied, while Projective Likelihood Estimators are used as a cross check.

Input variables which are only weakly correlated to the angular distributions minimizes a potential bias if a multivariate discriminator favor the coupling scenario from its training.

The optimal set of input variables and the working point of the discriminator are chosen by minimizing the total uncertainty on the asymmetry measurement. This displays a tradeoff between the high systematic uncertainties from background processes and the statistically dominated uncertainties of the selected single top quark t-channel process.

The angular distributions are unfolded to correct for detector and reconstruction effects. Pseudo-experiments are generated to correctly propagate systematic and statistical uncertainties through the unfolding procedure.

A Neyman construction using event samples according to eight different anomalous coupling scenarios checks for a potential bias on the measurement due to the event selection, signal separation, or the unfolding. The anomalous coupling scenarios are

generated with the WHIZARD Monte-Carlo generator.

In total, three top quark spin asymmetries are measured in the spectator basis and in the beamline basis. The asymmetries with the smallest uncertainties are obtained using the spectator basis with $A_{\mu}^{\text{spec.}} = 0.23^{+0.20}_{-0.44}$, $A_b^{\text{spec.}} = -0.33^{+0.44}_{-0.23}$, and $A_{\nu}^{\text{spec.}} = 0.10^{+0.55}_{-0.55}$. These top quark spin asymmetries are used to constrain the anomalous couplings with additional information from measurements of the single top quark cross sections and the W boson helicity fractions.

The measured top quark spin asymmetry for the muon spin analyzer in the spectator basis is compatible with the SM within a significance of 1.55σ . The top quark spin asymmetry for the b-tagged jet spin analyzer in the spectator basis agrees well with a significance of 0.06σ with the SM. For the top quark spin asymmetry of the neutrino spin analyzer in the spectator basis, the measurement agrees with a significance of 0.72σ with the SM.

Appendix

Table 7.1: Part one of the variable ranking for the multivariate training.

1-5	$\Delta p_T(\text{lightjet top})$, Δp_T (W boson HFS), p_T vector sum (lightjet top), p_T vector sum (W boson HFS), Δp_T (lightjet best top)
6-10	η best top, $\Delta\phi$ (lightjet top), Δp_T (leading jet subleading jet), Δp_T (subleading jet best top), η top
11-15	Δp_T (b-tagged jet top), Δp_T (leading jet best top), Δp_T (bestJet best top), p_T not b-tagged jet, mass (b-tagged jet W boson)
16-20	Δp_T (leading jet top), Δp_T (leading jet bestJet), p_T best top, p_T vector sum (bestJet W boson), Δp_T (bestJet top)
21-25	mass (leading jet W boson), Δp_T (b-tagged jet best top), mass (muon top), Δp_T (subleading jet top), mass (W boson best top)
26-30	p_T vector sum (b-tagged jet W boson), p_T top, $\Delta\eta$ (leading jet top), mass (MET top), mass (muon best top)
31-35	Δp_T (muon lightjet), mass (W boson top), mass (leading jet best top), Δp_T (subleading jet bestJet), p_T vector sum (MET best top)
36-40	η leading jetTop, mass (MET best top), $\Delta\eta$ (bestJet best top), $\Delta\eta$ (b-tagged jet top), mass (subleading jet W boson)
41-45	Δp_T (muon top), mass (subleading jet top), Δp_T (bestJet W boson), Δp_T (muon best top), η light jet
46-50	\hat{s} , η subleading jet, p_T vector sum (subleading jet W boson), mass (subleading jet best top), $\Delta\eta$ (lightjet top)
51-55	p_T vector sum (muon best top), mass (bestJet top), mass (b-tagged jet best top), mass (bestJet W boson), mass (MET HFS)
56-60	Δp_T (b-tagged jet bestJet), mass (leading jet top), ΔR (lightjet top), \cos (b-tagged jet W boson), Δp_T (leading jet b-tagged jet)

Table 7.2: Part two of the variable ranking for the multivariate training.

61-65	Δp_T (subleading jet light jet), Δp_T (b-tagged jet W boson), mass (subleading jet light jet), mass (leading jet MET), mass (lightjet best top)
66-70	$\Delta\eta$ (leading jet best top), $\Delta\eta$ (subleading jet top), mass best top, Δp_T (lightjet bestJet), Δp_T (subleading jet b-tagged jet)
71-75	Δp_T (leading jet lightjet), Δp_T (subleading jet W boson), $\Delta\eta$ (subleading jet best top), $\Delta\eta$ (lightjet best top), mass (W boson HFS)
76-80	mass (lightjet top), E_T^{jets} , sphericity lambda 2, Δp_T (subleading jet MET), $\Delta\eta$ bestJet top
81-85	$\cos(\text{MET W boson})$, $\Delta\eta$ (muon best top), mass (muon leading jet), $\cos(\text{muon W boson})$, Δp_T (lightjet MET)
86-90	η leading jet, $\cos(\text{W boson best top})$, mass (subleading jet MET), η bestJet, p_T vector sum (W boson best top)
91-95	aplanarity, sphericity lambda 3, sphericity, sphericity lambda 1, Δp_T (muon subleading jet)
95-100	mass (lightjet MET), mass (lightjet W boson), Δp_T (MET top), mass (leading jet b-tagged jet), mass (leading jet bestJet)

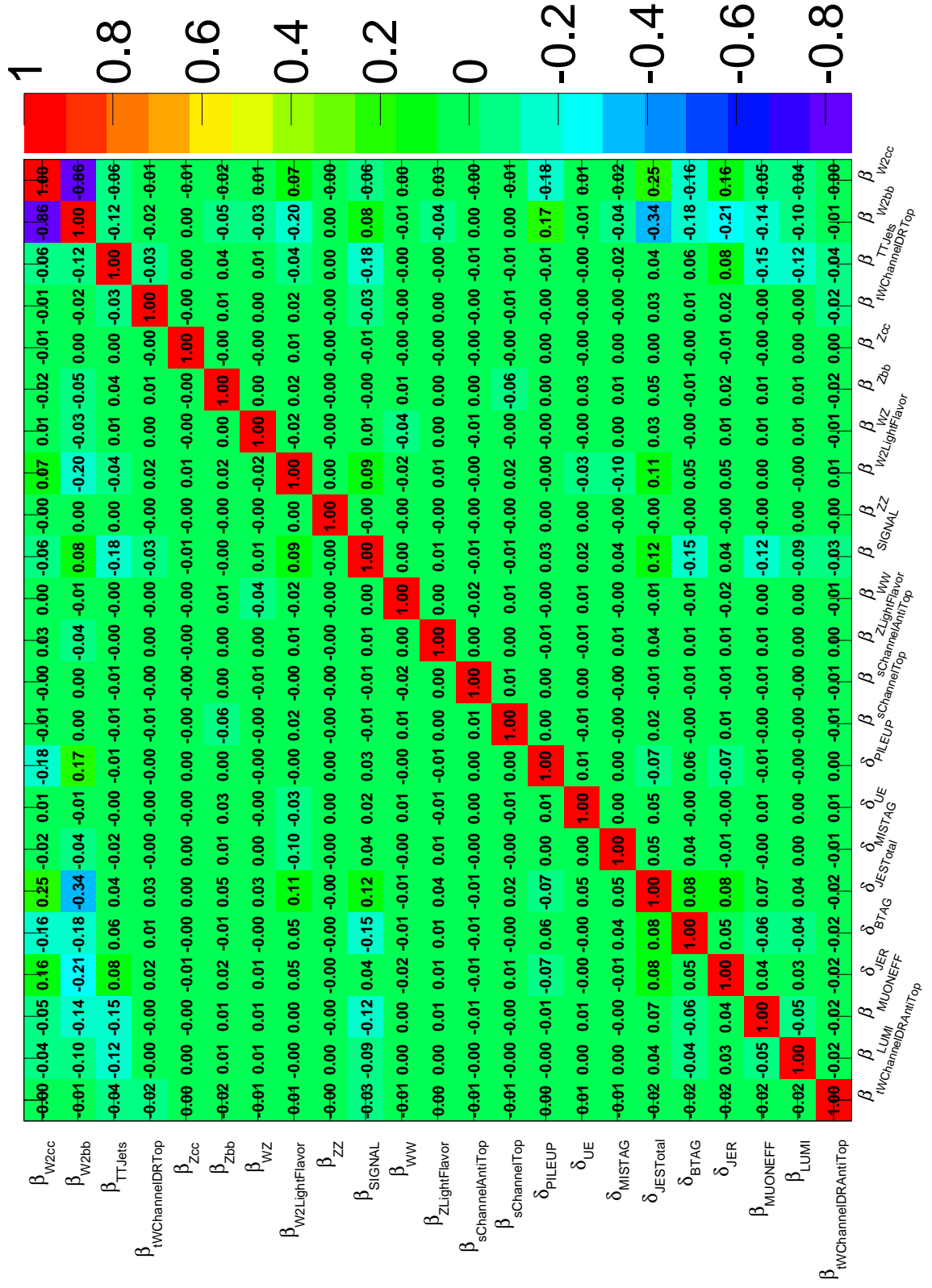


Figure 7.1: Correlation matrix from the fit to the reconstructed top quark mass.

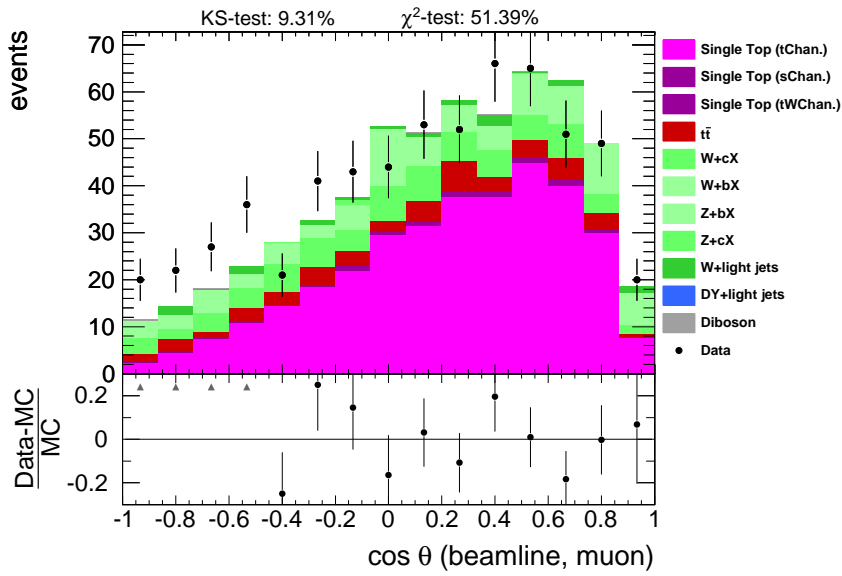


Figure 7.2: Differential distribution for the muon spin analyzer in the beamline basis.

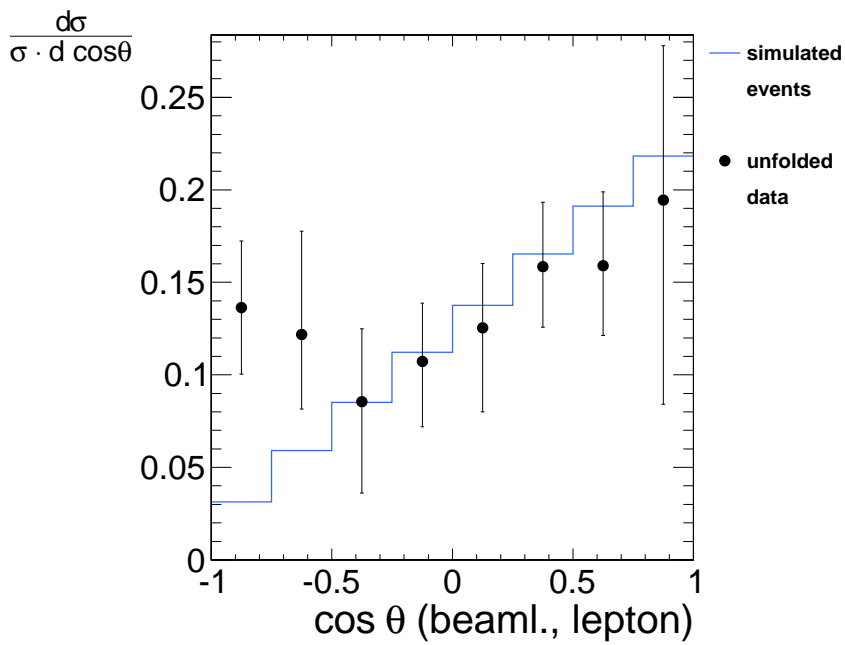


Figure 7.3: Differential distribution for the muon spin analyzer in the beamline basis.

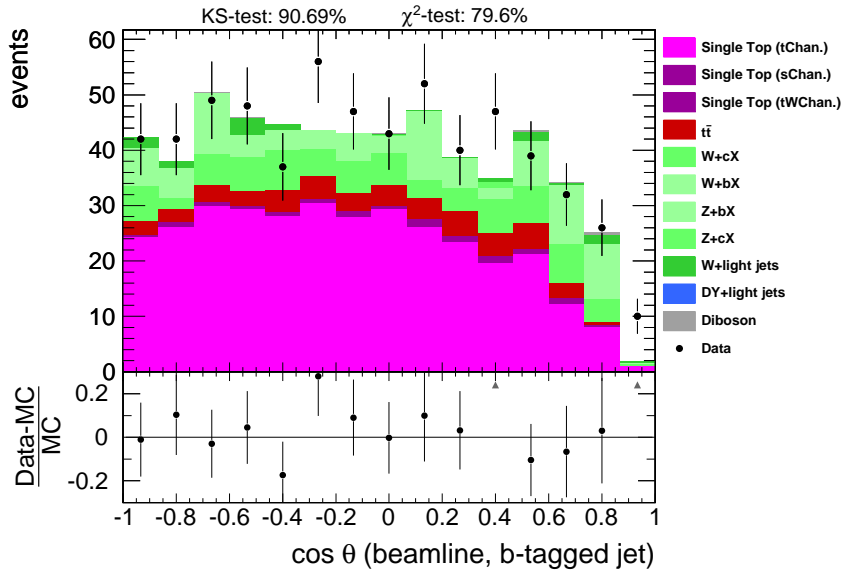


Figure 7.4: Differential distribution for the b-tagged jet spin analyzer in the beamline basis.

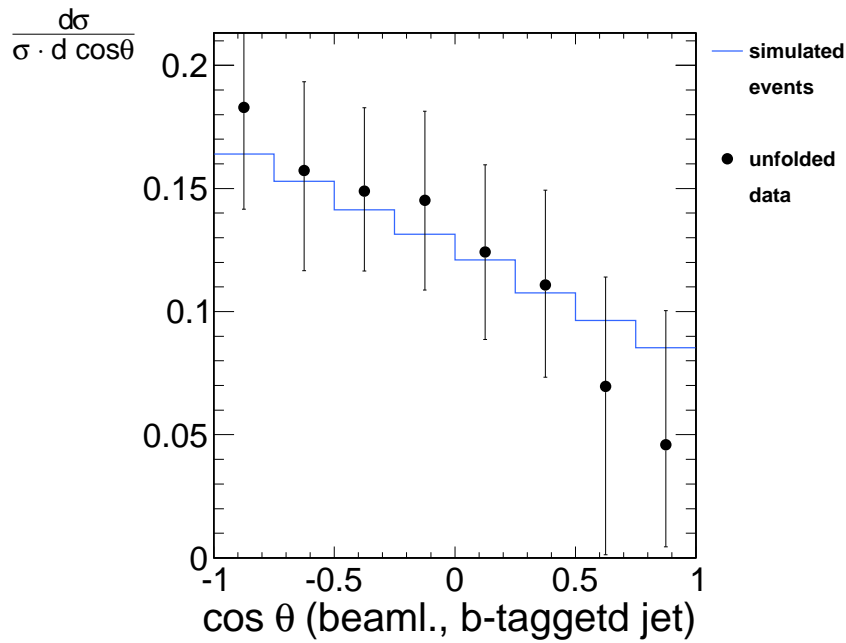


Figure 7.5: Differential distribution for the b-tagged jet spin analyzer in the beamline basis.

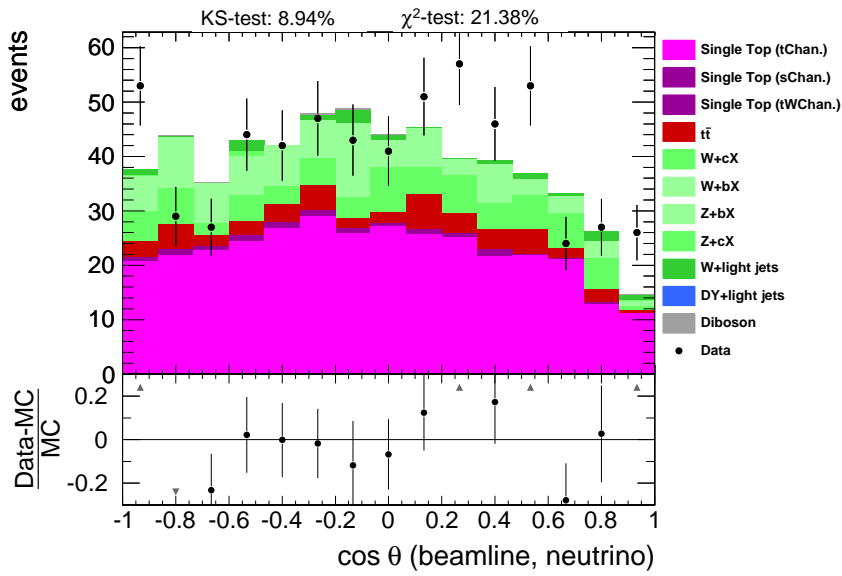


Figure 7.6: Differential distribution for the neutrino spin analyzer in the beamline basis.

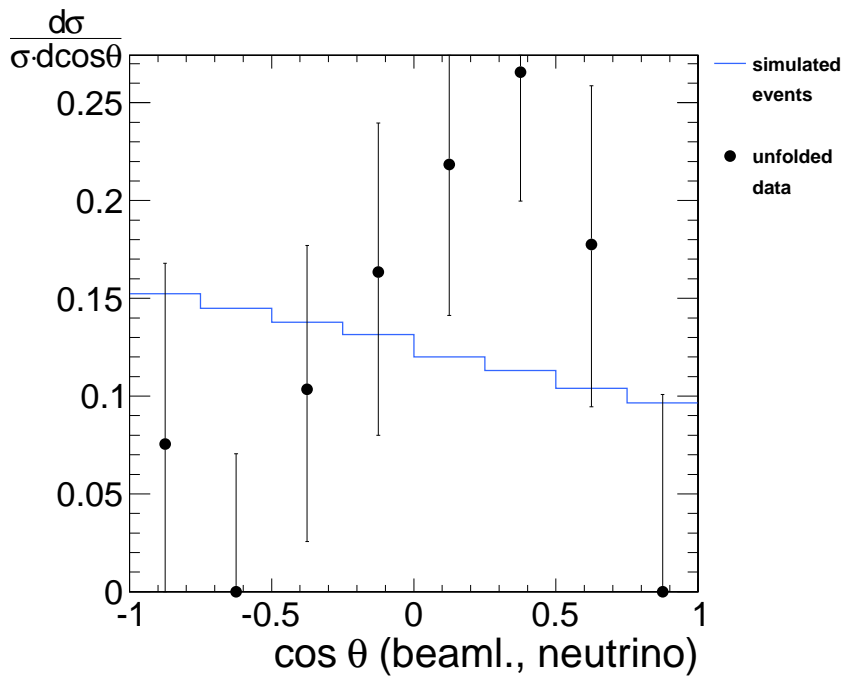


Figure 7.7: Differential distribution for the neutrino spin analyzer in the beamline basis.

List of Figures

2.1	The Higgs Potential - “Mexican Hat”	7
2.2	The production and decay of the top quark.	10
2.3	Quantization of the W boson spin.	12
2.4	Quantization of the top quark spin.	13
3.1	The CERN accelerator complex	16
3.2	The CMS detector and its sub systems.	18
3.3	The CMS trigger system.	20
3.4	Jet definition in different scenarios of additional particles	22
4.1	Signature of single top quark t-channel production.	27
4.2	The simulated $\frac{d\sigma}{d\cos\theta_{B,X}}$ distributions for the lepton, bottom quark, and neutrino.	31
4.3	The resulting W boson helicity fractions.	32
4.4	QCD background in the transverse W boson mass distribution	37
4.5	The “top quark event view” inside VISPA.	37
4.6	WHIZARD SM and Powheg comparison	40
4.7	WHIZARD SM and Powheg comparison.	41
5.1	The $\frac{d\sigma}{d\cos\theta_{B,X}}$ distributions after the event selection.	44
5.2	Correlation of the first and 100th variable to $\cos\theta_{\text{spec.,muon}}$	47
5.3	Some of the input variables used for the training of the multivariate discriminators.	48
5.4	Discriminator outputs for some trained BDTs and PLEs.	49
5.5	Exemplary discrimination power.	50
5.6	The ill-posed unfolding problem.	52
5.7	Correlations in an unregularized unfolded distribution.	55
5.8	Regularized correlations for an exemplary detector.	56
5.9	Exemplary optimization for the $\cos\theta_{\text{spec.,muon}}$ angle.	57

5.10	Construction of the response matrix.	57
5.11	The response matrices for the observables in the spectator basis.	59
6.1	Number of vertices distribution for the simulated events with Powheg. .	64
6.2	Distribution of $\cos\theta_{\text{spec},\mu\text{on}}$ in the two jet and non b-tagged jet control region.	65
6.3	The reconstructed top quark mass distribution before the data-driven W+jets estimation.	66
6.4	The reconstructed top quark mass distribution after scaling the W+bX contribution to the fit result.	67
6.5	Event variables before and after the fit to the reconstructed top quark mass.	70
6.6	Measurement procedure with Neyman construction.	71
6.7	The anomalous coupling sample from which the response matrices are constructed.	72
6.8	Schematic Neyman construction.	73
6.9	BDT outputs and asymmetry uncertainty for different discriminator values.	74
6.10	Asymmetries and their uncertainties after the Neyman construction with the BDT method.	77
6.11	Exemplary PLE outputs.	78
6.12	Top quark spin asymmetries and their uncertainties in the spectator basis after the Neyman construction with the PLE method.	78
6.13	The $\frac{d\sigma}{d\cos\theta_{\text{spec},\mu\text{on}}}$ before and after the unfolding.	80
6.14	The $\frac{d\sigma}{d\cos\theta_{\text{spec},\text{tagged jet}}}$ before and after the unfolding.	81
6.15	The $\frac{d\sigma}{d\cos\theta_{\text{spec},\text{neutrino}}}$ before and after the unfolding.	82
6.16	The used legend for the Neyman constructions.	83
6.17	The top spin asymmetry measurement for the muon spin analyzer. (a): spectator basis, (b) beamline basis.	83
6.18	The top spin asymmetry measurement for the b-tagged jet spin analyzer. (a): spectator basis, (b) beamline basis.	84
6.19	The top spin asymmetry measurement for the neutrino spin analyzer. (a): spectator basis, (b) beamline basis.	84
6.20	The significance for the asymmetry measurement for the muons spin analyzer in the spectator basis.	85
6.21	Limits on anomalous couplings 1.	87
6.22	Limits on anomalous couplings 2.	88

7.1	Correlation matrix from the fit to the reconstructed top quark mass. . . .	C
7.2	Differential distribution for the muon spin analyzer in the beamline basis.	D
7.3	Differential distribution for the muon spin analyzer in the beamline basis.	D
7.4	Differential distribution for the b-tagged jet spin analyzer in the beamline basis.	E
7.5	Differential distribution for the b-tagged jet spin analyzer in the beamline basis.	E
7.6	Differential distribution for the neutrino spin analyzer in the beamline basis.	F
7.7	Differential distribution for the neutrino spin analyzer in the beamline basis.	F

List of Tables

2.1	The SM leptons.	3
2.2	The SM Quarks.	4
2.3	The SM interactions and their gauge bosons	4
2.4	Top quark cross sections.	10
2.5	The expected top quark spin asymmetries.	14
4.1	The simulated SM samples.	28
4.2	The simulated processes with WHIZARD.	30
4.3	The resulting top quark spin asymmetries and W boson helicity fractions.	33
4.4	Event yields of data and MC samples after event selection.	36
6.1	The scale factors for the b-tagging efficiency.	62
6.2	Results from fit to the reconstructed top quark mass.	68
6.3	Impact of systematic uncertainties.	69
6.4	The measured top spin asymmetries.	85
7.1	Part one of the variable ranking for the multivariate training.	A
7.2	Part two of the variable ranking for the multivariate training.	B

Bibliography

- [1] G. Aad et al., *Observation of a new particle in the search for the Standard Model Higgs boson with the ATLAS detector at the LHC*, Phys.Lett. **B716** (2012), 1–29, arXiv:1207.7214 [hep-ex].
- [2] F. Abe et al., *Observation of top quark production in $\bar{p}p$ collisions*, Phys. Rev. Lett. **74** (1995), 2626–2631, arXiv:hep-ex/9503002 [hep-ex].
- [3] S. Agostinelli et al., *Geant4 - a simulation toolkit*, Nuclear Instruments and Methods in Physics Research Section A: Accelerators, Spectrometers, Detectors and Associated Equipment **506** (2003), no. 3, 250 – 303.
- [4] J.A. Aguilar-Saavedra, *A Minimal set of top anomalous couplings*, Nucl.Phys. **B812** (2009), 181–204, arXiv:0811.3842 [hep-ph].
- [5] J.A. Aguilar-Saavedra and J. Bernabeu, *W polarisation beyond helicity fractions in top quark decays*, Nucl.Phys. **B840** (2010), 349–378, arXiv:1005.5382 [hep-ph].
- [6] J.A. Aguilar-Saavedra et al., *Probing anomalous Wtb couplings in top pair decays*, Eur. Phys. J. **C50** (2007), 519–533, arXiv:hep-ph/0605190 [hep-ph].
- [7] S. Alioli et al., *A general framework for implementing NLO calculations in shower Monte Carlo programs: the POWHEG BOX*, JHEP **1006** (2010), 043, arXiv:1002.2581 [hep-ph].
- [8] J. Alwall et al., *MadGraph 5 : Going Beyond*, JHEP **1106** (2011), 128, arXiv:1106.0522 [hep-ph].
- [9] F. Bach and T. Ohl, *Anomalous Top Couplings at Hadron Colliders Revisited*, (2012), arXiv:1209.4564 [hep-ph].
- [10] A. Barczyk et al., *Measurement of the Fermi Constant by FAST*, Phys.Lett. **B663** (2008), 172–180, arXiv:0707.3904 [hep-ex].
- [11] G.L. Bayatian et al., *CMS physics: Technical design report*, (2006), CERN-LHCC-2006-001.
- [12] A. Belyaev and E. Boos, *Single top quark $tW + X$ production at the CERN LHC: A Closer look*, Phys. Rev. **D63** (2001), 034012, arXiv:hep-ph/0003260 [hep-ph].
- [13] W. Bernreuther, *Top quark physics at the LHC*, J.Phys. **G35** (2008), 083001, arXiv:0805.1333 [hep-ph].
- [14] V. Blobel, *An Unfolding method for high-energy physics experiments*, (2002), arXiv:hep-ex/0208022 [hep-ex].

- [15] A.P. Bradley, *The use of the area under the roc curve in the evaluation of machine learning algorithms*, Pattern Recognition **30** (1997), no. 7, 1145 – 1159.
- [16] H.-P. Bretz et al., *A Development Environment for Visual Physics Analysis*, Journal of Instrumentation **7** (2012), 8005, arXiv:1205.4912 [physics.data-an].
- [17] R. Brun et al., *ROOT, an object oriented data analysis framework*, 17 - 30 Sep 2000, 23rd CERN School of Computing,
<http://root.cern.ch>.
- [18] A. Buckley et al., *Systematic event generator tuning for the LHC*, Eur. Phys. J. **C65** (2010), 331–357, arXiv:0907.2973 [hep-ph].
- [19] M. Cacciari et al., *The Anti-k(t) jet clustering algorithm*, JHEP **0804** (2008), 063, arXiv:0802.1189 [hep-ph].
- [20] J.M. Campbell et al., *Vector boson pair production at the LHC*, JHEP **1107** (2011), 018, arXiv:1105.0020 [hep-ph].
- [21] S. Chatrchyan et al., *Observation of a new boson at a mass of 125 GeV with the CMS experiment at the LHC*, Phys.Lett. **B716** (2012), 30–61, arXiv:1207.7235 [hep-ex].
- [22] The CMS Collaboration, *Particle-Flow Event Reconstruction in CMS and Performance for Jets, Taus and ET(miss)*, 2009, CMS Physics Analysis Summary CMS-PAS-PFT-09-001.
- [23] The CMS Collaboration, *Commissioning of the particle-flow event reconstruction with leptons from J/Psi and W decays at 7 TeV*, 2010, CMS Physics Analysis Summary CMS-PAS-PFT-10-003.
- [24] The CMS Collaboration, *Jet Energy Resolution in CMS at $\sqrt{s} = 7\text{TeV}$* , 2010, CMS Physics Analysis Summary CMS-PAS-JME-10-014.
- [25] The CMS Collaboration, *Performance and operation of the cms electromagnetic calorimeter*, Journal of Instrumentation **5** (2010), no. 03, T03010.
- [26] The CMS Collaboration, *Performance of muon identification in pp collisions at $\sqrt{s} = 7\text{TeV}$* , 2010, CMS Physics Analysis Summary CMS-PAS-MUO-10-002.
- [27] The CMS Collaboration, *Absolute Calibration of Luminosity Measurement at CMS: Summer 2011 Update*, 2011, CMS Physics Analysis Summary CMS-PAS-EWK-11-001.
- [28] The CMS Collaboration, *b-Jet Identification in the CMS Experiment*, 2011, CMS Physics Analysis Summary CMS-PAS-BTV-11-004.
- [29] The CMS Collaboration, *Determination of jet energy calibration and transverse momen-*

- tum resolution in CMS*, Journal of Instrumentation **6** (2011), 11002, arXiv:1107.4277 [physics.ins-det].
- [30] The CMS Collaboration, *Measurement of the inelastic pp cross section at $\sqrt{s} = 7$ TeV with the CMS detector*, 2011, CMS Physics Analysis Summary CMS-PAS-FWD-11-001.
 - [31] The CMS Collaboration, *Missing transverse energy performance of the cms detector*, Journal of Instrumentation **6** (2011), no. 09, P09001.
 - [32] The CMS Collaboration, *Absolute Calibration of the Luminosity Measurement at CMS: Winter 2012 Update*, 2012, CMS Physics Analysis Summary CMS-PAS-SMP-12-008.
 - [33] The CMS Collaboration, *Evidence for associated production of a single top quark and W boson in pp collisions at 7 TeV*, (2012), arXiv:1209.3489 [hep-ex].
 - [34] The CMS Collaboration, *First measurement of $B(t \rightarrow Wb)/B(t \rightarrow Wq)$ in the dilepton channel in pp collisions at $\sqrt{s} = 7$ TeV*, 2012, CMS Physics Analysis Summary CMS-PAS-TOP-11-029.
 - [35] The CMS Collaboration, *Measurement of the single-top-quark t -channel cross section in pp collisions at $\sqrt{s} = 7$ TeV*, (2012), arXiv:1209.4533 [hep-ex].
 - [36] The CMS Collaboration, *W helicity in top pair events*, 2012, CMS Physics Analysis Summary CMS-PAS-TOP-11-020.
 - [37] The CMS Collaboration et al., *The cms experiment at the cern lh*, Journal of Instrumentation **3** (2008), no. 08, S08004.
 - [38] G. Cowan, *A Survey Of Unfolding Methods For Particle Physics*, <http://www.ippp.dur.ac.uk/old/Workshops/02/statistics/proceedings/cowan.pdf>.
 - [39] O. Douglas and the CMS Collaboration, *Fast simulation of the cms detector*, Journal of Physics: Conference Series **219** (2010), no. 3, 032053.
 - [40] F. Englert and R. Brout, *Broken symmetry and the mass of gauge vector mesons*, Phys. Rev. Lett. **13** (1964), 321–323.
 - [41] L. Evans and P. Bryant, *Lhc machine*, Journal of Instrumentation **3** (2008), no. 08, S08001.
 - [42] M. Feindt and M. Prim, *An algorithm for quantifying dependence in multivariate data sets*, ArXiv e-prints (2012), arXiv:1207.0981 [physics.data-an].
 - [43] D. Fournier, *Performance of the LHC, ATLAS and CMS in 2011*, EPJ Web Conf. **28** (2012), 01003, arXiv:1201.4681 [hep-ex].

- [44] G.S. Guralnik et al., *Global conservation laws and massless particles*, Phys. Rev. Lett. **13** (1964), 585–587.
- [45] A. Heinson, *Useful Diagrams of Top Signals and Backgrounds*, Oct 2011, http://www-d0.fnal.gov/Run2Physics/top/top_public_web_pages/top_feynman_diagrams.html.
- [46] P.W. Higgs, *Broken symmetries and the masses of gauge bosons*, Phys. Rev. Lett. **13** (1964), 508–509.
- [47] P.W. Higgs, *Broken symmetries, massless particles and gauge fields*, Phys.Lett. **12** (1964), 132–133.
- [48] A. Hocker and V. Kartvelishvili, *SVD approach to data unfolding*, Nucl.Instrum.Meth. **A372** (1996), 469–481, arXiv:hep-ph/9509307 [hep-ph].
- [49] A. Hoecker et al., *TMVA - Toolkit for Multivariate Data Analysis*, ArXiv Physics e-prints (2007), arXiv:physics/0703039.
- [50] J. Beringer et. al. (Particle Data Group), *Review of Particle Physics (RPP)*, Phys. Rev. **D86** (2012), 010001.
- [51] C.D. Jones et al., *The new CMS Event Data Model and Framework*, 2006, Proc. Computing in High Energy Physics (CHEP2006), Mumbai, India.
- [52] N. Kidonakis, *NNLL resummation for s-channel single top quark production*, Phys. Rev. **D81** (2010), 054028, arXiv:1001.5034 [hep-ph].
- [53] N. Kidonakis, *Top quark pair and single top production at Tevatron and LHC energies*, PoS **ICHEP2010** (2010), 059, arXiv:1008.2460 [hep-ph].
- [54] N. Kidonakis, *Two-loop soft anomalous dimensions for single top quark associated production with a W- or H-*, Phys. Rev. **D82** (2010), 054018, arXiv:1005.4451 [hep-ph].
- [55] N. Kidonakis, *Next-to-next-to-leading-order collinear and soft gluon corrections for t-channel single top quark production*, Phys. Rev. **D83** (2011), 091503, arXiv:1103.2792 [hep-ph].
- [56] W. Kilian et al., *WHIZARD: Simulating Multi-Particle Processes at LHC and ILC*, Eur. Phys. J. **C71** (2011), 1742, arXiv:0708.4233 [hep-ph].
- [57] D. Klingebiel, *Prospects for a Measurement of the t-Channel Single Top Quark Cross Section with the CMS Experiment*, Master’s thesis, RWTH Aachen University, 2010.
- [58] C. Lefèvre, *The CERN accelerator complex*, 2008, <http://cdsweb.cern.ch/record/1260465>.
- [59] K. Melnikov and F. Petriello, *Electroweak gauge boson production at hadron colliders*

- through $O(\alpha(s)^2)$, Phys. Rev. **D74** (2006), 114017, arXiv:hep-ph/0609070 [hep-ph].
- [60] T. Müeller et al., *theta - a framework for template-based statistical modeling and inference*, 2010, IEKP-KA-CMS/2012-1
<http://theta-framework.org>.
- [61] The CERN Press Office, *LHC sets new record - accelerates beam to 3.5 TeV*, Press Release 05.10, 19.03.2010.
- [62] M.E. Peskin and D.V. Schroeder, *An introduction to quantum field theory (frontiers in physics)*, Westview Press, 1995.
- [63] W.H. Press et al., *Numerical recipes 3rd edition: The art of scientific computing*, 3 ed., Cambridge University Press, 2007.
- [64] A. Rizzi et al., *Track impact parameter based b-tagging with CMS*, CMS NOTE 2006/019.
- [65] G.P. Salam and G. Soyez, *A Practical Seedless Infrared-Safe Cone jet algorithm*, JHEP **0705** (2007), 086, arXiv:0704.0292 [hep-ph].
- [66] S. Schmitt, *TUnfold: an algorithm for correcting migration effects in high energy physics*, ArXiv e-prints (2012), arXiv:1205.6201 [physics.data-an].
- [67] T. Sjostrand et al., *PYTHIA 6.4 Physics and Manual*, JHEP **0605** (2006), 026, arXiv:hep-ph/0603175 [hep-ph].
- [68] D. Spiga et al., *Crab: the cms distributed analysis tool development and design*, Nucl. Phys. B, Proc. Suppl. **177-178** (2008), 267–268.
- [69] P. Sturm et al., *Studies for the Measurement of Single-Top-Quark-Events with the CMS-Experiment*, Ph.D. thesis, KIT, Karlsruhe, 2008, CERN-THESIS-2008-121.
- [70] T.M.P. Tait, *The tW^- mode of single top production*, Phys. Rev. **D61** (2000), 034001, arXiv:hep-ph/9909352 [hep-ph].
- [71] Z. Was, *TAUOLA the library for tau lepton decay, and KKMC / KORALB / KORALZ /... status report*, Nucl.Phys.Proc.Suppl. **98** (2001), 96–102, arXiv:hep-ph/0011305 [hep-ph].
- [72] C.S. Wu et al., *Experimental test of parity conservation in beta decay*, Phys. Rev. **105** (1957), 1413–1415.

Danksagung

Diese Arbeit wäre ohne die stetigen Diskussionen innerhalb des “top” CMS Teams nicht zustande gekommen. Mein erster Dank gilt daher Prof. Dr. Martin Erdmann, Robert Fischer, Dennis Klingebiel und Jan Steggemann.

Besonders bei Dennis Klingebiel möchte ich für die exzellente Betreuung während der Arbeit danken. Bei Prof. Dr. Martin Erdmann bedanke ich mich ausserdem für die Möglichkeit an einem so interessanten Thema zum Abschluss meines Masterstudium zu arbeiten. Dies hat mir besonders viel Freude bereitet!

Prof. Dr. Thomas Hebbeker danke ich für die Übernahme der Zweitkorrektur.

Zuletzt danke ich meinen Eltern für ihre Unterstützung besonders in der letzten Zeit vor der Fertigstellung der Arbeit.

Erklärung

Hiermit versichere, dass ich diese Arbeit selbstständig verfasst und keine anderen als die angegebenen Hilfsmittel und Quellen benutzt habe.

Aachen, den 17.10.2012